FORMATION OF CRYSTALLOGRAPHIC TEXTURES DURING MANUFACTURING OF TUBES OF ZIRCALOY 4

by

DENIS LOUIS VUILLAUME

Ingenieur Civil des Mines de Paris 1974

SUBMITTED IN PARTIAL FULFILLMENT
OF THE REQUIREMENTS FOR THE
DEGREE OF

MASTER OF SCIENCE

at the

MASSACHUSETTS INSTITUTE OF TECHNOLOGY

September 1977

Signature redacted

Signature of Author.....
Department of Materials Science and Engineering
August 12, 1977

Signature redacted

Certified by.....
Thesis Supervisor

Signature redacted

Accepted by.....
Chairman, Departmental Committee on Graduate Students

FORMATION OF CRYSTALLOGRAPHIC TEXTURES DURING MANUFACTURING OF TUBES OF ZIRCALOY-4

by

DENIS LOUIS VUILLAUME

Submitted to the Department of Materials Science and Engineering on August 12, 1977 in partial fulfillment of the requirements for the Degree of Master of Science.

ABSTRACT

The different parameters which control the manufacturing process of Zircaloy tubes have been reviewed and correlated with the crystallographic texture of the tubes.

The formation and evolution of the crystallographic textures during the reduction of the Zircaloy-4 tubes were determined as a function of the strain path.The results were analysed in term of deformation parameters and tool design. It is shown that small changes in the plastic strain paths can lead to marked texture variations.

Thesis Supervisor: Regis M.N Pelloux
Title: Professor of Metallurgy

TABLE OF CONTENTS

LIST OF TABLES

LIST OF FIGURES

ACKNOWLEDGMENTS

I would like to express my gratitude to Professor Regis Pelloux for his guidance and precious encouragements during the course of this study.

I am specially grateful to David Knorr who kindly offered his expertise in texture characterization.

I would also like to thank my sponsor for the opportunity to devote myself to this study.

I finally want to thank my wife Marie-Pierre for her patience, and our son Antoine for his special kind of encouragements.

I. INTRODUCTION

The low temperature hexagonal phase of zirconium exhibits a marked anisotropic mechanical behaviour due to the limited number of slip systems and due to the deformation by twinning.Consequently, during plastic forming of polycrystalline zirconium and zirconium alloys, this anisotropy results in the development of strong preferred orientations.

The preferred crystallographic orientation or texture confers to a polycrystalline mill product some of the single crystal anisotropic mechanical behaviour.

If the mill product is a finished structural component, this mechanical anisotropy has to be taken into account in design, since it can either seriously limit or increase the allowable design streses.

If the mill product is to undergo further deformation processing, its texture and the associated mechanical anisotropy will determine the degree of formability of the material, the level of the forces required for the next fabrication step, and the texture obtained in the finished product.

Thus, in order to take advantage of the mechanical anisotropy, two expertises are required: on one hand, the knowledge of how to relate a given texture to the mechanical properties of a structural component; on the other hand, a satisfactory control of the development of textures during manufacturing operations.

The use of zirconium alloys as cladding and structural material in the cores of the water cooled nuclear reactors, has led to extensive research programs to attain these expertises.These programs involved:

- the charaterization of textures, detailed measurements of the mechanical anisotropy for short time deformations and for creep;
- mechanical models for the deformation of textured polycrystalline material, to orient and support the linking of experimental results on textures and anisotropy;
- characterization of the deformation in various manufacturing processes and of the texture development.

The goals of the present study were:

-1) to review the manufacturing processes currently available for the fabrication of zircaloy tubes to be used as fuel sheaths in water cooled nuclear reactors;

-2) to review the various parameters and methods proposed to characterize the deformation and texture evolutions during fabrication;

-3) to characterize quantitatively the deformation and texture evolution during manufacturing of Zircaloy-4. Two reduction transitions were analyzed,that were part of two different manufacturing processes; one process used a three rolls machine of the rocking roll-reducer type and a cylindrical mandrel; the other process used a two rolls pilger and a tapered mandrel.

-4) to determine the best methods to correlate plastic strain path to texture.

2. BACKGROUND

2.1 Fuel clad material in water cooled nuclear reactors

The requirement of a low thermal neutron absorption cross-section for the fuel cladding material in water cooled nuclear reactors, is met by only four metals: Be, Mg, Zr, Al.Among those, only zirconium combines an appropriate water corrosion resistance to mechanical strength at reactor service temperature.

The development of the zirconium-tin (+ Fe.Cr.Ni) alloys that led to the Zircaloy-2, answered a need to improve and control the corrosion resistance to water and steam of the unalloyed zirconium which is very sensitive to ppm ranges of impurity content such as nitrogen.[1]

The nickel free Zircaloy-2,and Zircaloy-4 were developed to reduce the hydrogen pick-up rate during corrosion by the coolant.

Zircaloy-4 mainly finds its application in pressurized light water reactors where the hydrogen overpressure in the coolant makes hydrogen pick-up a problem.

Zircaloy-2 keeps a better corrosion resistance in steam and thus is satisfactorily used in boiling light water reactors.

Other commonly used zirconium alloys are the zirconium-niobium alloys which upon appropriate thermomechanical treatment,yield outstanding mechanical properties.These alloys are presently used in the Canadian CANDU heavy water reactor and in the USSR.[2]

The compositions of the zirconium-base alloys are detailed in Table 1.

The stresses induced in a fuel cladding tube in its reactor environment, are compressive transverse stresses in the early life of the element, due to cooling water pressure.

Internal pre-pressurization of PWR fuel elements makes the level of these compressive stresses comparable in the various types of reactors, although the coolant pressures are different.

As the element burns up, swelling and cracking of the fuel pellets occur, together with fission gas release building up an internal pressure in the cladding tube.

Eventually, the stresses in the clad are all tensile due to the increase of internal stresses.

2.2 Crystallography & Structure

The stable pure zirconium crystal lattice is hexagonal close packed up to 862°C (α-phase) and body centered cubic from 862°C up to the melting point 1855°C (β-phase).[3]

The lattice parameters of the α-phase (hcp) are:[4]

$a_o = 3.23118$ Å

$c_o = 5.14634$ Å

$c/a = 1.59271$

In Zircaloys, the α-phase is stable up to 790°C[5], i.e. well above the normal operating temperatures in reactor service. The α-phase does not dissolve all of the alloying elements; iron and nickel, especially, concentrate in a secondary χ-phase[6] present in

the matrix as evenly distributed particles, with a maximum diameter of one or two microns for the best water corrosion resistance.

The β-phase, stable above 950°C, dissolves all alloying elements Two stages are observed in the phase transformation. From 790°C to 820°C, the χ-phase coexists with α and β .From 820°C to950°C, the structure consists of α and β .[5]

2.3 α-Zirconium HCP crystal.Deformation systems. Crystal anisotropy and deformation behaviour.

Fig.1 shows a HCP lattice cell with the important planes and directions.

Fig.2a & 2b,present some of the deformation systems observed in the α-structure of zirconium and its alloys [7].

The primary slip system at room temperature and up to 500°C is by prismatic slip: slip on first order prim planes $(01\bar{1}0)$ along the $\vec{a}$ direction $2\bar{1}\bar{1}0$.

The other slip systems may be considered to have a minor importance : slip on the basal plane (0001) along the $\vec{a}$ direction $<2\bar{1}\bar{1}0>$ occurs at elevated temperatures only; slip on the first order pyramidal planes $(0\bar{1}\bar{1}1)$ along the $\vec{a}$ direction $<2\bar{1}\bar{1}0>$ was observed only under complex stressing. Slip in the $(\vec{c}+\vec{a})$ direction $<\bar{2}113>$ on $(11\bar{2}1)$ or $(10\bar{1}\bar{1})$ planes requires elevated temperature and constraint[7].

Thus slip is essentially prismatic slip along the $\vec{a}$ direction; this mechanism cannot produce strain in directions out of the basal plane. When deformations are required along the c-axis, twinning

mechanisms are called upon.

Among the twinning mechanisms sketched in Fig.2, the $(10\bar{1}2)$ tensile twinning is the most commonly observed; other tensile $(11\bar{2}1)$ twins are less common; $(10\bar{1}1)$ compressive twins require elevated deformation temperature.

Twinning, unlike slip, is dependent upon the direction of stress. Different twinning systems, with different activation requirements, accommodate tensile and compressive stresses. This is the origin of mechanical anisotropy, and it is the basis for the difference between tension and compression flow stresses in zircaloys (stength differential effect), observed for loading directions close to the $\vec{c}$ axis.

While stresses initiating the various twinning systems are different, all have been shown to be greater than the corresponding critical resolved shear stress for prism slip [7]. Loading directions perpendicular to the basal plane normal direction, or basal pole, correspond to favorable orientations (high Schmid factor) for slip to occur, and thus are "soft" directions. Loading directions close to the basal pole, involve twinning, and thus are "hard" directions.

Deformation by twinning results in the reorientation of the twinned part of the crystal lattice with respect to the stress axis; other deformation mechanisms may then be activated in the twinned material.

For example, in simple tension along the basal pole, the first plastic flow occurs by $(10\bar{1}2)$ $\langle 10\bar{1}1\rangle$ twinning. The twinned material

is then so oriented relative to ths stress axis that it can deform by prism slip. Further twinning is called upon again when slip in the twin requires high activation stresses due to rapid strain hardening[8].

In compression along the basal pole, a problem has to be faced: in polycrystal Zirconium and Zircaloy sheet rolling, the grains with c-axis normal to the rolling direction endure compressive strain along the c-axis without being reoriented.

Picklesimer[8] suggested a sequence of deformation mechanisms that would bring little reorientation in the end; the sequence involved second order or internal tensile twinning $(10\bar{1}2)$ and $(11\bar{2}1)$ inside the initial $(11\bar{2}2)$ compression twins.

Hobson experimentally observed those retwinnings in rolling experiments on Zirconium single crystal.

2.4 Polycrystalline Zircaloy material. Deformation behaviour and texture rotation.

Some care must be taken in extrapolating the results of deformation studies on Zirconium single crystals to Zircaloy polycrystals.

On one hand, because the deformation mechanisms are not as ideally predictable in polycrystals as in single crystals; 1) internal stresses due to accommodation of deformations at grain boundaries and other microstructural features interfere with the macroscopic stress field; 2) the statistical orientation of individual grains (texture) relative to the stress field has to be taken into account.

On the other hand, although the same deformation systems are mostly shared by pure Zirconium and its alloys, there has been a controversy that the mechanism involved in c-axis compression is different for Zirconium and Zircaloy. In Zirconium we have $(11\bar{2}2)$ compression twins- and subsequent retwinning- ; in Zircaloy, $(\vec{c} + \vec{a})$ $<\bar{2}113>$ slip would preferentially occur [9].

However, one may schematically consider that each grain in a polycrystalline sample in a given stress field is strained by the same deformation mechanism that would operate for the individual crystal. In the process, some grains undergo marked lattice reorientation by twinning; others, mainly deformed by slip, maintain their original crystalline orientation. As a result a non random distribution of the crystallite orientations over the whole polycrystal is created. This non random distribution is called crystallographic texture or texture.

The extreme case for a textured polycrystal would be that all grains be congruent crystals. This single crystal situation is approached for instance in conventionnal sheet rolling.

Quasi single crystal material lends itself to easier qualitative interpretation of the deformation and texture evolution observed. The three cases sketched in Fig.3, of quasi single crystal tensile specimens, illustrate at the same time: 1) the anisotropic plastic behaviour and load carrying capacity of textured Zircaloy.

2) the texture rotation associated with plastic deformation [8].

In Fig.3a , tensile prism slip deformation may occur in the axial direction and compressive prism slip in the width direction; the compressive strain in the thickness direction, along the c-axis of most of the grains, whether it is accomplished by $(11\bar{2}2)$ twinning or by $(\vec{c} + \vec{a})\langle 2\bar{1}\bar{1}3\rangle$ slip, is more difficult to initiate and little deformation is thus obtained in the thickness direction.

The specimen elongates and fails under moderate loading by thinning in the width direction. The deformation mechanisms involved have not modified the original alignment of the basal poles. Slip deformation will result in a slight rotation effect analogous to the rotation obtained in constrained single crystal deformation; this slight rotation of the grains around their basal pole puts a different prism direction in the direction of plastic flow. The $(11\bar{2}2)$ twinning and subsequent retwinning involved by the thickness reduction would not have a marked reorientation effect as pointed out earlier; if instead of twinning, $(\vec{c} + \vec{a})$ slip is operative during compression, there will be no reorientation either. The texture of the specimen is thus hardly changed by the deformation.

In Fig.3.b, tensile prism slip deformation may occur in the axial direction, and compressive prism slip in the thickness direction. The width is the hard basal pole direction. Elongation and failure occurs under moderate loading by thickness reduction without width variation. Here the texture is not markedly changed.

In Fig.3.c , the basal poles are parallel to the axial direction; the axial tensile strain requires $(10\bar{1}2)$ twinning which

means a higher flow stress and thus a higher load than in the first two cases. The twinned materials have their basal poles in the width-thickness plane; other mechanisms bring them mostly parallel either to the width or to the thickness directions; the orientations and the mechanisms are then the same as in either of the two cases in Fig.3.a & b . Width and thickness reductions are both obtained under higher loads.

The initial texture has been changed from axial to both normal and transverse basal poles in the deformed region. A single crystal has become a bi-crystal.

The interpretation of texture formation during rolling, with those mechanisms is relatively easy: the strains are tensile in the rolling direction, compressive in the normal direction. There is no strain in the transverse direction, provided that the width of the sheet is many time greater than its thickness. The tensile axial strain rotates all axially oriented basal pole towards the normal transverse plane by $(10\bar{1}2)$ twinning; in this plane, the normal compressive strain leaves only normal and tangential basal poles stable; it can be shown also that this compressive strain rotates all intermediate basal poles towards the normal direction within $\pm$ 30°. Slip in the axial direction brings $(10\bar{1}0)$ poles parallel to the axial orientation.

If we define the stability of a texture as its conservation through continued deformation with proportionnal strain tensors, the initial textures in Fig.3.a & b are stable with respect to the plane

strain deformation observed in each case, at least when considering basal pole orientations.

The initial texture in Fig.3.c is not stable.The reorientation of this texture ends up in a texture stable with respect to a deformation characterized by a certain ratio of reductions in width and thickness.

Picklesimer [8] derives the following texture stability rules: there will be " - stability if there is compression along the basal pole,

- stability if there is a state of plane strain such that the strain can be accomplished by slip and the basal pole is normal to the plane of strain,

- unstability if the strain is produced by tension along the basal pole in which case twinning and rotation to one of the above case will occur."

2.5 Texture measurement by X-ray diffraction

In the above paragraph, we have been able to describe the texture evolution in terms of quasi-single crystals and quasi bi-crystal. Textures are not always so simple, and more precise evaluations are needed to better follow the texture through deformations, as well as to predict the mechanical behaviour.

X-ray diffraction is used to obtain direct and inverse pole figures from which various characterization of the texture are possible.

2.5.1 Inverse pole figure

2.5.1.1 Experimental background

The X-ray intensities, diffracted by all crystallographic planes parallel to the surface of a specimen, are recorded. Specimen surfaces are chosen perpendicular to a principal direction in the material to analyse (e.g. the axial, tangential or radial direction for a tube).A diffractometer is used to continuously vary the X-ray beam incidence angle and scan all possible Bragg angles.

2.5.1.2 Texture coefficients

The integrated X-ray intensity diffracted by a crystallographic plane (hkil) is proportionnal to the volume of irradiated crystallites in which the plane (hkil) is parallel to the specimen surface. Harris [10] proposed as a way to analyze texture, to refer such a volume of crystallites in a textured specimen to its equivalent in a random sample. In doing so, one obtains the volume fraction, in the textured specimen, of crystallites with the plane (hkil) parallel to the specimen surface, and this volume fraction is expressed in times random units. Instead of volume fraction, one rather speaks of density of (hkil) poles oriented normally to the specimen surface. The equivalence of this pole density and of the volume fraction appears if one pole corresponds to a unit volume of crystallite.

If the intensities, I and I°, diffracted by (hkil) in textured and random samples, were obtained in identical operating conditions,

their ratio I/I° would yield directly the pole density. But one preferably uses calculated random intensities. A normalization is then necessary, for which purpose Harris defined the texture coefficient. For the (hkil) plane, denoted as the p^{th} reflection, it is defined as:

$$T.C.\ (\ hkil\ ) = \frac{I'_p\ /\ I''^{\circ}_p}{\frac{1}{N}\ \sum_{i=1}^{N}\ I'_i\ /\ I''^{\circ}_i} \qquad (\ 1\ )$$

where:

- I'_p = measured intensity of p^{th} reflection from textured sample in arbitrary units.
- I''°_p = calculated intensity of p^{th} reflection from a random sample in arbitrary units whose relationship to those for I'_p is unknown. These calculated intensities have been tabulated for zirconium by Sturcken and Duke[11] and are listed in Table 3.
- N = number of reflections considered.

The ratio $I'_p\ /\ I''^{\circ}_p$ is related to the ratio $I_p\ /\ I^{\circ}_p$ for intensities in same units and operating conditions, by an unknown proportionnality $I'_p\ /\ I''^{\circ}_p = K\ .\ I_p\ /\ I^{\circ}_p$. Substitution into Eq. (1) eliminates K :

$$T.C.\ (\ hkil\ ) = \frac{I_p\ /\ I^{\circ}_p}{\frac{1}{N}\ \sum_{i=1}^{N}\ I_i\ /\ I^{\circ}_i} \qquad (\ 2\ )$$

assuming then:

$$\frac{1}{N} \sum_{i=1}^{N} I_i / I^\circ_i = 1 \qquad (3)$$

one obtains:

$$\text{T.C. (hkil)} = I_p / I^\circ_p = \text{(hkil) pole density} \qquad (4)$$

The assumption in Eq.(3) means that the average value of I/I° should be unity, regardless of the preferred orientation in the specimen. Calculation for textured samples yields values a little greater than one, but nevertheless, texture coefficients are considered acceptable approximations to I/I° and thus to pole densities in times random units[13].

2.5.1.3 Inverse pole figure

Texture coefficients are plotted on a standard projection of the hcp crystal. This projection may be entirely represented by 30° sectors for symmetry reasons. Lines of constant T.C. values are drawn using planar interpolation and the result is the inverse pole figure associated with the normal to the specimen surface.Examples of such inverse pole figures are in Fig. 39 & 40 .

This representation may be interpreted as follows: after rearranging all crystallites, so that their crystallographic axes coïncide with those of the stereo-projection, one plots the (inverted) distribution of the normal to the specimen surface [14].

Inverse pole figures associated with three orthogonal directions in the analyzed material (e.g. the axial, tangential and radial directions for a tube), completely represent the orientation distribution of this material (e.g the tube) as observed from a

constant crystallographic orientation in any crystallite.An inverted image of the texture is obtained.

Pole densities, obtained as T.C. values,may be used also in a different way to represent the texture. For hcp material, the angle between (hkil) and (0002) poles , Φ_{hkil} , is known from crystallography; thus, the crystallites with (hkil) poles parallel to the normal D to the specimen surface, have their basal poles on a circular line C of the orientation sphere, with constant inclination Φ_{hkil} relative to D (Fig.4). The density of (hkil) poles in the D direction, thus represents the integrated basal pole density along C. Such integrated basal pole densities, determined for every inclination Φ to D , fully describe a fiber texture of axis D. In other cases, they do not resolve the basal pole density variations on the same level of inclination Φ_{hkil}. For small inclinations to D, they are however representative of the density of basal poles parallel to D within a certain (small) angular range. Such texture analyses were done by Cheadle et al[12], as sketched in Fig.5.

2.5.1.4 Quantitative analysis

Kearns[13] proposed to derive from data on pole densities, an orientation parameter, f, representing the effective fraction of crystallites aligned with their <0001> axis parallel to the reference direction D (normal to the specimen surface). The method calculates by interpolation the average basal pole density in times random units, I (Φ), at each level of inclination Φ relative to D. In fiber textures, this average is simple: basal poles densi-

ties are constant on the same inclination level. One then calculates:

$$V_{\Delta i}\Phi = \frac{\int_{\Phi_1}^{\Phi_2} I(\Phi)\sin\Phi\, d\Phi}{\int_0^{\frac{\pi}{2}} I(\Phi)\sin\Phi\, d\Phi} \qquad (5)$$

which represents the ratio of the volume fraction of crystallites with their basal poles in the inclination band: $\Phi_1<\Phi<\Phi_2$, to the volume fraction (in times random) of crystallites with their basal pole in any inclination band. This denominator is of course unity (when times random units are used), but the ratio in (5) allows elimination of the small discrepancy between ideal pole densities and calculated texture coefficients.

The orientation parameter is defined as:

$$f = \sum V_{\Delta i}\Phi_i \cdot \cos^2\Phi_i = \int_0^{\frac{\pi}{2}} I(\Phi)\sin\Phi\cos^2\Phi\, d\Phi \qquad (6)$$

R.J. Roe[14] developed a more general analytical representation, which has been used by Kallstrom[15] for the reduction of sets of inverse pole figures relative to 3 principal directions.

In this method, the information from the sets of texture coefficients is used to construct a global distribution function $w(\varphi,\omega,\psi)$ where the angles φ,ω,ψ, define the orientation of a single grain (Fig. 6). The function implies that $w(\varphi_1,\omega_1,\psi_1)\sin\varphi_1\, d\varphi\, d\omega\, d\psi$ is the volume fraction of grains with crystal orientation within a small angular range ($d\varphi, d\omega, d\psi$) around orientation $(\varphi_1,\omega_1,\psi_1)$. Integration of w along the circular line C of constant inclination Φ_q relative to the reference direction p on the reference sphere and

and dividing with the same integral of w_o for texture free material, one obtains:

$$\int_C w\,dL \Big/ \int_C w_o\,dL = \int_C w \sin \Phi_q \, dL \Big/ \int_C w_o \sin \Phi_q \, dL \quad (7)$$

That is the volume fraction of grains with crystal orientations (Φ_q , ω , Ψ) i.e with basal poles on C, as observed in the textured sample, divided by the same quantity in texture free material.

This corresponds to the density represented by the texture coefficient T_{pq}, where p is for the reference direction used, and q for the crystallographic plane whose pole inclination to <0001> is Φ_q.

Expansion of w into a series of generalized spherical harmonics, and equating expression (7) to T_{pq}, provides a means to determine the coefficients of the expanded series as linear combinations of the T_{pq} [15].

2.5.2 Direct pole figure

2.5.2.1 Experimental background

A direct pole figure is determined by measuring the variation of the X-ray intensity diffracted by a single family of crystallographic planes, as a function of the relative orientation of the specimen with respect to the diffractometer. The specimen orientation is varied using a gonio sample stage with two degrees of freedom (Fig.7 & 8) .If we fictively invert the sample motion with respect to the diffractometer, we see that diffracted intensities are recorded for all possible orientations of the pole of the selected plane, in the sample coordinates. The sample motion corresponds to a scanning

of those pole orientations located on a spiral in the polar stereographic projection of the sample reference frame (the pole is the normal to the specimen surface) (Fig.9) .

2.5.2.2 Obtention of pole densities in times random units.

The intensity recorded for the pole in the direction of the normal to the specimen surface, can be compared to the T.C. value obtained from the same specimen for the corresponding plane. This may be used to convert the recorded intensities into pole densities in times random units, for all orientations.This conversion is done by evaluating the one time random intensity in the units (cps) used in the diffraction experiment[16]:

$$(cps)_{\varphi=0}^{random} = \frac{(cps)_{\varphi=0} - \text{background cps}}{T.C} \qquad (8)$$

2.5.2.3 Data corrections. Reflection and transmission diffracting geometries.

Details on the diffraction geometries (Fig.7 & 8), their respective range of application and the corrections to be made, may be found in appendix .

2.5.2.4 Direct pole figure.

The pole intensity (in times random units) recorded for every orientation along the spiral scanned in sample reference axes, is plotted on the polar stereographic projection as iso-density loci. The result is the direct pole figure, or simply the pole figure. A pole figure fully describes the preferred orientations of one pole. The complete texture is more fully characterized by complementary

pole figures, obtained from other crystallographic planes.

Several pole figures may be analytically converted into a general orientation distribution function w (φ, ω, ψ) using R.J. Roe's method[14].

3. ZIRCALOY TUBE MANUFACTURING

3.1 Zircaloy tube fabrication

The main steps in the production schedule of Zircaloy tubing are summarized in Table 3.[5]

The operations in the melting stage are designed to assure uniform distribution of alloying elements in the ingot.

Heating into the β - phase field, after hot forging, yields fine secondary χ - phase particles.

Annealing between cold work passes removes strain-hardening and restores the ductility for the following deformation.The effect of annealing on texture has generally been found to be a 30° rotation of the $(10\bar{1}0)$ poles around the basal poles,bringing the $<11\bar{2}0>$ directions into axial alignment. The change in basal pole texture is small.

Straightening does not influence the texture; texture formation is to be looked for in fabrication stages involving larger plastic deformation.

3.2 Plastic deformation during fabrication

3.2.1 Hot forging

Hobson[17] observed the textures in a forged bar,and found preferred inclinations of the basal poles to the bar axis of about 75°. The forging schedule, however, was not specified and other textures might develop in this operation. Specific conditions likely to influence texture are: unrefined microstructure, high strain rate, α-β-α cycling in subsequent quenching.

3.2.2 Extrusion

Tenckhoff and Rittenhouse [18] studied the texture of tube hollows extruded from the same forged bar, with 3 different ratios of wall to diameter reduction. In all cases, the basal pole distribution was heavily concentrated in the plane normal to the extruded tube axis, the radial-tangential (R.T) plane. In this plane, the basal poles were more tangentially oriented to the tube when the ratio of wall to diameter reduction was lower .For the higher ratio, they observed maximum inclinations of the basal poles in the R.T plane of $\pm$ 42.to 46° from the tube radial direction, and also a split of those maximum inclinations at $\pm$ 8°on both sides of the R.T plane.

3.2.3 Cold working

The desired final dimensions of tubing are obtained, from the tube hollow, through a sequence of cold working passes. Most present day manufacturers are thought to utilize a tube reducing technique, but other processes have been or are used, such as plug and mandrel drawing , drawing without inner support also called sinking and swaging[8,19].

Several processes are schematically presented in Fig.10; the strain states and proposed texture evolutions, for two types of quasi-single crystal entering textures (radial or tangential basal poles) are also shown[8].

A few features of these different deformation processes should be pointed out.

- Drawing processes insure good axial symmetry of the deformation,

provided that there are no thickness variations in the entering tube. The deformation in tube reducing and swaging does not have this symmetry.

- In sinking, the deformation is often characterized by wall thickening due to the absence of support for the inner surface of the tube. Wall thickening results in a characteristic tensile radial straining.Such deformation with wall thickening is not limited to the sinking process, but also occurs in the early stages of reduction in the other processes, before contact with the mandrel or plug is made. In the case of cylindrical mandrels, this sinking stage is especially important: it may be half of the deformation brought about in the total pass[20].

A satisfactory interpretation for the evolution of texture in the rolling process has been developed[8,19,9]. Infering from this to tubing fabrication processes in general is reasonable, if an approximate plane strain condition exits and the plane of strain can be defined[19].

In tube sinking (Fig.10c) without wall thickening,this plane of strain is the axial (tensile direction)-tangential (compressive direction) plane. The final texture should show maximum basal pole density in the tangential direction, and prism poles mostly oriented in the axial direction.

In tube sinking with thickening, an approximate plane of strain in the thickening region is the radial(tensile direction) -tangential (compressive direction) plane.One expects then the texture to be rotated in this region towards more tangential basal poles and radial prism

poles ,as sketched in Fig.10c .

The deformation in plug or mandrel drawing (Fig.10.b), tube reducing (Fig. 10.d),and swaging may be divided into an initial sinking phase with wall thickening,and a subsequent combination of sinking without wall thickening, and wall thinning without diameter reduction. The effects on texture of the first two deformation types have been described. In wall thinning without diameter reduction (also called ironing), the plane of strain is the axial (tensile direction) -radial (compressive direction) plane. The expected stable texture corresponding to this deformation consists of basal poles concentrated in the radial direction, and prism poles in the axial direction.

It may be concluded from this qualitative explanation, that the textures produced by all tube cold working processes result in basal poles in the radial-tangential plane and prism poles in the axial direction. The preferred orientation of the basal poles in the radial-tangential plane depends on the process used, and represents a trade-off between effects of sinking type deformation, which produces tangential basal poles, and ironing type deformation, which produces radial basal poles.

This interpretation is in general agreement with experimental observations[20,18,5].

3.2.4 Formability

Texture evolution is determined by the history of strain states or strain path; likewise, the possibility of imposing specified strains

on a preferentially oriented sample of hcp material, is quite dependent on texture.

For instance, the drawabilities of tubing with radial or tangential basal poles are different. Those textures are theoretically stable throughout the drawing process (Fig.10).The drawing force is applied to the material emerging from the die, and a region of high tensile stress concentration results at the point where the tubing leaves the die[8].In the first case (radial basal poles), the material behaviour in the emerging region is of a sinking type (elongation by diameter reduction); if a mandrel or a plug is used, it provides constraint to this deformation; high drawing forces (required for instance by a particularly important reduction) may be sustained by the material. In the second case (tangential basal poles),the tube responds to the stresses in the emerging region, by a wall thinning elongation; failure in drawing occurs for pulling loads much lower than those sustained by the other material; moreover even without failure, this wall thinning after emergence destroys the geometric definition given to the tube by the die and mandrel.

Similar geometric definition problems might well occur also in extrusion for billet textures that would be too far from a fiber texture.

4. TEXTURE CONTROL

4.1 Generalities

Texture control during fabrication is desirable for the first obvious reason that it allows reproducibility of the texture that best suits the required mechanical properties of the cladding. But there is also another important advantage : different deformation paths could be used to reach in the end the texture specified for the cladding. Texture control should lead to the determination of the deformation routes that will facilitate processing, decrease the number of defects, increase mill yields and yet result in the required texture.

Two aspects are relevant for texture control:

- a quantitative method to characterize the deformation routes,
- a quantitative method to characterize the textures.

The correlation between deformation and texture evolution must also include :

- the texture stability conditions,
- the rate of texture change.

4.2 Tubing deformation characterization

4.2.1 Q - factor

The parameter Q, defined as the ratio of the percent reduction in wall thickness divided by the percent reduction in diameter, has been widely used to characterize a reduction step in the manufacture of Zircaloy tubing.

In accordance with the previous rationalization of texture evolution in the tube cold working processes, the relation between Q and

texture appears simple. High values of Q represent ironing deformation, and correspond to a texture with the basal poles closer to the tube normal. Low Q-values represent sinking deformation, and correspond to a texture with mostly tangential basal poles.

However, the Q-parameter was found to be too unprecise a representation of the actual deformation for texture control, for the following reasons:

- Q is not well defined: the diameters considered in diameter reduction calculations were either the inner, outer or mean diameters; the results were naturally not the same.
- Q gives the same global representation of a reduction step or pass whatever sequence of deformation types (sinking with wall thickening, sinking, ironing) has been used, whereas each different sequence, as suggested earlier and actually observed by varying the tooling or process, yields specific textures[5].
- When Q is calculated as a ratio of reductions, i.e as:

$$\frac{(t_i - t_f) / t_i}{(D_i - D_f) / D_i} \qquad (8)$$

it is not independent of the total area percent reduction involved in the pass. In other words, the Q-value calculated between any two points in a pass reduction is not equal to the global Q-value, or two reduction passes, each with a Q-ratio of 2, produce a different overall value[21]. Thus, the intended characterization of a type of deformation depends on the amount of deformation.

Hobson[20] tried to update the concept of the Q-parameter, by

calculating both Q-value and percent reduction in area R_A, at each section along a reduction step (Q-values being referred to the wall and diameter of the entering tube); he then plotted fabrication paths in $Q - R_A$ diagrams. Geometrical consideration allowed him to scale those diagrams with loci of equal diameter and wall reduction. The method was complicated since those loci depended on the starting tube geometry which was used as reference in Q calculations.

One way to solve the dependency of Q-values on the area reduction is to introduce true-strain ratios [22] defined as:

$$Q_{\varepsilon} = \frac{\ln \frac{\text{wall out}}{\text{wall in}}}{\ln \frac{\text{diameter out}}{\text{diameter in}}} \qquad (9)$$

for overall reduction step, or as:

$$Q^{x}_{\varepsilon} = \frac{\ln \frac{\text{wall x}}{\text{wall in}}}{\ln \frac{\text{diameter x}}{\text{diameter in}}} \qquad (10)$$

at any intermediate section x.

Since the texture formation was also to be studied with respect to stability and rate of change, this required to be able to characterize the amount of straining achieved under one deformation type.

The strain ratio did not provide such a possibility, as pointed out by Källström[15], who proposed a more complete deformation analysis in the form of strain paths.

4.2.2 Strain path

Neglecting the redundant and shear deformations in the tube being

reduced, the principal strain directions are the axial, radial and tangential directions; and the strains are:

$$\varepsilon_z = \ln \frac{l}{l_o} \quad ; \quad \varepsilon_r = \ln \frac{t}{t_o} \quad ; \quad \varepsilon_\theta = \ln \frac{\pi d}{\pi d_o} = \ln \frac{d}{d_o} \qquad (11)$$

where l, t and d are the axial length, wall thickness and mean diameter of a doughnut-like element in the tube.

Since the tube may be considered as thin-walled, the doughnut element may simply be taken as a section element of the tube. It must be pointed out that this assumes a uniform deformation through the thickness of the tube. For such a doughnut, t and d are directly measurable at every stage of the deformation.

Plotting (ln t) and (ln d) on two axes of a triaxial plane 120° diagram, for every tube section along the reduction transition, one obtains a curve. The vector $\overrightarrow{AB}$ which joins any two points A and B on the curve has the coordinates:

- on (ln t) axis..... $\ln t_B / t_A = \varepsilon_r^{AB}$
- on (ln d) axis..... $\ln d_B / d_A = \varepsilon_\theta^{AB}$
- on third axis..... $(-\varepsilon_r^{AB} - \varepsilon_\theta^{AB})$, by geometrical property of triaxial 120° diagrams.The constant volume equation for plastic deformation is: $\varepsilon_r + \varepsilon_\theta + \varepsilon_z = 0$; this implies that the coordinate of $\overrightarrow{AB}$ on the third axis is ε_z^{AB}.

The curve is thus a succession of small strain increment vectors; it is called a strain path. The diagram axes are now used to refer vectors. The same proportionnal scale, used to plot (ln t) and (ln d), is now a natural strain scale for $\varepsilon_r, \varepsilon_\theta, \varepsilon_z$. By geometrical property

of the triaxial 120° diagram, the length of a strain increment vector such as $\overrightarrow{AB}$ is related to its coordinates ε_r^{AB}, ε_θ^{AB}, ε_z^{AB}, by:

$$| \overrightarrow{AB} | = \frac{2}{3}\sqrt{(\varepsilon_r^{AB})^2 + (\varepsilon_\theta^{AB})^2 + (\varepsilon_z^{AB})^2} \qquad (12)$$

Comparing with the definition of the effective strain ε_e in plasticity, one sees that : $\overrightarrow{AB} = \varepsilon_e^{AB}$; lengths of strain increment vectors in the diagram, measured with the natural strain scale on the axes, represent the effective strain associated with the strain increment vector.

An easy plotting of strain paths is obtained by using the logarithmic scale derived from the proportionnal strain scale; direct entry of the thichness, t , and mean diameter, d , is then possible. The diagram is shown in Fig.11.

To summarize, the strain path diagram allows:

1) characterization of the amount of deformation between any two points of a reduction transition, by the effective strain.

2) characterization of the type of deformation. The ratio between radial and tangential strains for any deformation increment, is readily reflected by the orientation of the strain vector in the diagram. Källström[15], defines a strain ratio, α, as the angle clockwise from the positive ε_z - axis to the direction of the strain vector. (Table 4)

4.3 Tube texture characterization

The textures produced by the types of deformation encountered in tubing cold working, consist of basal poles oriented in the R-T plane, with generally two marked preferred orientations in this plane at $\pm \Phi_{max}$ to the radial direction.

Different investigators have proposed various parameters to characterize the position and sharpness of the density peaks.

The simplest one is the angle between the radial direction and the maximum recorded intensity in the R.T plane in a direct basal pole figure.

A more precise representation of the distribution of basal pole density in the R.T plane was proposed by Dahl Mc Kensie & Schemel[23]. They plot the basal pole density, N, recorded in the R.T plane, versus the inclination Φ to the radial direction.Considering this plot as a statistical distribution of Φ with the basal pole densities as relative frequencies (with correct normalization), they define:

$$\text{First Moment (FSTM)} = \sum_{i=1}^{m} N_i \Phi_i \Big/ \sum_{i=1}^{m} N_i \qquad (13)$$

$$\text{Second Moment} = \sum_{i=1}^{m} N_i \Phi_i^2 \Big/ \sum_{i=1}^{m} N_i \qquad (14)$$

$$\text{Standard Deviation (S)} = \sqrt{(\text{Second Moment}) - (\text{First Moment})^2} \qquad (15)$$

N_i and Φ_i values are from one side only of the radial direction in the R-T plane. This method gives the mean and standard deviation of one of the basal pole density peak, in that plane.

Hobson[20] uses a parameter M corresponding to Dahl et al.'s first moment.

As pointed out by Knorr[16], Dahl et al.'s formulae could as well incorporate Φ values from both sides of the radial direction, on condition to affect them with the same sign.In this manner, an averaged value of the mean and standard deviation for both peaks can be obtained.

Knorr also proposed to consider a distribution of $\sin \Phi$ rather than that of Φ .His parameters are:

$$\text{First Moment } \left(\frac{s1}{s0}\right) = \int_{-\pi/2}^{+\pi/2} I(\Phi).|\sin\Phi|.d\Phi \Big/ \int_{-\pi/2}^{+\pi/2} I(\Phi).d\Phi \qquad (16)$$

$$\text{Second Moment}\left(\frac{s2}{s0}\right) = \int_{-\pi/2}^{+\pi/2} I(\Phi).\sin^2\Phi.d\Phi \Big/ \int_{-\pi/2}^{+\pi/2} I(\Phi).d\Phi \qquad (17)$$

$$\text{Standard Deviation (S.D)} = \sqrt{(\text{Second Moment}) - (\text{First Moment})^2} \qquad (18)$$

Källström et al.[24] proposed still another texture factor to characterize the basal pole densities in the R.T plane. It is defined as:

$$F = \int_{-\pi/2}^{+\pi/2} I(\Phi).\cos 2\Phi.d\Phi \Big/ \int_{-\pi/2}^{+\pi/2} I(\Phi)d\Phi \qquad (19)$$

This definition implies a value F=1 for all radial basal poles and F=-1 for all tangential basal poles.

The global texture characterization, analytically developped by Roe[14], allows a more complete representation of textures and of their evolution. Källström[15] used it in the following way; symmetry considerations allow him to consider essentially three terms in the generalized spherical harmonics expansion of the global crystallite orientation distribution function $w(\varphi, \omega, \psi)$;

- a term of coefficient w_{000} corresponding to an average distribution,

a constant value for textured and non textured material.

-two terms of coefficients w_{2oo} and w_{22o} which express the main features of the deviation from randomness, as for basal pole preferred orientation.

Källström represents the textures in a $w'_{2oo} - w'_{22o}$ diagram (w'_{2oo} , w'_{22o} are proportionnal to w_{2oo}, w_{22o}.) In this diagram, any particular basal pole texture is represented by a point; the center $w'_{2oo} = w'_{22o} = o$ corresponds to random basal pole texture. The extreme quasi single crystal basal pole textures are represented by the three summits of an equilateral triangle inside which any intermediate texture is representated. (Fig. 12). Källström defines any texture representative point by its polar angle to the w'_{2oo} axis:

$$\eta = \arctan (- w'_{22o} / w'_{2oo}) \qquad (2o)$$

called texture ratio, and the distance to the origin :

$$w = w'^{2}_{2oo} + w'^{2}_{22o} \qquad (21)$$

called texture sharpness.

4.4 Previous texture control investigations.

Tenckhoff and Rittenhouse [18], Hobson [17,2o] and Källström [5,15] have investigated possible correlations between fabrication methods and textures.

Tenckhoff and Rittenhouse limited their studies to an observation of the texture (direct pole figures), related to the global Q-factor of the deformation; they confirmed the rule of thumb that high Q-values are related to high radial basal pole density, and low Q-values to high tangential basal pole density. They also demonstrated the texture gra-

dients through the wall of tubings, using a thin foil technique to obtain their X-ray specimen.

Hobson[20] characterized the plastic deformation by using a strain ratio type of Q-factor, Q_{ε}, and representing the amount of deformation by the reduction in area. He made a three dimensionnal plot of a texture parameter M, analogous to the first moment defined in Eq. (13), versus the strain ratio and reduction in area. His experiments[17] also pointed out texture gradients around the circumference of tubings and he suggested that the gradients were introduced by deformation inhomogeneities inherent to the tube reducing process.

A relation between types of deformation, or strain ratios, and associated stable textures is proposed by Källström[15] in the form of a texture rose (Fig.13).

The $(w'_{200} - w'_{22o})$ texture diagram quantitatively defines the texture rose, and in addition, provides a means of differentiating between texture sharpness. In this diagram, texture paths may be plotted and texture evolutions to stability may be followed. Källström[15] observed that "a texture path is parallel to its corresponding strain path until one of the triangle sides is approached, where the texture-path deviates to become parallel to the projection of the strain path on the triangle side." Källström also evaluated an approximate texture-change rate:

$$\Delta w / \Delta \varepsilon_e = 1.7 \cos (\alpha - \Delta \eta)$$

where Δw represent the length of an increment on the texture change path.

5. EXPERIMENTAL PROCEDURES AND RESULTS

5.1 Materials used.

Two Zircaloy-4 tubing reduction transitions were analyzed in details in this work.

The two tube transitions were from the same batch of Zircaloy-4 made by the Teledyne Wah Chang Company.These tubes were provided by a tubing manufacturer*, and corresponded to two different cold work stages performed on different machines; a Russian HPTR rocking roll reducer with three rolls and a cylindrical mandrel (Fig.14),and a Mc Kay-Mannesman 25VMR two rolls reducer with a tapered mandrel.(Fig.15)

5.2 Deformation characterization.

The strain paths were determined for both reduction transitions. External and internal diameters were measured along the transitions using appropriate gauges and a caliper.Measurements were made in the same axial-radial plane.Two profiles were obtained (Fig.16 & 17). Direct plotting of mean diameters and wall thicknesses yielded the strain paths in Fig.18.

Also, various global Q-values, displayed in Table 5 were calculated according to the various definitions mentionned in section 4-2-1. The reduction in area was determined along the reductions (also referred to,here,as cones) and plotted in Fig.19.

* the name of the manufacturer is withheld for proprietory reasons.

5.3 Texture Measurements

5.3.1 Specimen preparation

Nine and ten samples were cut from the cones at axial locations represented in Fig.16 & 17. Specimens for X-ray diffraction were obtained by the thin foils technique[18,16].Two cm lengths of the cone at the sampling axial locations,were machined on a lathe to obtain rings·of 2/10 mm wall thickness. These rings were taken at depths in the wall corresponding to the same layer of deformed material; depth correspondance was based on the assumption that the ratio of the cross sectional areas on each side of the chosen circumference should be constant during deformation[20]. The ratio selected for the two cones was that corresponding to a mid-wall circumference in the starting tube.

The depth location of each sample is shown in Fig.16 &17; very small variations from mid-wall position were in fact introduced by the above constant layer considerations.

After chemical thinning of the sample rings in a fluonitric solution (10% HF, 40% HNO_3, 50% H_2O), to about 1/10 mm in thickness,elastic unrolling was possible. Chemical thinning had moreover removed the cold work layers introduced by sample machining. The samples were then glued to a stiff plexiglass backing to form a flat X-ray specimen.

5.3.2 Inverse pole figures.

Inverse pole figures were determined for the flat sheet specimens. In all cases, the reference direction was the normal to the flat sheet i.e the radial direction of the tube. A General Electric diffractometer was used. The operating conditions of the diffractometer were:

- Cu K_α radiation
- Cu K_β eliminated by a Ni filter
- X-ray tube voltage of 35 kV
- 3° div. slit
- .2° receiving slit
- measurement time constant of 1 sec.

All the diffracting planes for Bragg angles between 15° and 75° were considered (Table 2); texture coefficients were calculated.

5.3.3 Direct pole figures.

Direct pole figures were determined by reflection, on a Siemens pole figure diffractometer. The crystallographic plane considered was the basal plane.

In the gonio stage, the sample was tilted (Φ variation) at the rate of 1°/min, while being rotated in its own plane (δ variation) at 72°/min. The basal pole orientations scanned, thus belonged to a spiral with a 5° pitch on the stereographic projection (Fig.9).

The diffraction operating conditions were the same as for the inverse pole figure determination. The incident beam irradiated a square of 15 mm side on the specimen, for every orientation.

The range of Φ angles covered with the reflection method was 0° to 75° or 80°. Beyond 80°, defocusing of the incident beam made the signal merge into the background radiation.

Intensities were corrected for defocusing at increasing Φ angles, using the methods and data given in appendix [16]. Conversion of intensities into basal pole densities was obtained using the textu-

re coefficients calculated from the inverse pole figure experiments. The most representative direct pole figures obtained for the two cones are displayed in Fig. 20 to 28.

5.4 Texture characterization.

Kearn's [13] parameter, f , defined in section 2-5-1-4 was calculated for each specimen, using 30 inclination bands for each of which an average basal pole density was obtained from texture coefficients interpolation. f-values for the two reductions are presented in Table 6; plots of f, versus the effective strain, ε_e, and the strain ratio, α, defined in section 4-2-2, are shown in Fig.29 & 30.

The basal pole density in the R-T plane was analyzed from direct pole figures experiments. Plots of the basal pole density, versus the inclination Φ to the radial direction, were made for each specimen and have been called R-T scans. Fig. 31 & 32 show perspectives of these R-T scans versus the axial location of the specimen along the cone axis.

For each R-T scan , the mean (sl/so) and standard deviation (S.D.) of the $\sin\Phi$ distribution, with the normalized basal pole densities as relative occurrence frequencies, were calculated according to Eq.16,17, 18.

The texture factor, F , defined in Eq. 19, was also determined.

Results for sl/so, S.D and F are presented in Table 6. Plots versus ε_e and α are shown in Fig.33 to 38 .

5.5 Circumferential texture gradients.

In order to observe the influence on circumferential texture gradients, of the two different tooling designs used for the two reduc-

tions, the following experiments were made.

For each cone, one specimen was chosen in the zone of deformation without mandrel support, and another one in the zone of deformation with mandrel support.

A small .4° diverging slip was used on the G.E diffractometer, to obtain inverse pole figures from very small areas of the same specimen at distances apart corresponding to 60° (3 rolls HPTR) and 90° (2 rolls 25VMR), on the same circumference.

Several of the inverse pole figures obtained are displayed in Fig. 39 to 41 .

Kearn's parameters were also calculated, and have been plotted at the corresponding circumferential locations in Fig.42 & 43.

6. DISCUSSION

6.1 Deformations

Both reductions start with a short sinking stage bringing the inner surface of tube to contact with the mandrel (Fig.16 & 17).The strain ratio associated with this sinking deformation, is represented by a strain path orientation (Fig.18) approximately parallel to the ($-\varepsilon_\theta$) axis ($\alpha = -30°$). Deviations from this orientation correspond to wall thinning at the very beginning of deformation ($\alpha > -30°$) and to wall thickening ($\alpha < -30°$) afterwards.

In the case of the HPTR reduction, a pure ironing deformation follows the sinking stage. The pure type of this deformation appears in the strain path which becomes a straight line almost parallel to the ($-\varepsilon_r$) axis. Ironing deformation is less and less severe as a section proceeds towards the end of the reduction; this is evidenced by the profile (Fig. 16) and the reduction in area plot (Fig. 19), but it also appears in the strain path,on which the proceeding section representative point moves slower and slower.

The 25 VMR reduction shows a severe wall thinning in the sinking zone, prior to wall thickening. This important wall thinning is probably due to a particularly severe sinking. The reversal thinning-thickening gives a weird aspect to the profile.The deformation with mandrel support is for the main part a combination of sinking and ironing,with more ironing at the beginning and more sinking at the end, as shown by a slight orientation variation in the strain path (Fig. 18).

An interesting feature of the end of the deformation is revealed by the strain path. A marked wall thickening occurs at reaching the calibration zone of the final tube. This reverses the orientation of the strain path and brings it parallel to (ε_r) which is characteristic of wall thickening with equal shortening and diameter contraction. (Table 4). It is suggested that this is a deformation anomaly, introduced by an improper position of the mandrel; indeed a slight withdrawal of the mandrel would have eliminated this thickening.

6.2 Texture rotation

The strain paths thus allow a detailed characterization of the deformation in the two cases analyzed. The texture evolutions have been related to the strain paths.Qualitatively, the evolution of the textures in both cases is in accordance with the texture rose (Fig.13).Every change of orientation on the strain path is observed to correspond to a displacement of the basal pole density peaks in the R-T plane, in the direction ascribed by the texture rose. (Fig. 20 to 28, Fig.31 , Fig. 32).

The various texture parameters analyzed , f , s_1 / s_0 ,S.D, and F, have been plotted versus the two quantitative deformation parameters associated with the strain path, i.e the strain ratio, α ,and the effective strain, ε_e, defined in section 4.2.2. Those parameters were measured on the strain path and are somewhat approximative. When the strain path segment associated with a specimen (Fig.18) was undergoing pronounced orientation changes (e.g sample 25 VMR-2), the α-value associated with the origin of the segment was chosen because

it was considered that texture rotation was a delayed effect of the setting of a certain strain ratio;hence, the α-value selected for the 25 VMR-2 sample was ($-40°$) and not ($+25°$). The effective strain value, ε_e, corresponds to the curvilinear abscissa, on the strain path, of the midpoint of the segment associated with a specimen. Table 7 displays the values of α and ε_e so evaluated.

The plots obtained (Fig.29 & 30, Fig. 33 to 38) suggest the following observations:

1) The dependencies of the texture factors f, F, s_1/s_o, on the strain ratio α , exhibit larger and larger increases (f, F),or decreases(s_1/s_o) as α varies from $-120°$ to $+30°$. This is in agreement with the evolution of stable textures proposed in the texture rose (Fig.13) for this α-variation, and with the nature of the texture factors which all are most sensitive to rotation of the basal pole density maxima towards the radial direction.

2) Two data points appear at erratic locations in the plots of f, F and s_1/s_o, versus α , for the 25 VMR reduction; these correspond to specimens 25 VMR 1 and 25 VMR 3 for which the following interpretation is proposed: textures in those specimens are not yet stable relative to the respective strain ratio ; specimen 3 is an especially clear case that mostly retains the features of texture in specimen 2, i.e of a somewhat stabilized texture corresponding to $\alpha = -40°$. The important delay for texture rotation and stabilization between specimen 25 VMR 2 and 25 VMR 4, and the lack of such delay for the other α-changes suggest that texture rotation requires more effective strain when

the tube wall is thicker.

3) The difference between texture parameters F and s_1 / s_0 on one hand, and f on the other hand, is illustrated by considering the texture factors associated with specimens 25 VMR In and 25 VMR 1.Texture in 25 VMR 1 differs from texture in 25 VMR In by:

a) a general strengthening of the basal pole density in the R-T plane,

b) a slight rotation of the density peaks in the plane towards the tangential direction.

The variations of texture factors F and s_1/s_o reflect the second aspect; this is in accordance with the definitions of these texture factors, which make them sensitive to the location of basal pole density peaks in the R-T plane, irrespective of the texture strength.

The opposite variation of Kearn's parameter, f, reflects the first aspect of the texture variation. f is thus sensitive to general strengthening of the texture in the R-T plane; but this sensitivity is combined to a sensitivity to texture rotation, as demonstrated by trends generally similar to those of F.

This might be summarized in stating that F, and s_1/s_o are exclusively sensitive to texture rotation (in the R-T plane), while f incorporates some sensitivity to texture formation.

4) The specific effect of ε_e appears for specimens HPTR 4 to HPTR 7,and 25 VMR 4 to 25 VMR 6, two series with constant strain ratios (25° and 15°).

In the HPTR case, the texture evolution observed is a marked and steady sharpening of the density peaks with only very slight displacements of

the peaks in the R-T plane (Fig. 31).

In the 25 VMR case, the texture evolution is a less pronounced sharpening with some instability in the Φ-locations of the density peaks (Fig.32).

In both cases, the specimen 4 shows peaks slightly closer to the radial direction but a much weaker texture than the following specimen.

Kearn's parameter ,f, reflects essentially the steady sharpening evolution while F and s_1/s_o trends follow the slightest peak displacements.

5) The basal pole density peak sharpness parameter S.D does not show any dependence on α. Its variations in Fig.37 are readily interpretable in relation with the events in the strain paths: marked peak broadening (S.D increase) occurs at locations where severe α changes bring massive basal pole reorientations; sharpening (S.D decrease) occurs whenever a stabilized texture is attained under any strain ratio and when further deformation goes on without α-change.

Thus the combination of S.D and F or S.D and s_1/s_o describes both texture rotation in the R-T plane and texture sharpening.

We have seen that Kearn's parameter, f, somehow incorporates those two characterizations of texture evolution.

6.3 Circumferential texture gradients.

Hobson[17] measured texture gradients in the circumferential direction using a device that allowed continuous scanning of (0002) reflections along a circumference.He observed periodic variations with fre-

quent six fold peaks, and suggested that these peaks were introduced as follows: the actual deformation in tube reducing is not homogeneously axisymmetric. After each stroke of the rolls, a small feed is imparted to the tube which is also rotated; a different point of a section circumference is brought in the plane of each roll where more compression occurs; Hobson suggested that these localized heavier compressive strains resulted in a higher density of radial basal poles at the location of the impact.

The measurements made in this work have been different in that they were not continuous recordings, and also in the fact that specimen were taken from the reducing part and not from the final tube obtained from a pass. However, a periodicity is observed, especially in the case of the 25 VMR reduction with two rolls. Only two peaks are observe which suggests that under heavy deformation, the effects of previous roll strokes on texture is completely offset. An ill defined periodicity in the HPTR case is in accordance with a higher degree of axisymmetry provided by three rolls instead of two.

7. CONCLUSION

The processes for Zircaloy tube manufacturing have been reviewed and the specific deformation routes have been analyzed in terms of the operating deformation systems in the material.

Methods for texture characterization and parameters for texture-change evaluation have been summarized.

Two different reduction transitions of Zircaloy-4 tubing were used to analyze texture formation and rotation in relation to the deformations. The deformations were characterized by strain paths, obtained from profile measurements; the textures were represented by direct and inverse pole figures, from which various texture factors F, s_1/s_o , S.D, and f were derived.

The results illustrate the interest of the strain path for the analysis of tubing deformations.

The strain paths and the pole figures obtained corroborate the texture rose theory on texture rotation.They also show that small changes in the orientation of strain paths may result in pronounced texture changes.

The evolutions of the texture parameters f, F, s_1/s_o and S.D have been referred to two deformation parameters derived from the strain paths: the strain ratio α , and the effective strain ε_e . Analyzing the texture evolutions in terms of rotation of the basal pole density peaks in the R-T plane, and in terms of texture strengthening and sharpening in the R-T plane, the respective sensitivities of the textu-

re factors have been evaluated. The sensitivity of the F factor and of the first moment, s_1/s_0, to density peak rotation and the sensitivity of the standard deviation, S.D , to the sharpness of the density peaks have been observed, in accordance with the definitions of those parameters. Kearn's parameter, f , has been found to show an interesting sensitivity to both texture rotation and texture strengthening which seems to be convenient for texture-change characterizations.

The influence on texture of the deformation inhomogeneities neglected in the strain path approach has been studied by characterizing the circumferential texture gradients obtained on the two reductions. Reasonable agreement has been observed with Hobson's analysis of deformation inhomogeneities and related circumferential texture gradients.

REFERENCES

1. S. KAAS The development of the Zircaloys.

2. C.E.ELLS ASTM STP 551 (1974),311.

3. D.L.DOUGLASS, The metallurgy of Zirconium,
International Atomic Energy Review, Vienna (1971).

4.B.D LICHTER Trans. AIME 218 (1960), 1015.

5. K. KALLSTROM , Scandinavian Journal of Metallurgy 4 (1965), 75.

6. G. OSTBERG , Journal of Nuclear Materials 7 (1962), 103.

7. E. TENCKHOFF, ASTM STP 551 (1974), 179.

8. M. PICKLESIMER, ORNL- TM 460 (1963).

9. R.G BALLINGER , SM thesis M.I.T(1977)

10. G.B HARRIS , Phil. Mag., 43 series 7, 113 (1952)

11.E.F STURKEN & W.G DUKE AEC.DP 607 (1961)

12 B.A CHEADLE , C.E. ELLS, W. EVANS , J. of Nuclear Materials
23 (1967) ,199.

13 J.J. KEARNS - WAPD TM 472 (1965)

14. R.J.ROE,J. of Applied Physics vol. 36 N°6 (1965) , 2024

15. K.KALLSTROM, Canadian Metallurgical Quaterly
vol. 11, 1 (1972) ,185.

16.D.B. KNORR SM thesis M.I.T (1977)

17. D.O. HOBSON ASTM STP 458 (1969), 37.

18. E. TENCKHOFF and P.L RITTENHOUSE . ASTM STP 458 (1969),50.

19 M. PICKLESIMER. J.of Electrochem.Tech. vol4 (1966), 289.

20.D.O. HOBSON - ORNL TM 3500 (1971).

21. J.H. SCHEMEL & R.W. McKENSIE , ASTM STP 551 (1974), 169

22. F.C. EDENS, ASTM STP 551 (1974), 177.

23. J.M.DAHL, R.W McKENZIE & J.H SCHEMEL , ASTM STP 551 (1974);147

24. K. KALLSTROM , T. ANDERSON & A. HOFVENSTAM, ASTM STP 551 (1974);160.

25. B.F. DECKER, E.T. ASP, and D. HARKER, J. Appl. Phys.,19 (1948), 388.

26. L.G. SCHULZ, J. Appl. Phys. , 20 (1949), 1030.

TABLE 1

ZIRCONIUM BASED ALLOYS CHEMICAL COMPOSITIONS

Alloy element	Zircaloy-2 wt.%	Zircaloy-4 wt.%	Zr-2.5 Nb wt.%
Tin	1.20 - 1.70	1.20 - 1.70	-
Iron	0.07 - 0.20	0.18 - 0.24	0.150
Chronium	0.05 - 0.15	0.07 - 0.13	0.020
Nickel	0.03 - 0.08	0.0070	0.0070
Fe+ Cr + Ni	0.18 - 0.38	0.28 - 0.37	-
Niobium	-	-	2.40 - 2.80
Oxygen	(a)	(a)	0.09 - 0.13

Reference: ASTM Standard Specification for Zirconium and Zirconium alloy ingots for nuclear application B 350-73

(a) oxygen has a strengthening effect on Zircaloys; its concentration may be specified.

TABLE 2

SUMMARY OF DATA PERTINENT TO X-RAY ANALYSIS OF ZIRCONIUM ALLOYS

(hkil)	2 (CuKα)	Relative Intensity[11] (I/I)	Tilt Angle from (0002) Φ_{hkil}
$10\bar{1}0$	32.00°	24.3	90°
0002	34.84°	25.5	0°
$10\bar{1}1$	36.56°	100	61.4°
$10\bar{1}2$	48.02°	14.6	42.5°
$11\bar{2}0$	57.04°	16.6	90°
$10\bar{1}3$	63.60°	17.3	31.5°
$11\bar{2}2$	68.5°	18.0	57.8°
$20\bar{2}1$	69.7°	12.9	74.8°
0004	73.63°	2.41	0°
$10\bar{1}4$	82.5°	2.69	24.7°
$20\bar{2}3$	90.64°	6.63	50.7°
$21\bar{3}0$	93.6°	2.10	90°
$21\bar{3}1$	96.18°	12.2	78.4°
$11\bar{2}4$	100.0°	7.73	38.5°
$21\bar{3}2$	104.03°	3.79	67.6°
$10\bar{1}5$	105.91°	5.62	20.2°
$21\bar{3}3$	117.83°	11.6	58.3°
$30\bar{3}2$	123.09°	8.10	70.1°
$20\bar{2}5$	136.85°	7.50	36.3°
$10\bar{1}6$	140.16°	-	17°
$21\bar{3}4$	141.36°	-	50.6°

TABLE 3

PROCESS FLOW SHEET FOR PRODUCTION OF ZIRCALOY TUBING

Stage	Operations
Melting	Pressing of Zr sponge and alloy additions into briquettes.
	Welding of briquettes into electrodes.
	Melting / Remelting — High vacuum electric are consumable electrode.
Hot working	Hot forging in upper α-range .
	Heating to β-range and quenching.
	Extrusion in upper α-range.
Cold working and annealing	Cold rolling .
	Annealing in upper α-range.
	Cold rolling .
	Annealing.
	Final cold rolling 50 - 80% .
	Final annealing 475- 575°C.
	Straightening.

TABLE 4

Strain ratio	Deformation type
$\alpha = 0°$	Elongation with equal wall thinning and diameter contraction.
$\alpha = 30°$	Elongation with constant diameter.
$\alpha = 60°$	Wall thinning with equal expansion and elongation.
$\alpha = 90°$	Expansion with constant length.
$\alpha = 120°$	Expansion with equal shortening and wall thinning.
$\alpha = 150°$	Expansion with constant wall thickness.
$\alpha = 180°$	Shortening with equal wall thickening and expansion.
$\alpha = -150°$	Shortening with constant diameter.
$\alpha = -120°$	Wall thickening with equal diameter contraction and shortening.
$\alpha = -90°$	Diameter contraction with constant length.
$\alpha = -60°$	Diameter contraction with equal elongation and wall thickening.
$\alpha = -30°$	Elongation with constant wall thickness.

TABLE 5

Q-values

	25 VMR	HPTR
Initial geometry OD * t	19.02 * 2.26	11.08 * 1.13
Final geometry OD * t	11.0 * 1.05	9.58 * 0.65
$Q_1 = \frac{(t_s - t_f)/t_s}{(D^o_s - D^o_f)/D^o_s}$	1.27	3.14
$Q_1 = \frac{\ln t_s / t_f}{\ln D^o_s / D^o_f}$	1.40	3.80
$Q_2 = \frac{(t_s - t_f) / t_s}{(D^m_s - D^m_f) / D^m_s}$	1.32	4.14
$Q_2 = \frac{\ln t_s / t_f}{\ln D^m_s / D^m_f}$	1.47	5.11
$Q_3 = \frac{(t_s - t_f)/ t_s}{(D^i_s - D^i_f)/ D^i_s}$	1.39	6.94
$Q_3 = \frac{\ln t_s / t_f}{\ln D^i_s / D^i_f}$	1.57	8.75

s, f, are for starting and final.

o, m, i, are for outer, mean and inner.

TABLE 6

TEXTURE PARAMETERS RESULTS

Specimen	f	$^{s}1/s_{0}$	S.D	F
HPTR IN	0.533	0.59653	0.2903	0.1197
1	0.535	0.58644	0.2915	0.1422
2	0.537	0.58931	0.2922	0.1346
3	0.501	0.60523	0.2883	0.1012
4	0.606	0.56598	0.2773	0.2056
5	0.645	0.56604	0.2695	0.2139
6	0.658	0.54244	0.2614	0.2749
7	0.667	0.53940	0.2609	0.2819
OUT	0.656	0.56400	0.2633	0.2252
25 VMR IN	0.400	0.59944	0.2907	0.1123
1	0.492	0.63187	0.2831	0.0412
2	0.431	0.67914	0.2622	-0.0599
3	0.433	0.67367	0.2623	-0.0453
4	0.472	0.64523	0.2719	0.0195
5	0.477	0.65222	0.2703	0.0031
6	0.489	0.65345	0.2680	0.0023
7	0.468	0.65464	0.2701	-0.0031
8	0.420	0.68437	0.2616	-0.0736
OUT	0.448	0.68887	0.2588	-0.0831

TABLE 7

DEFORMATION PARAMETERS DERIVED FROM THE STRAIN PATHS

Specimen	e	α
HPTR IN	0	-
1	0	-
2	0.015	0°
3	0.05	-45°
4	0.30	+25°
5	0.51	+25°
6	0.70	+25°
7	0.72	+25°
OUT	0.75	-
25 VMR IN	0	-
1	0.07	-40°
2	0.34	+15°
3	0.54	+15°
4	0.89	+15°
5	1.09	+15°
6	1.26	+15°
7	1.44	- 2.5°
8	1.55	-120°
OUT	1.55	-

Summary of Important Planes and Directions for HCP Crystal Structure

FIGURE 1

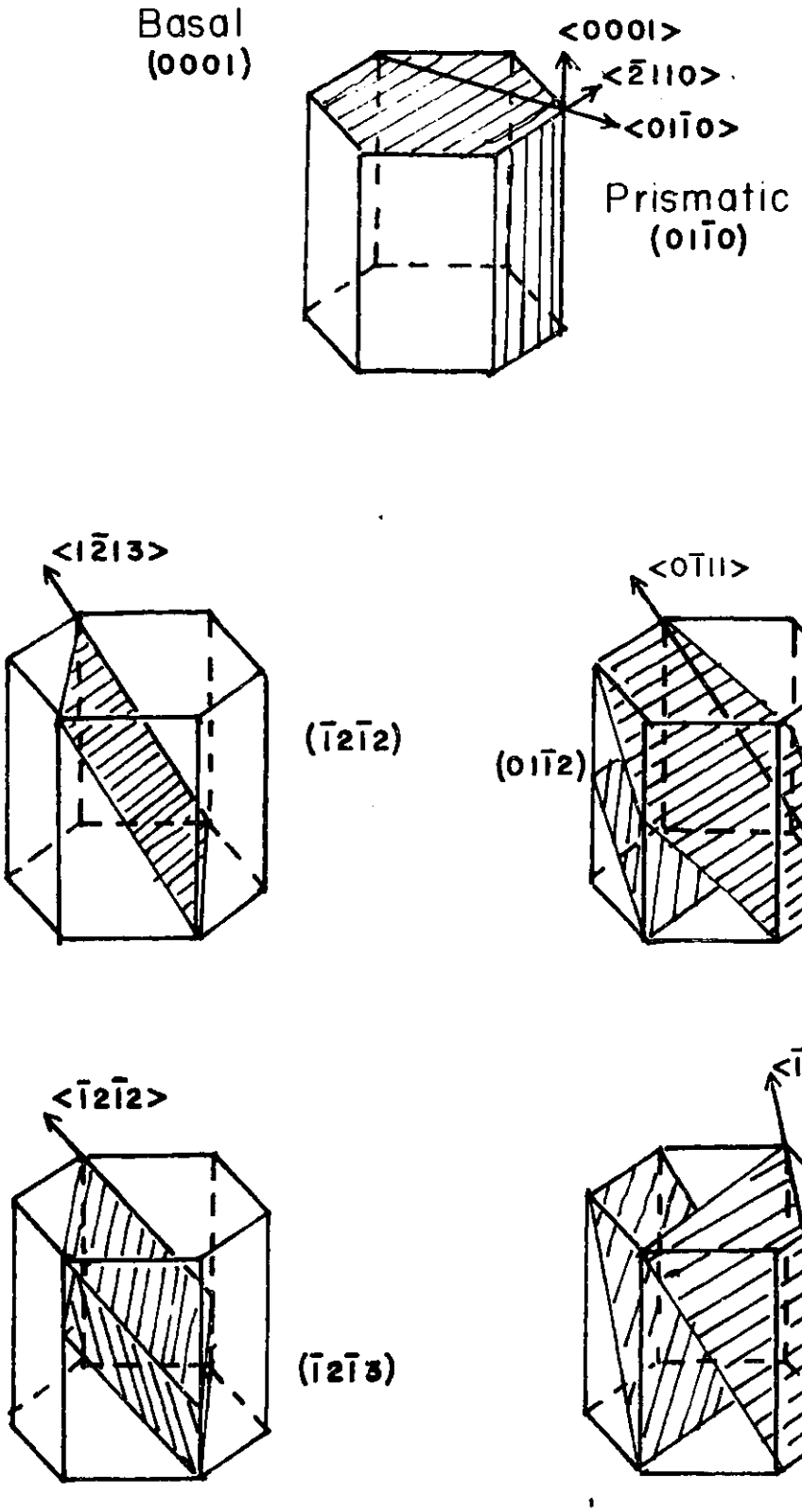

FIGURE 2a

SLIP SYSTEMS IN ZIRCONIUM

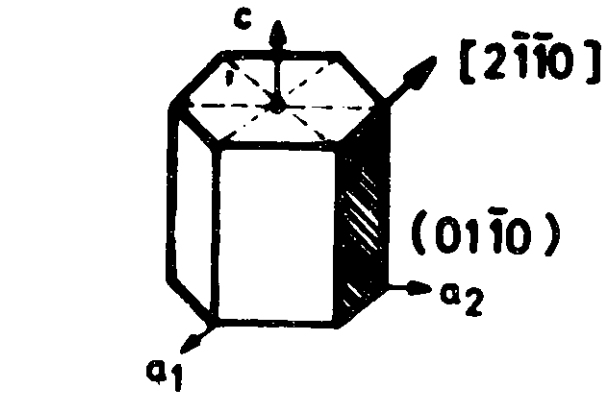

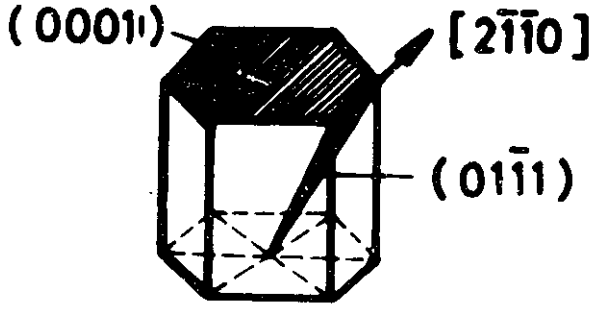

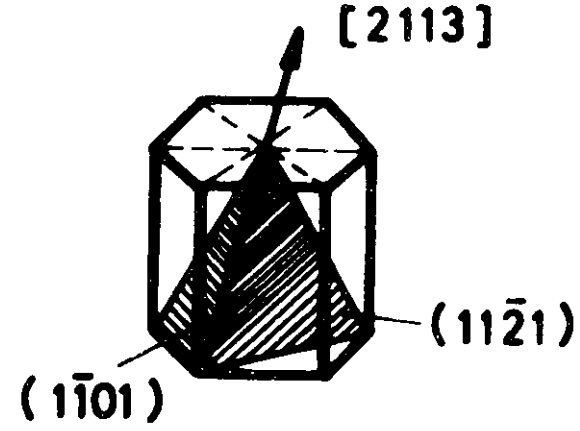

F I G U R E 2 b

TWINNING SYSTEMS IN ZIRCONIUM

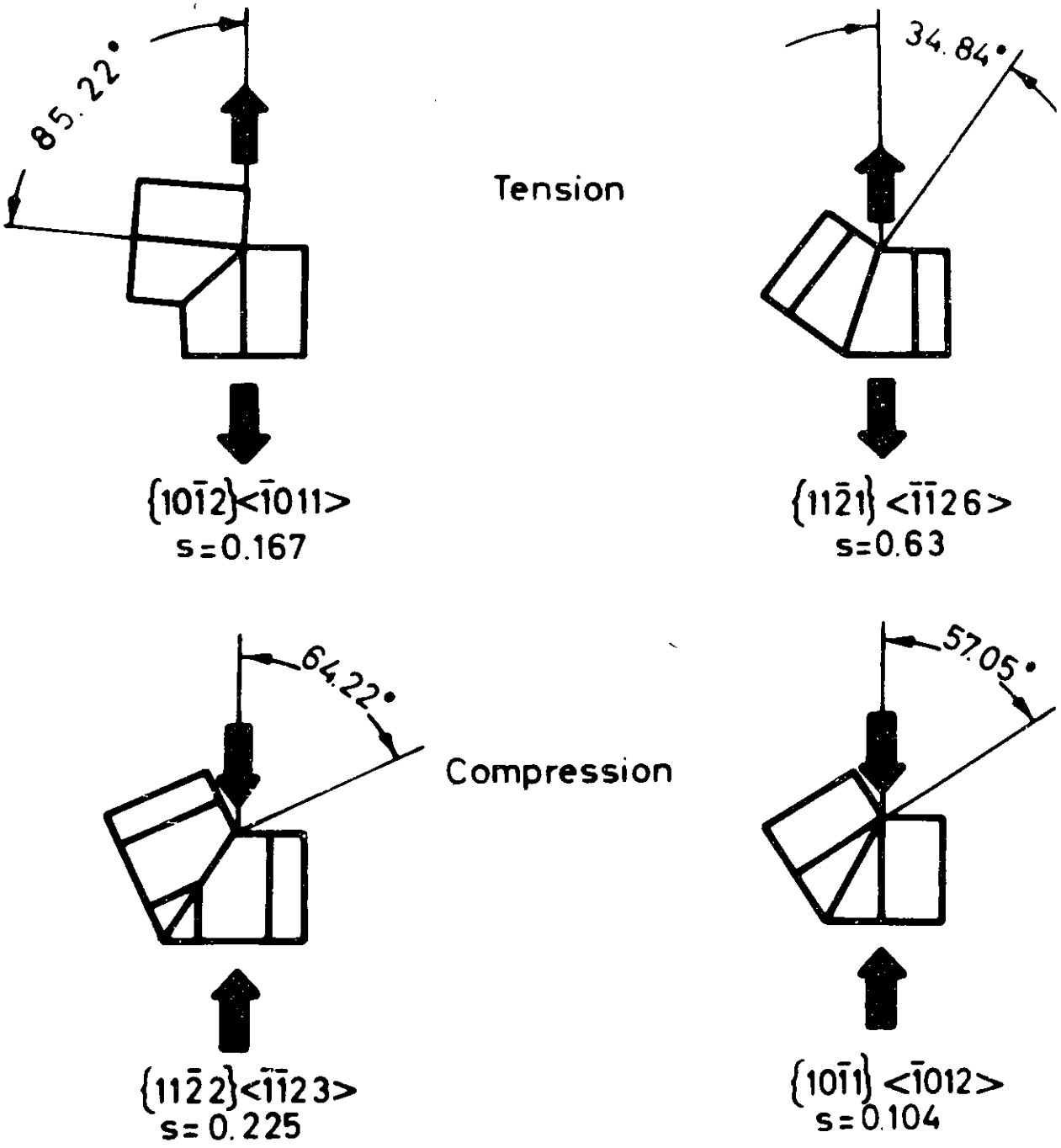

FIGURE 3

QUASI-SINGLE CRYSTAL TENSILE SHEET SPECIMENS OF ZIRCALOY-2

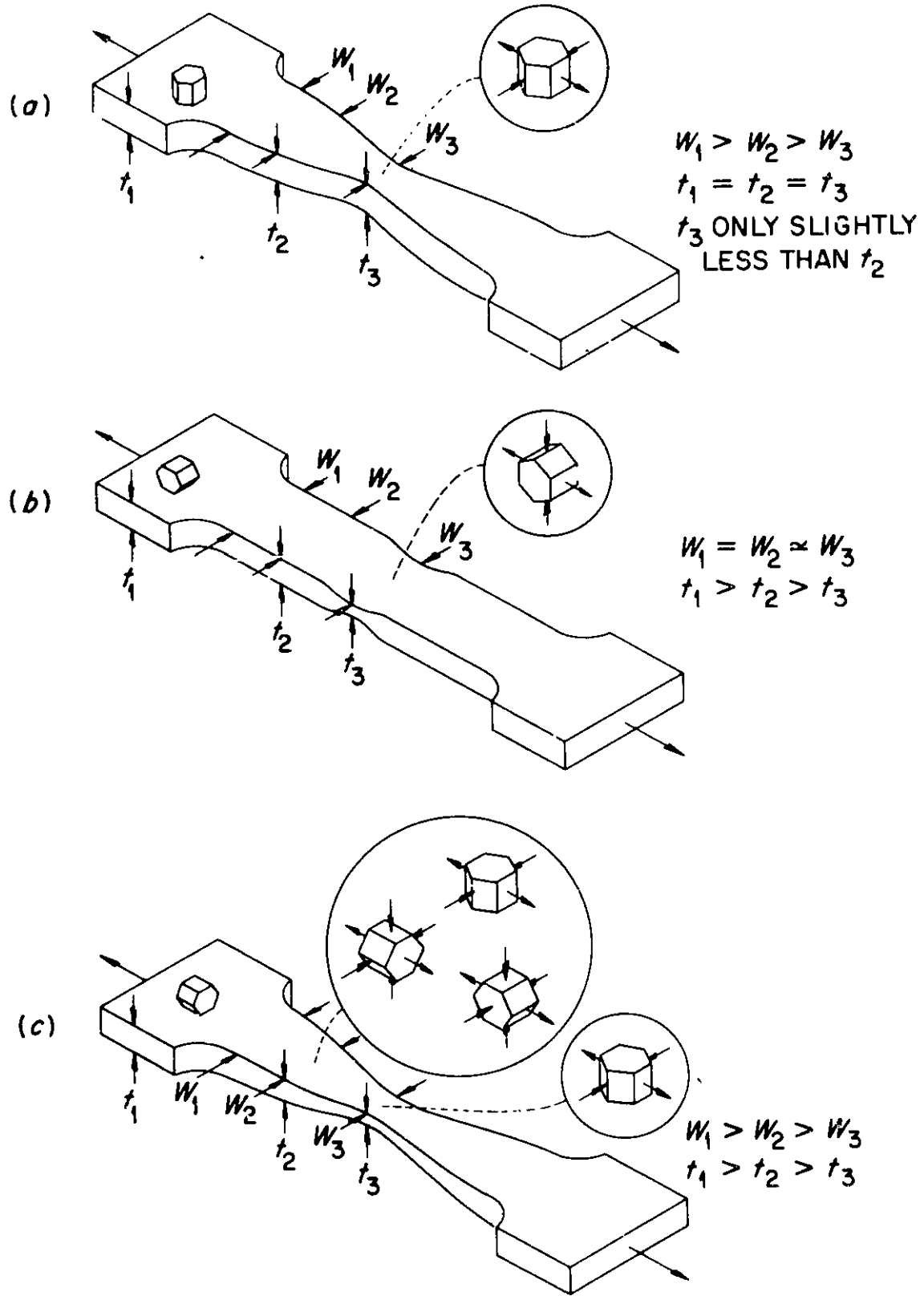

F I G U R E 4

BASAL POLES LOCUS FOR CRYSTALLITES GIVING AN (hkil) REFLECTION

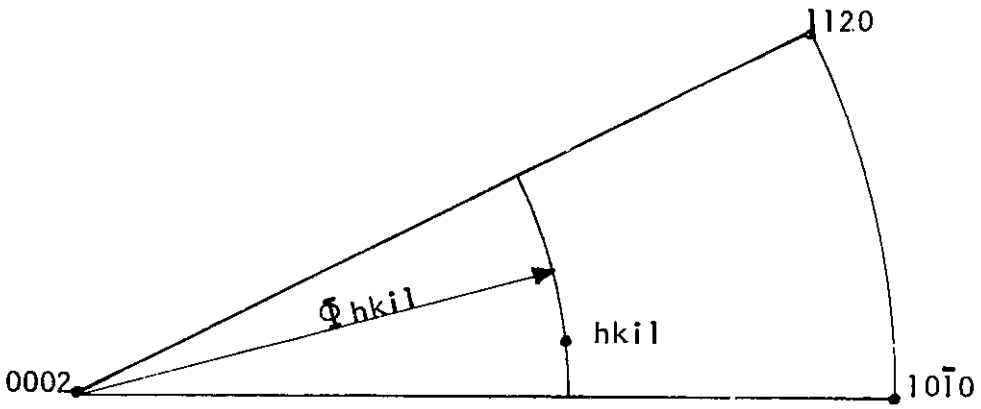

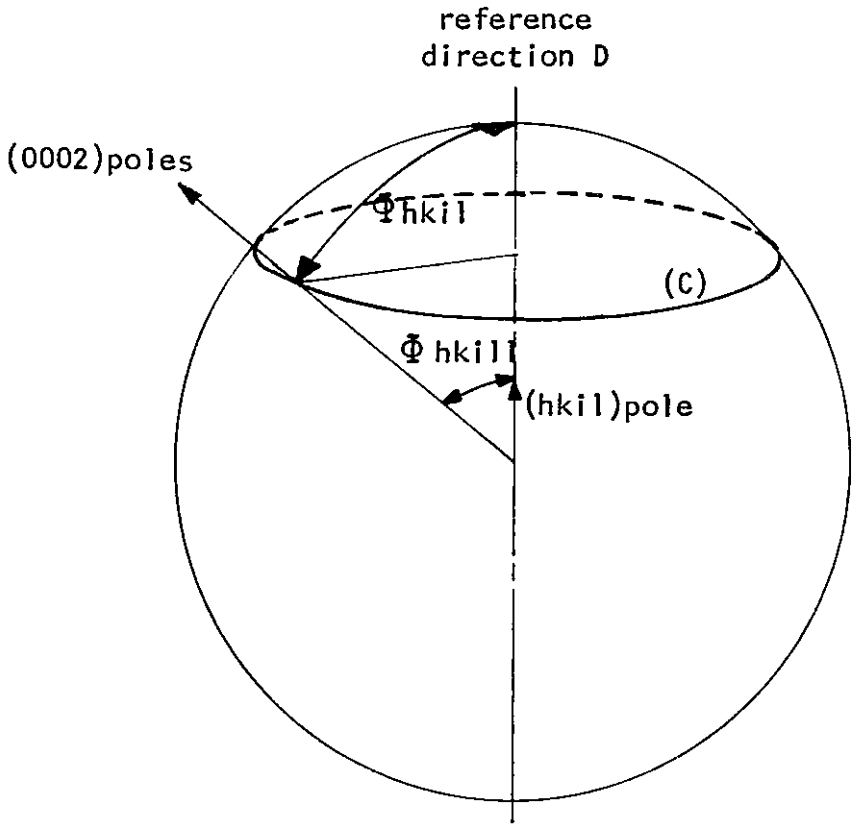

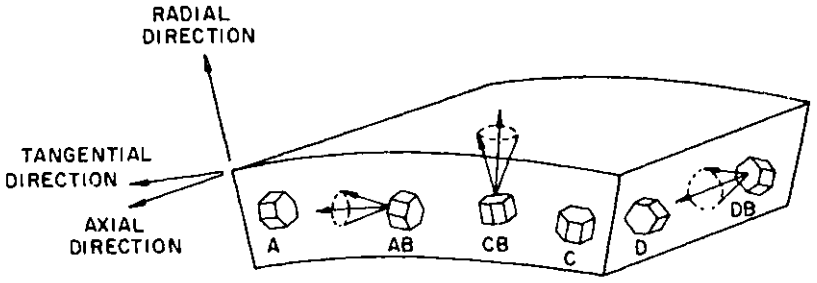

Fig. 1a. The idealised orientations.

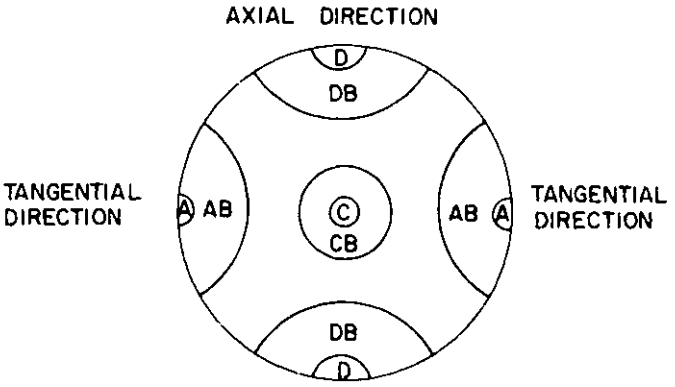

Fig. 1b. The idealised orientations on an (0001) pole figure.

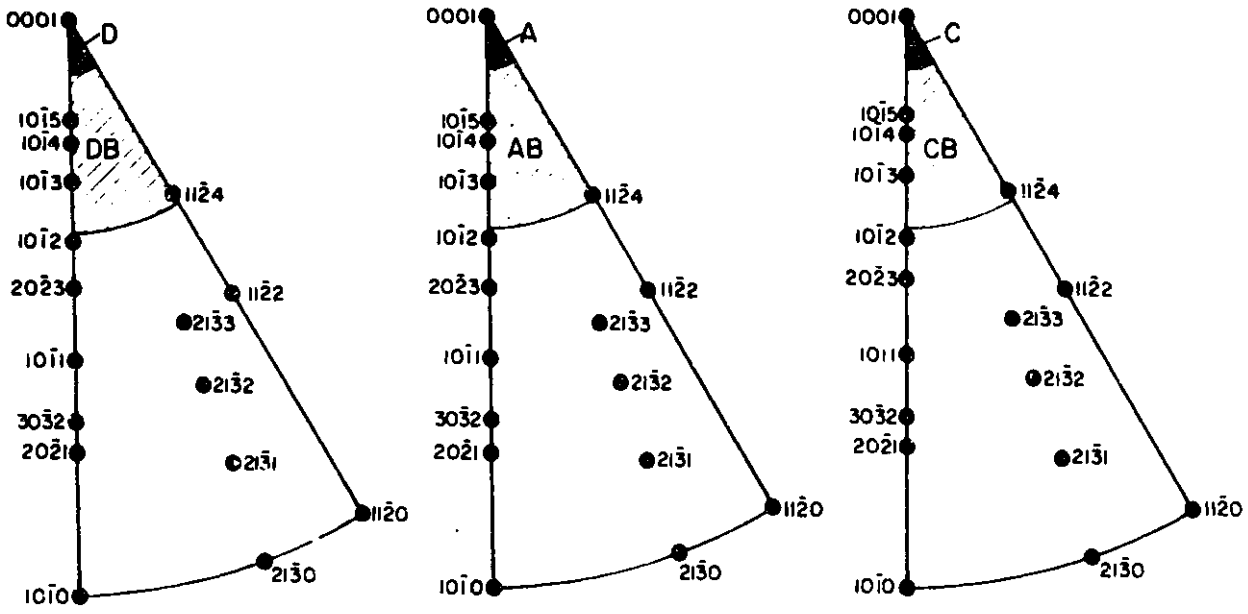

DEFINITION OF IDEALIZED ORIENTATIONS ON DIRECT AND INVERSE POLE FIGURES

F I G U R E 6

ORIENTATION OF A CRYSTAL IN RELATION

TO THE PRINCIPAL DIRECTIONS OF A TUBE

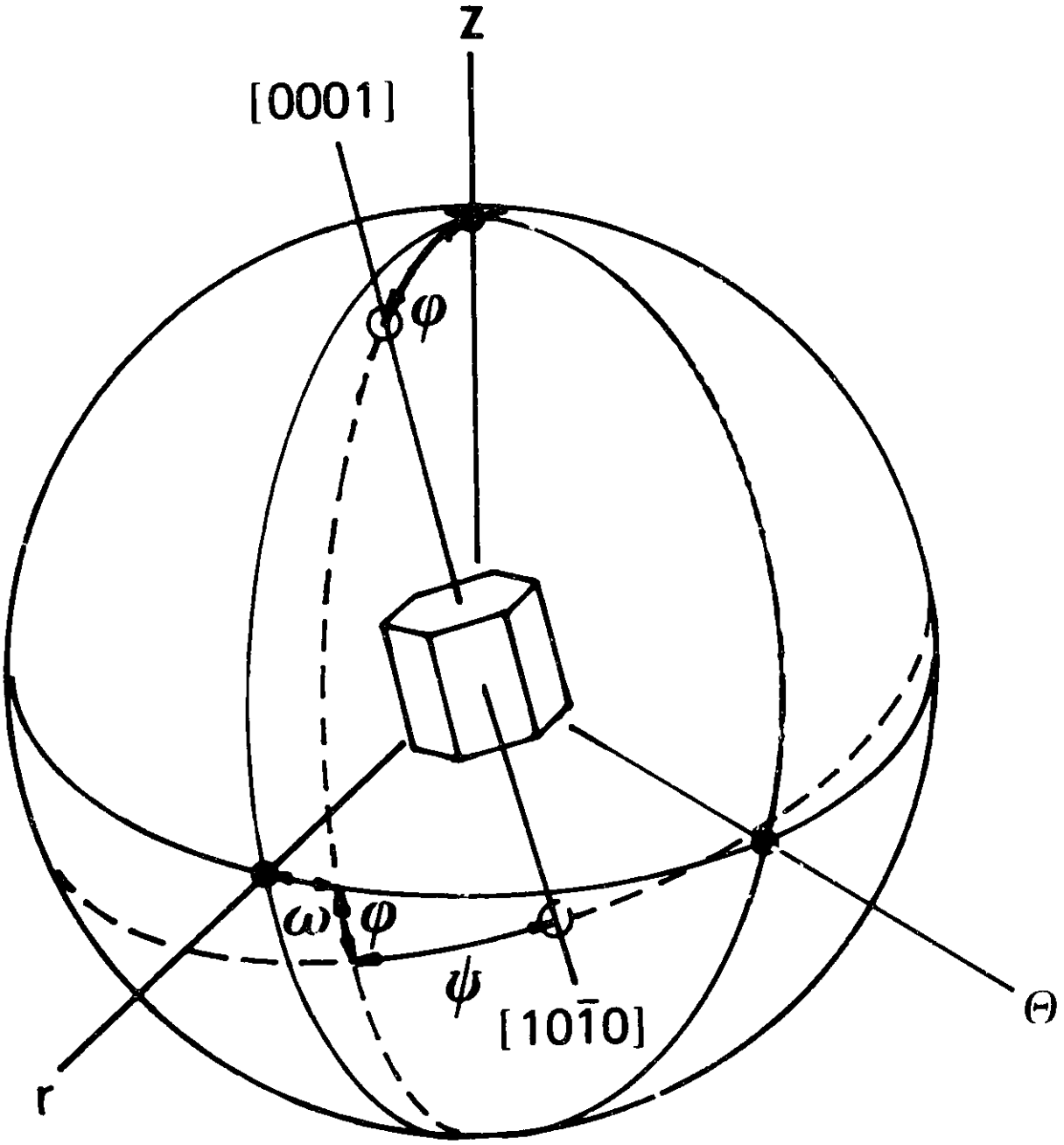

FIGURE 7

REFLECTION GEOMETRY FOR POLE FIGURE DETERMINATION

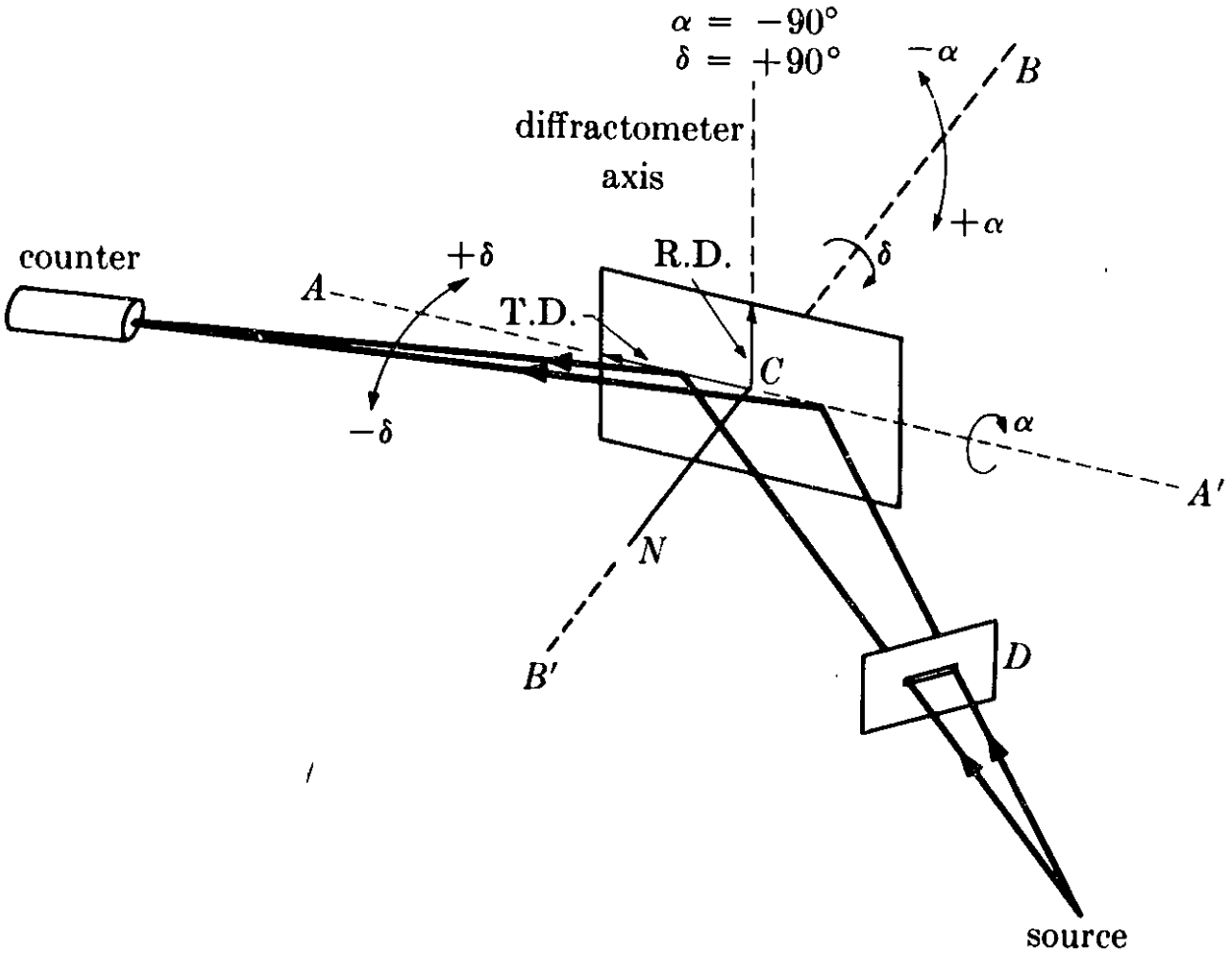

FIGURE 8

TRANSMISSION GEOMETRY FOR POLE FIGURE DETERMINATION

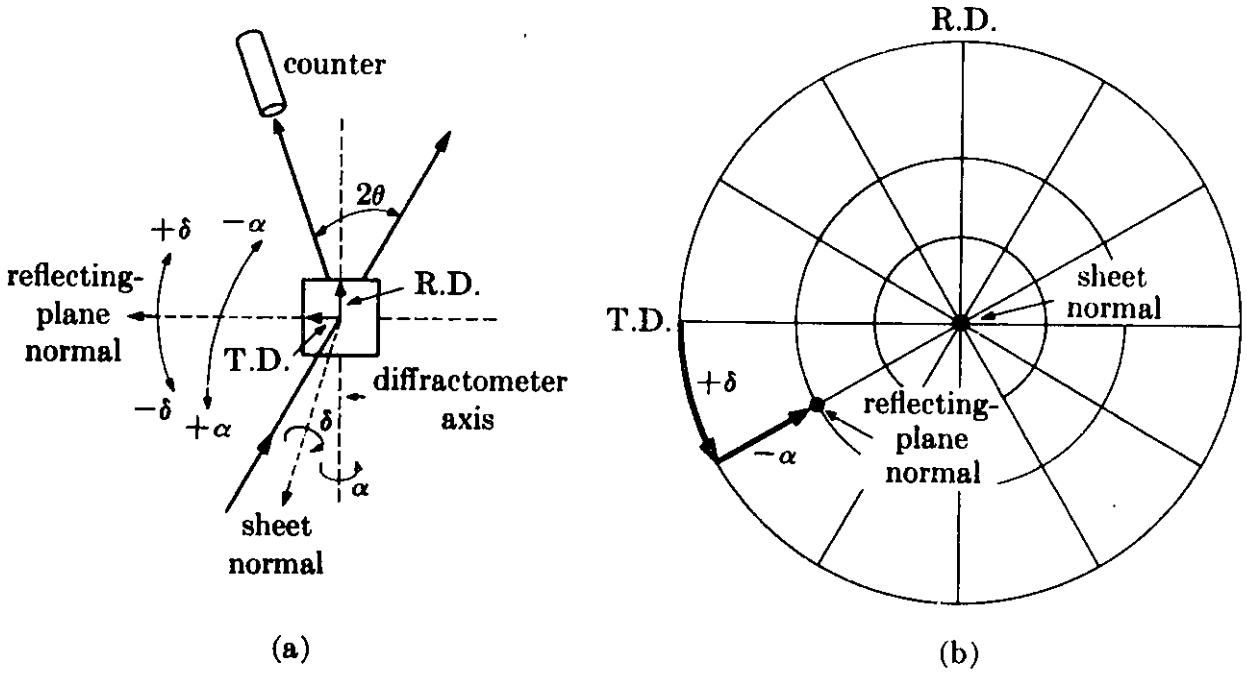

F I G U R E 9

POLAR STEREOGRAPHIC PROJECTION SHOWING IMPORTANT ANGLES

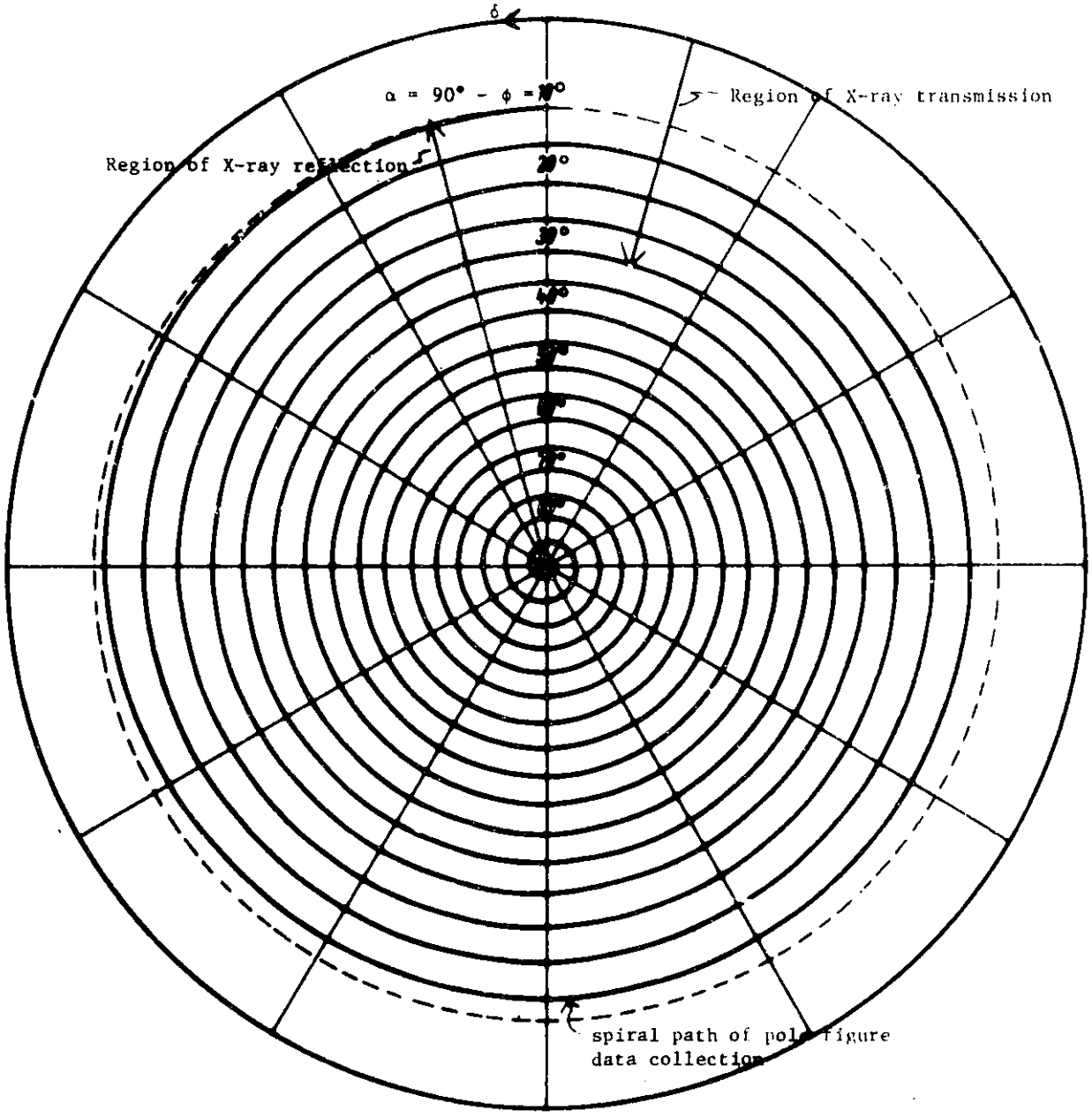

F I G U R E 10

FABRICATION PROCESSES FOR ZIRCONIUM ALLOYS

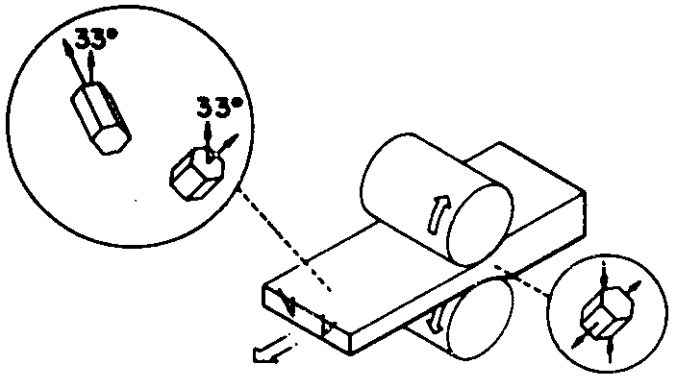

(a) SHEET ROLLING

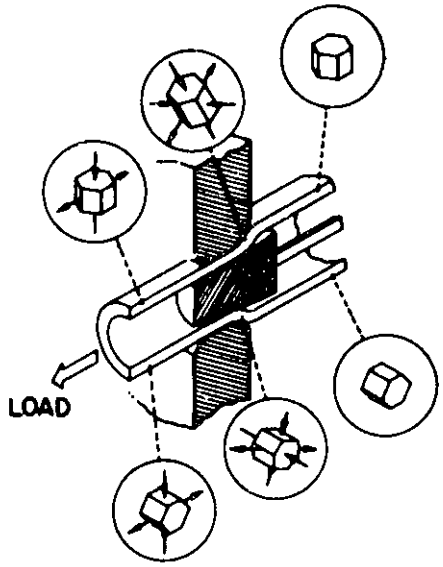

(b) PLUG DRAWING WITH WALL THINNING

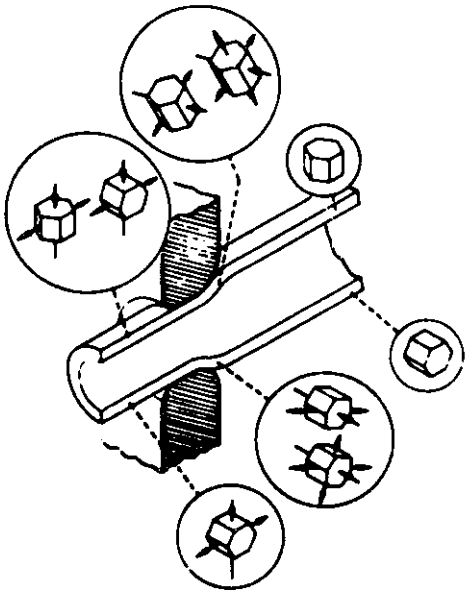

(c) TUBE SINKING WITH AND WITHOUT WALL THICKENING

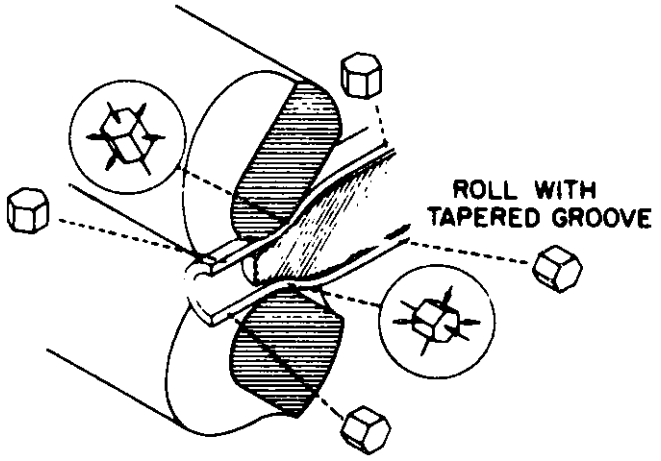

(d) TUBE REDUCING

FIGURE 11

STRAIN PATH DIAGRAM

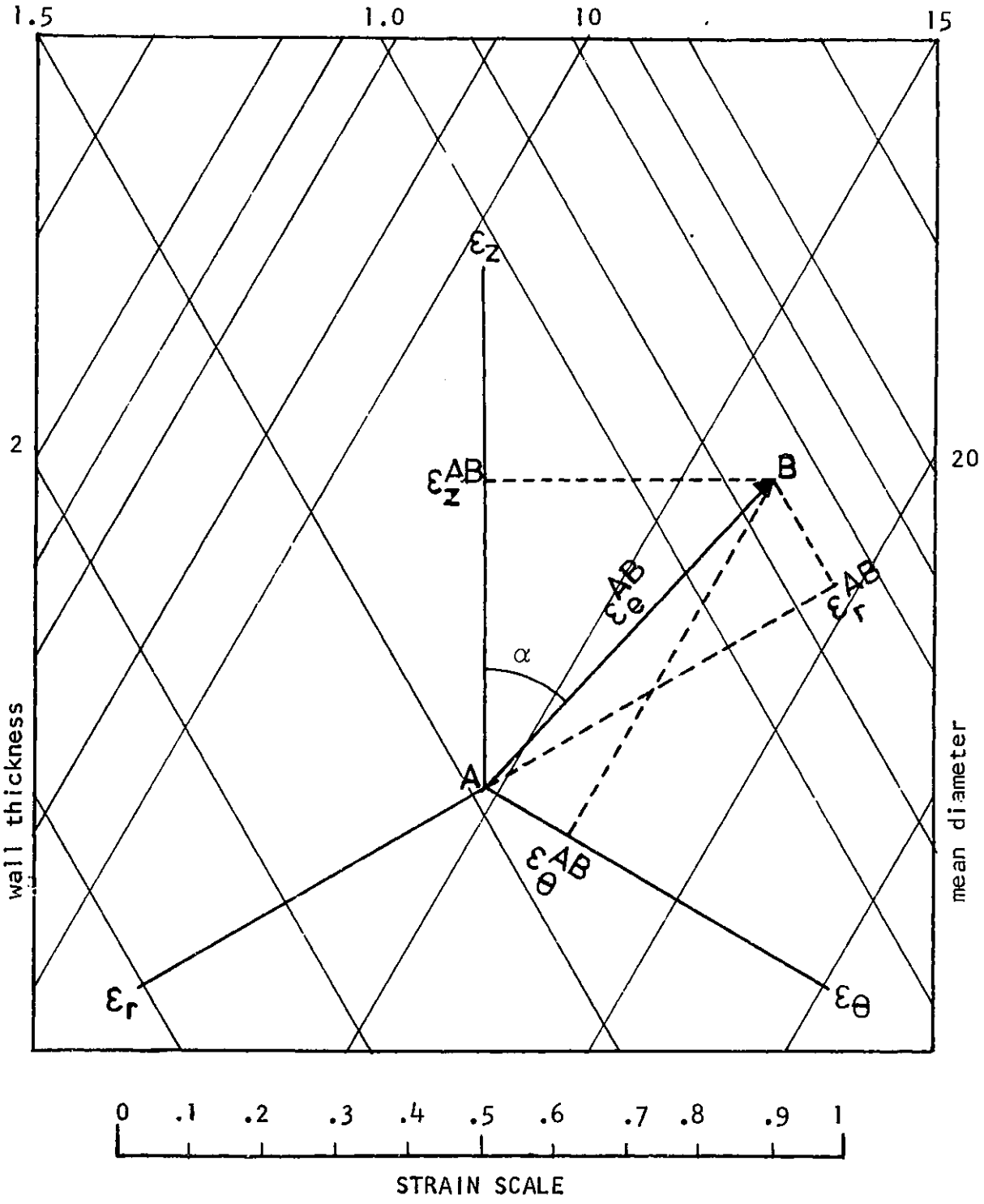

F I G U R E 12

BASAL POLE TEXTURES DIAGRAM

EQUILATERAL TRIANGLE OUTLINED BY EXTREME TEXTURES

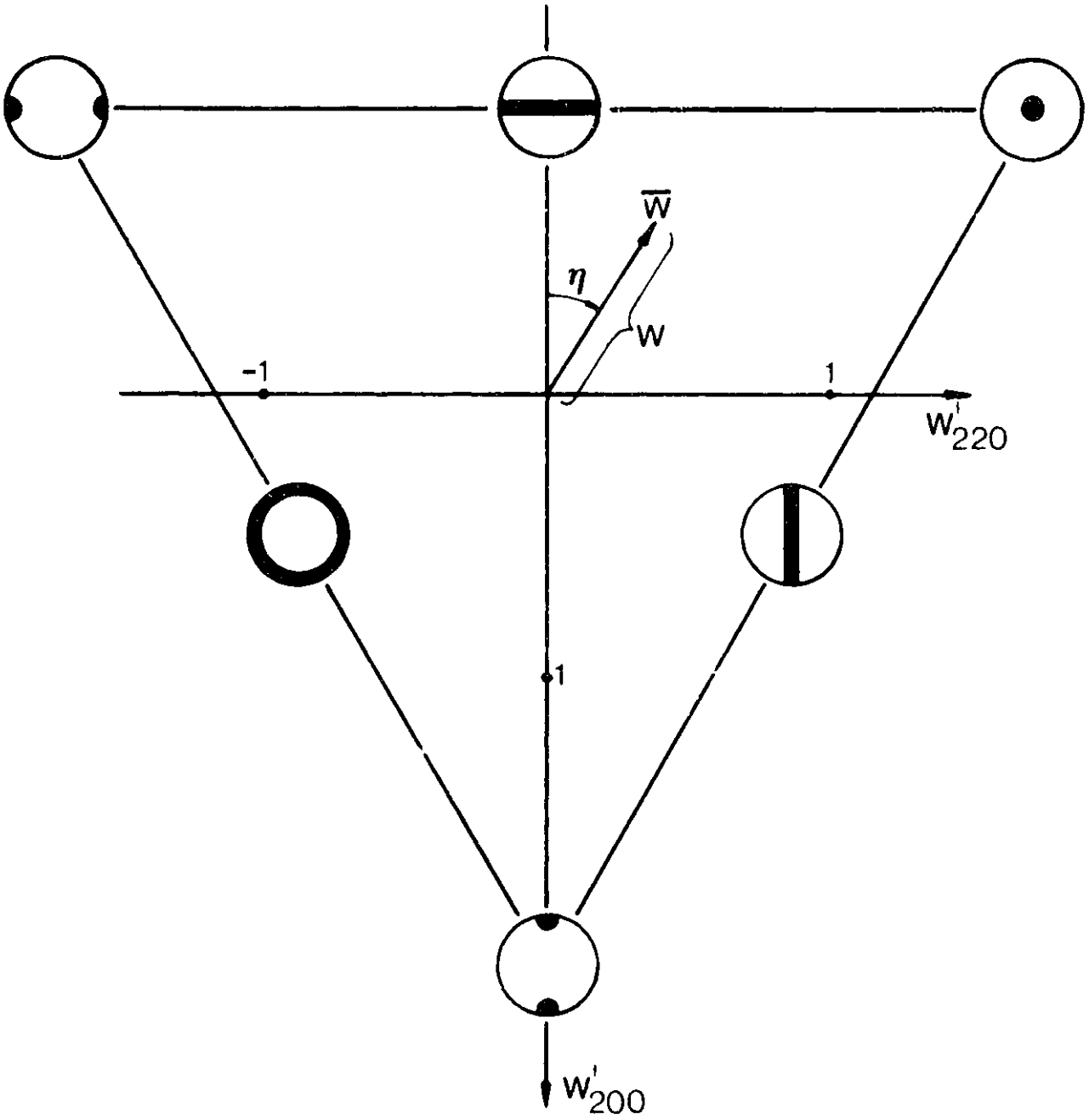

F I G U R E 13

TEXTURE ROSE RELATING STRAIN RATIOS TO RESULTING STABLE TEXTURES

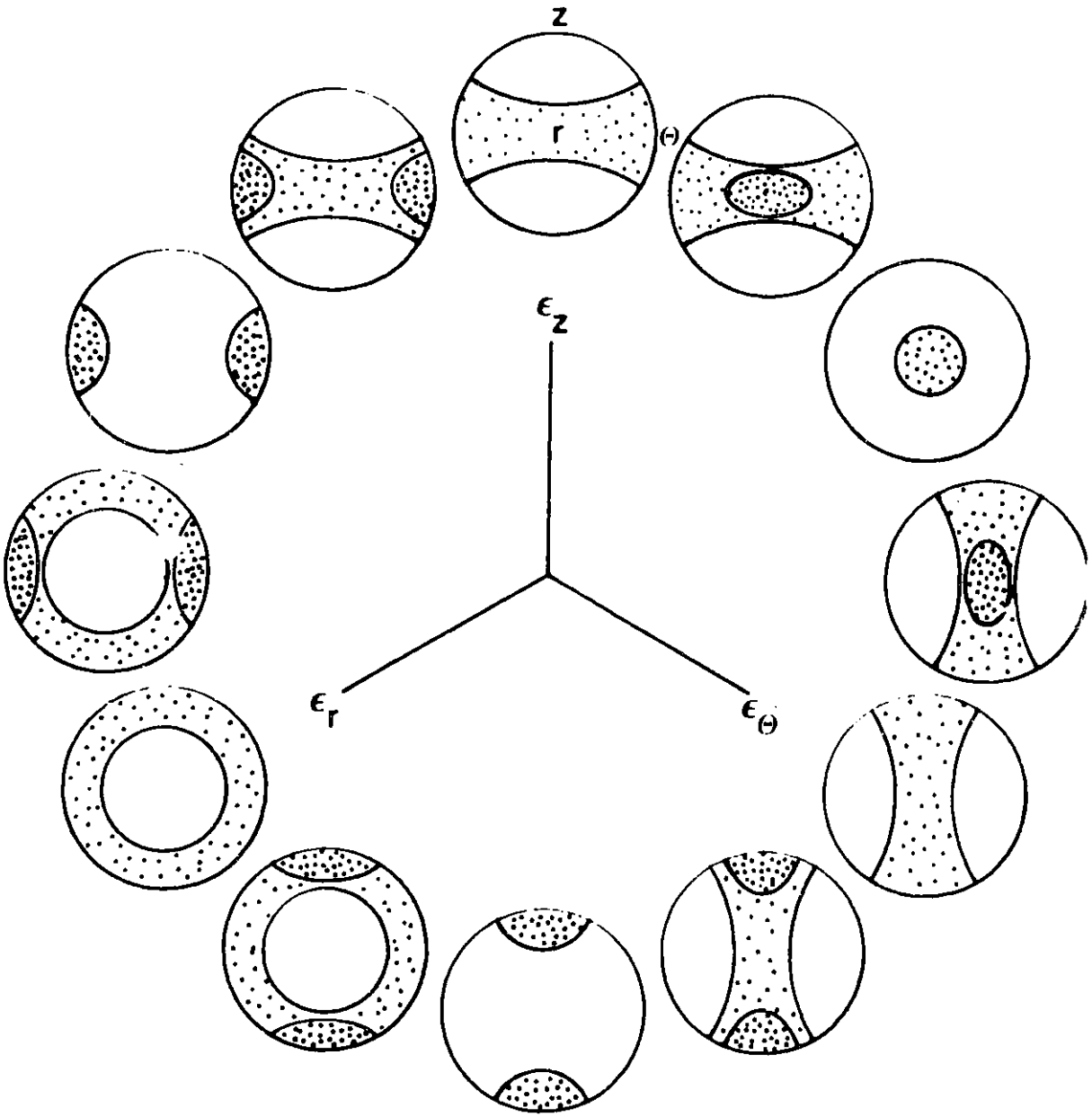

F I G U R E 14

THREE-ROLL TUBE REDUCER (HPTR MACHINE)

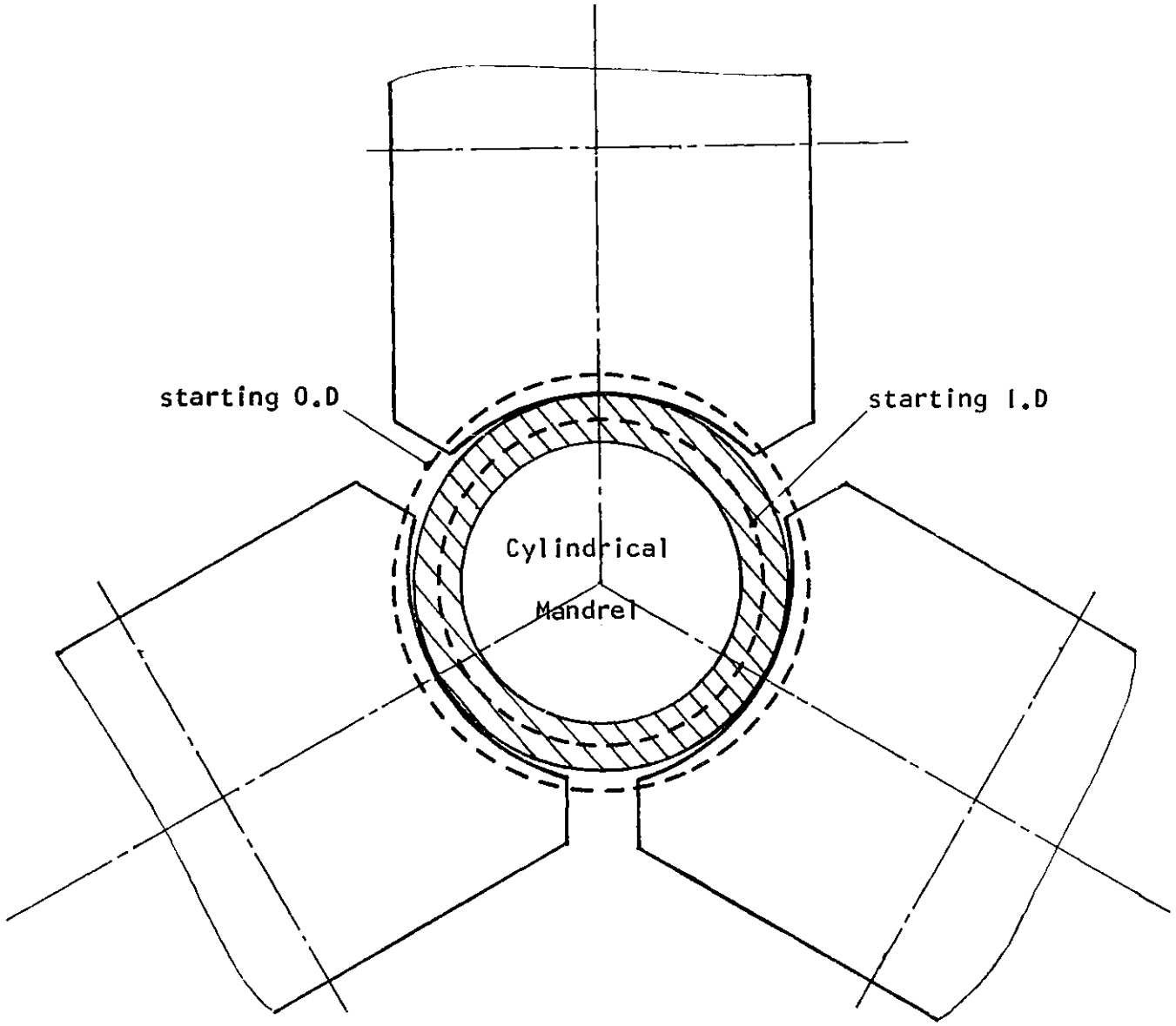

F I G U R E 15

TWO-ROLL TUBE REDUCER (25 VMR MACHINE)

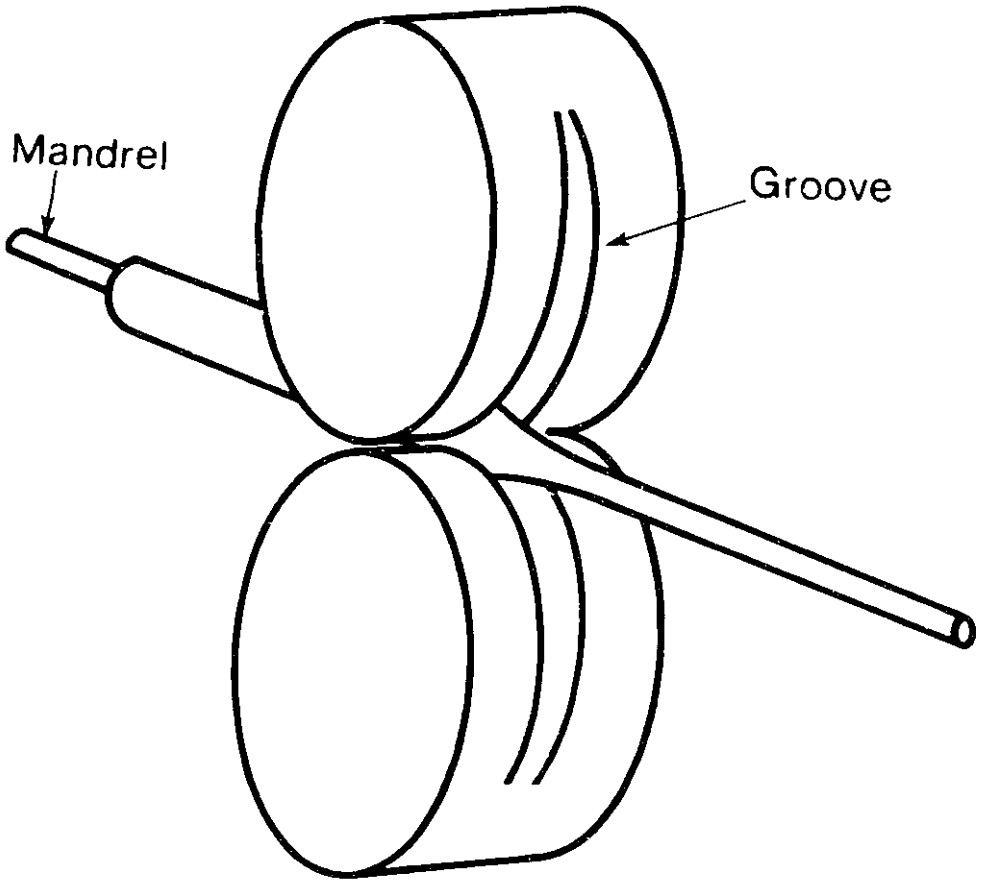

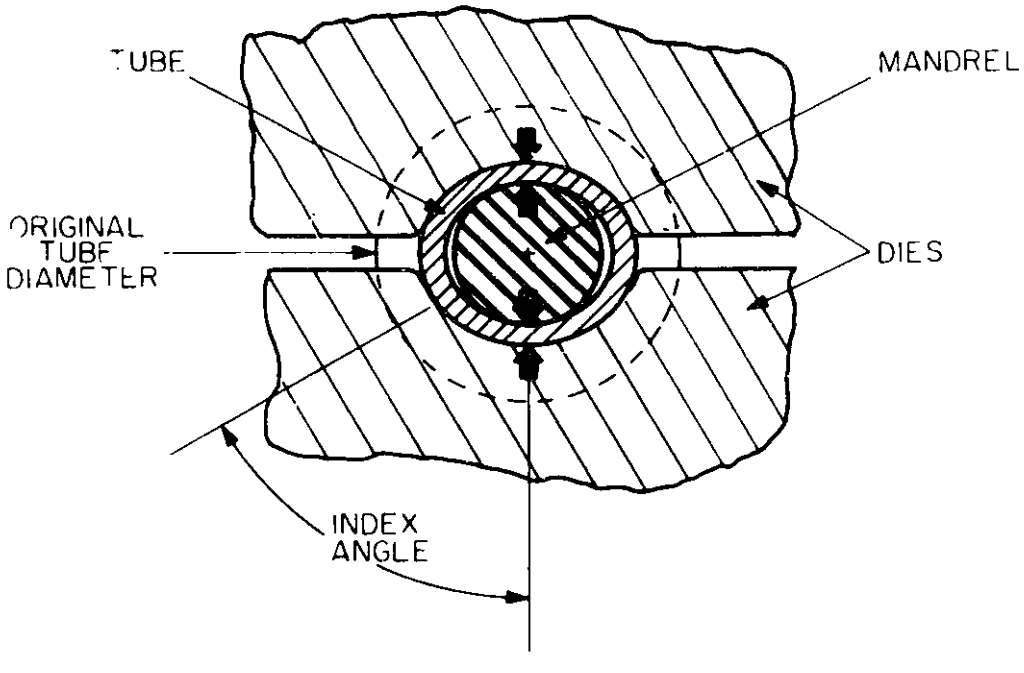

FIGURE 16

PROFILE AND SAMPLING LOCATIONS FOR REDUCTION CONE FROM HPTR MACHINE

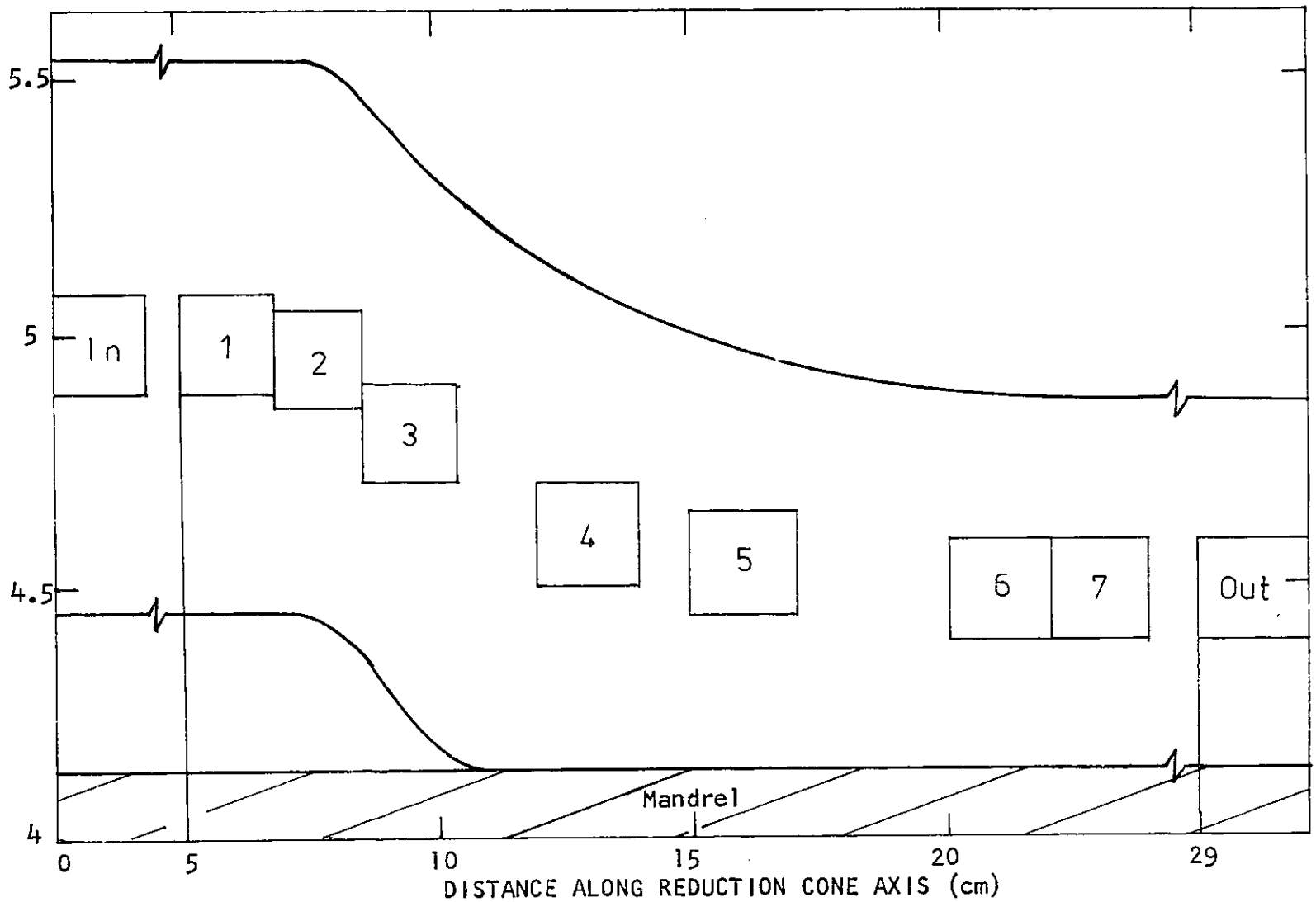

F I G U R E 17

PROFILE AND SAMPLING LOCATIONS FOR REDUCTION CONE FROM 25 VMR MACHINE

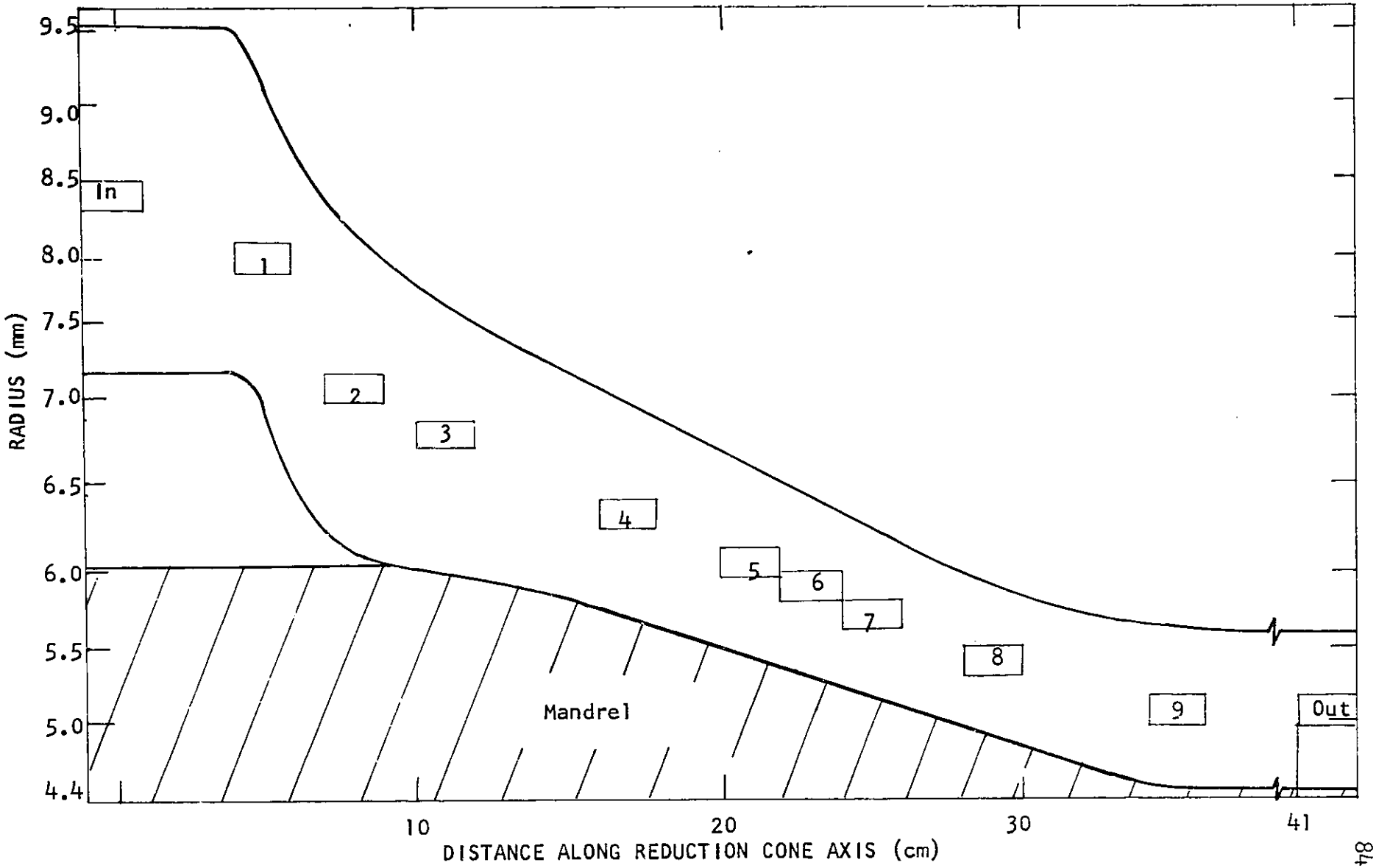

FIGURE 18
STRAIN PATHS

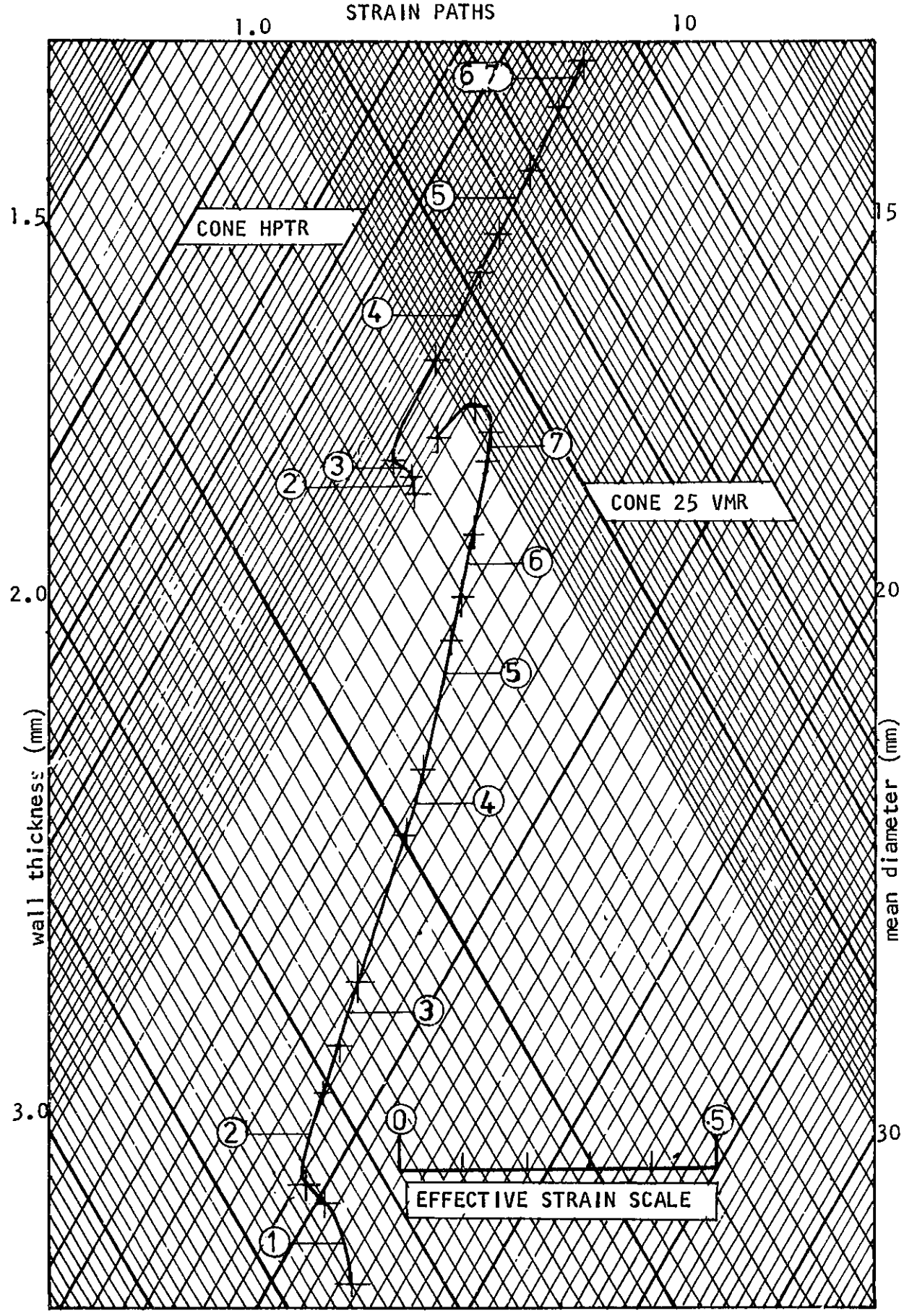

F I G U R E 19

REDUCTION IN AREA ALONG CONE AXIS

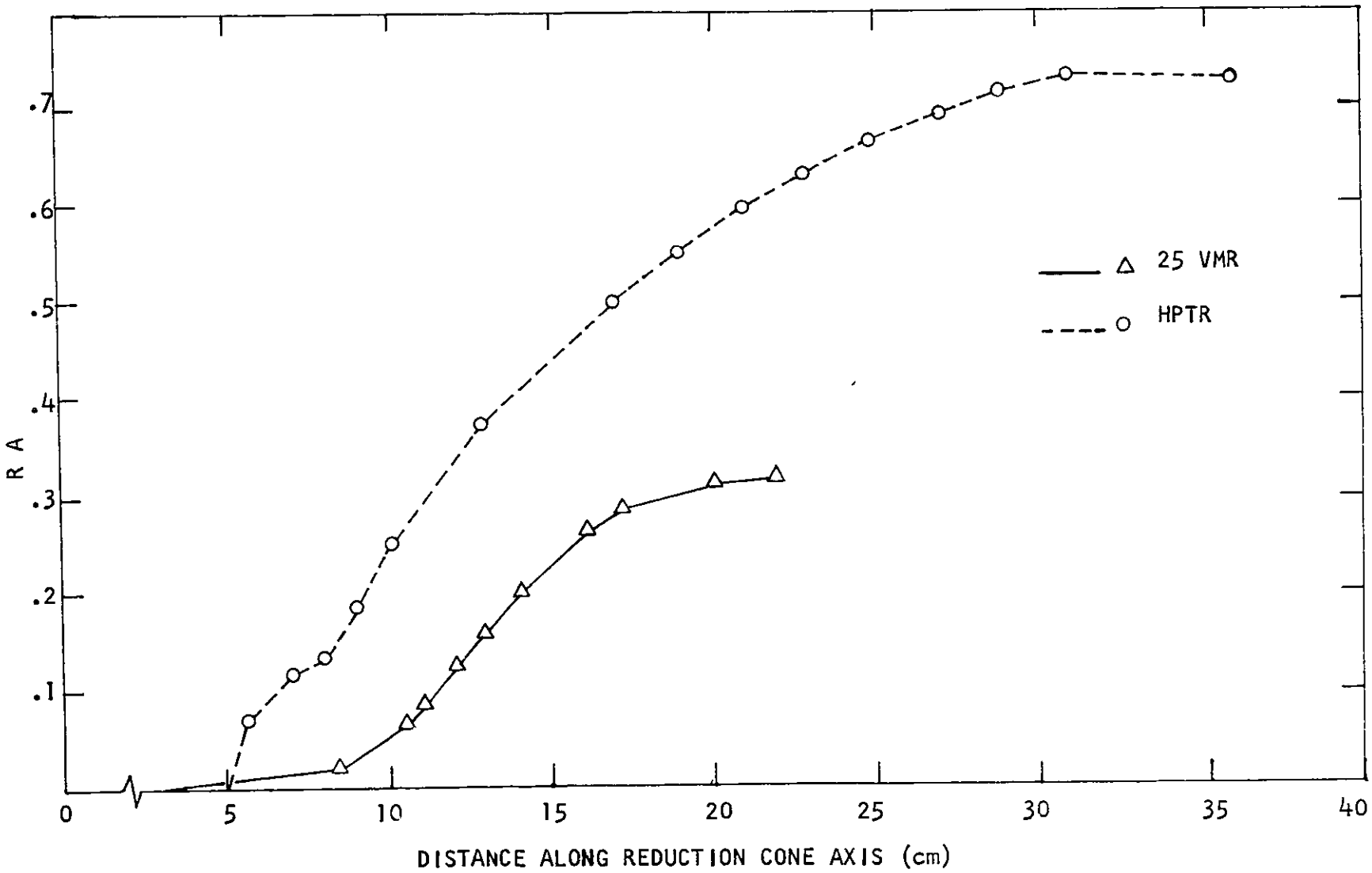

F I G U R E 20

BASAL POLE FIGURE FOR SAMPLE HPTR IN

A.D

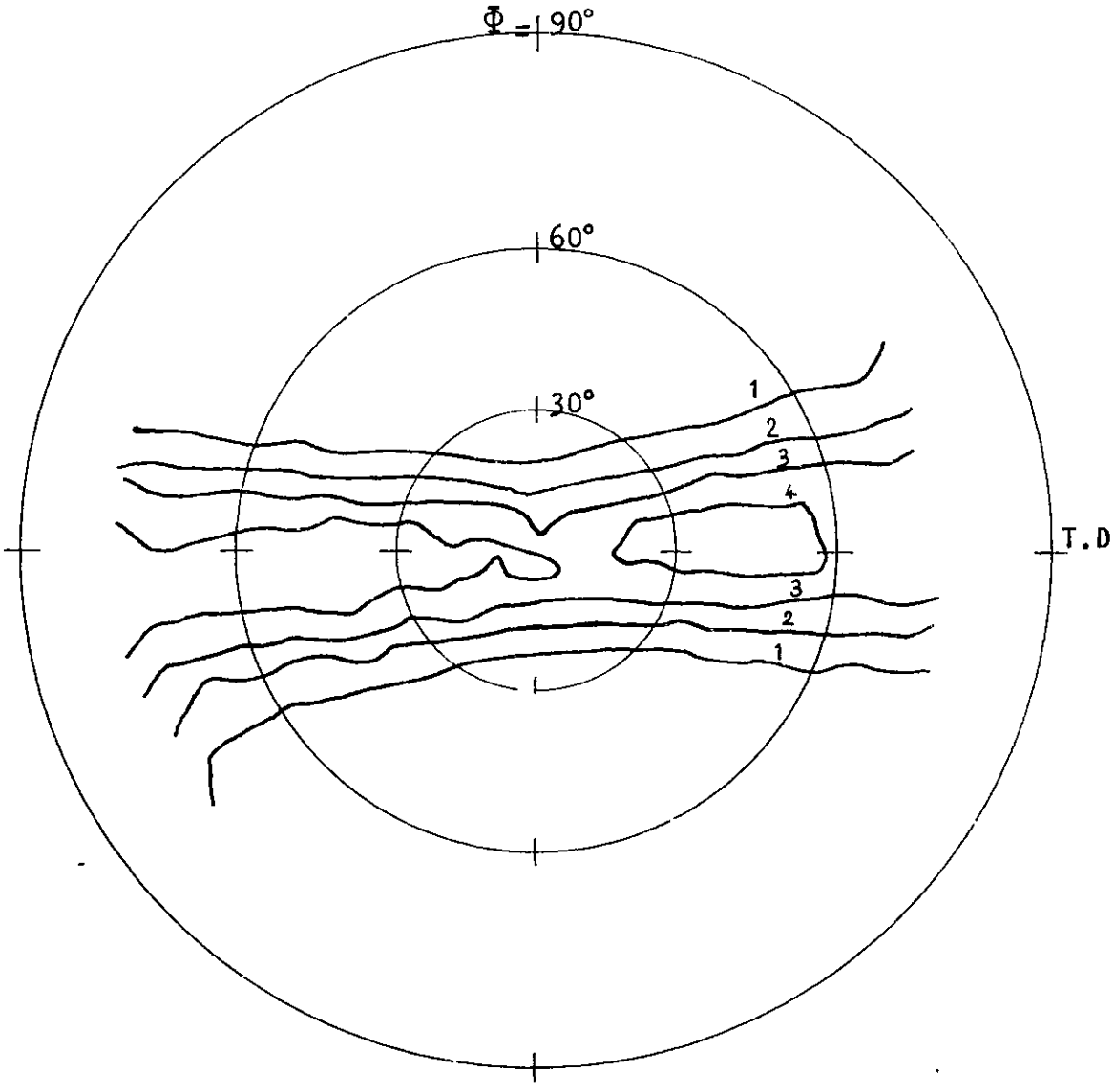

F I G U R E 21

BASAL POLE FIGURE FOR SAMPLE HPTR 3

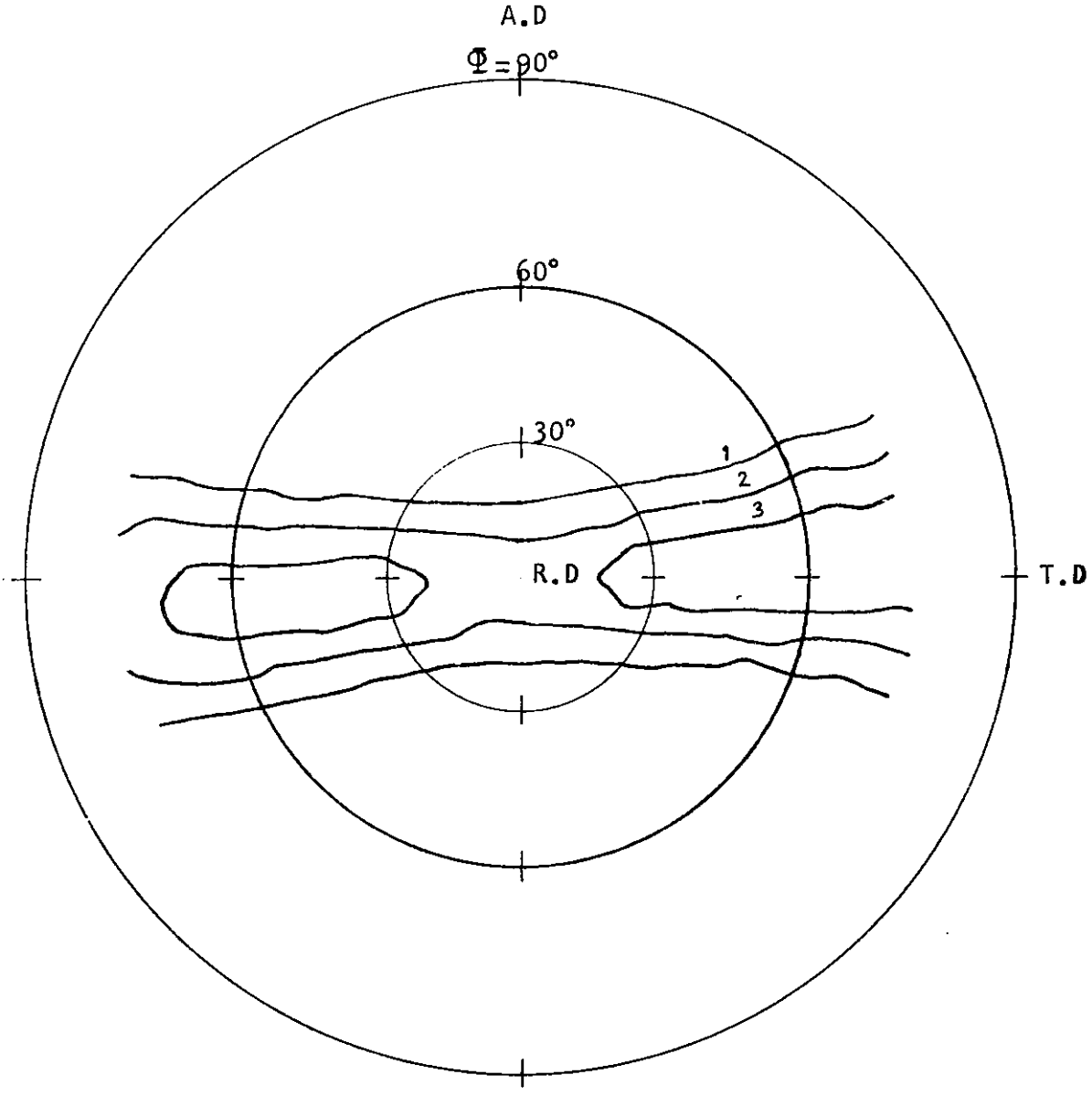

F I G U R E 22

BASAL POLE FIGURE FOR SAMPLE HPTR 4

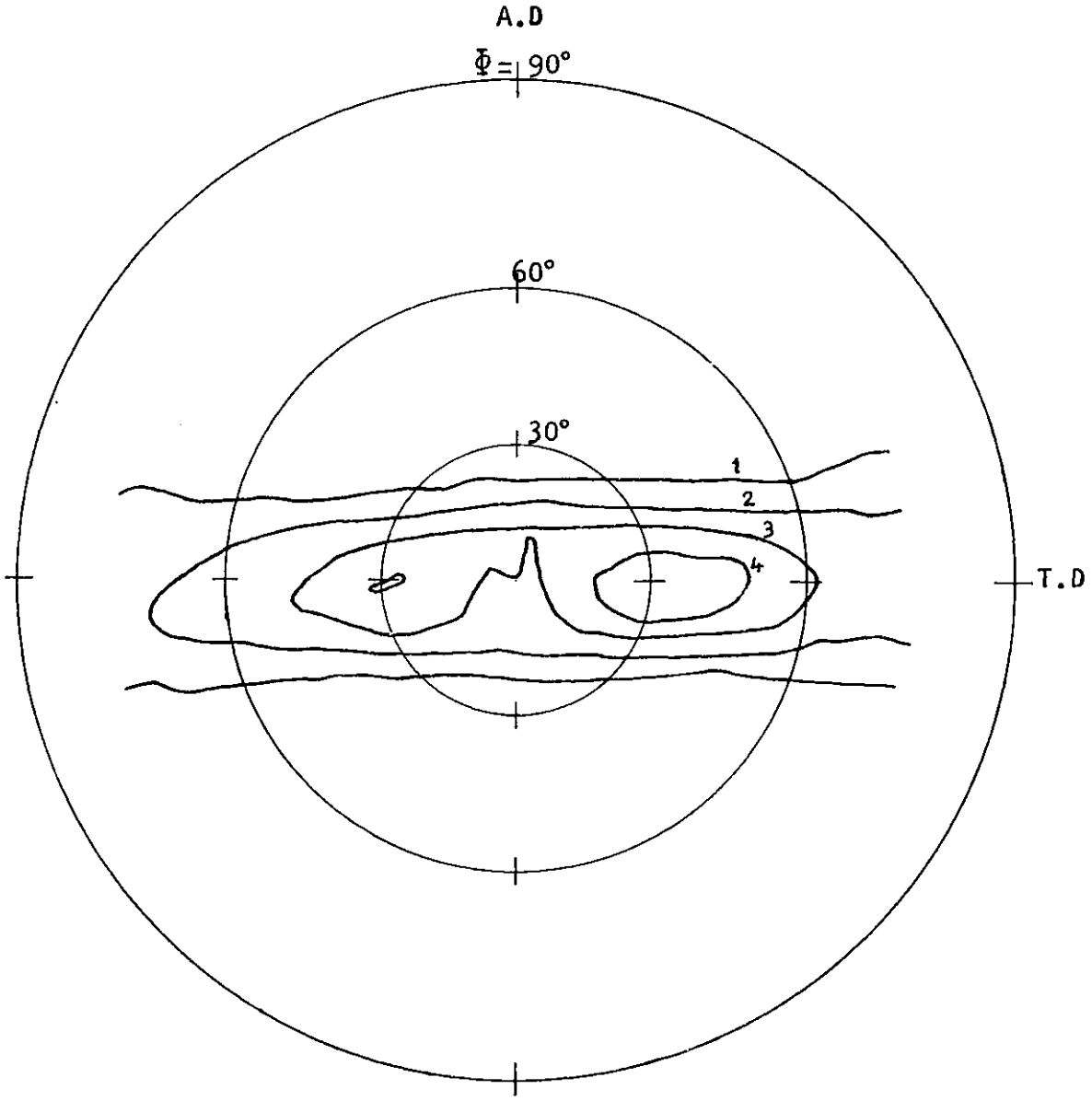

F I G U R E 23

BASAL POLE FIGURE FOR SAMPLE HPTR 7

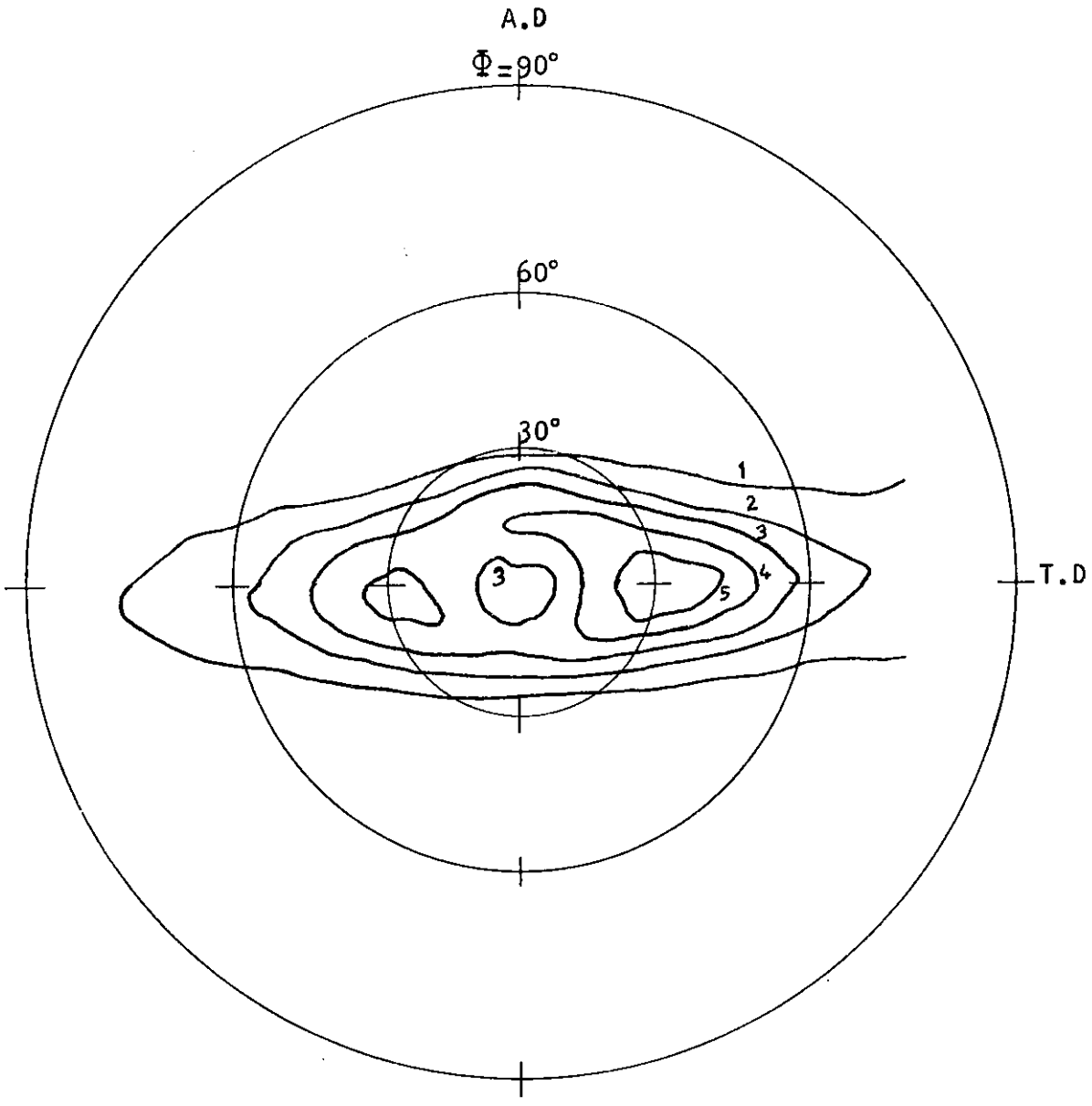

F I G U R E 24

BASAL POLE FIGURE FOR SAMPLE 25 VMR IN

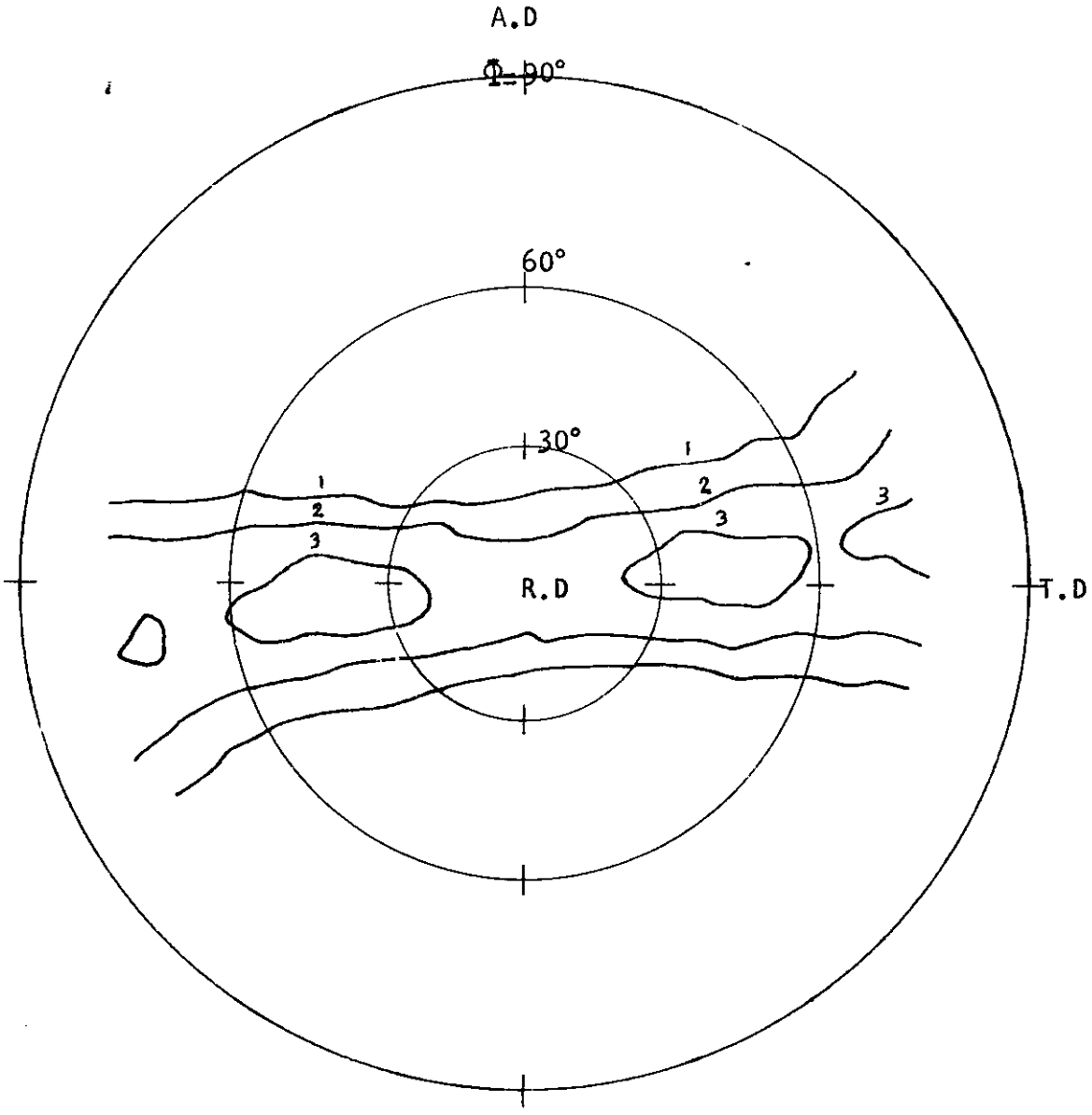

F I G U R E 25

BASAL POLE FIGURE FOR SAMPLE 25 VMR 1

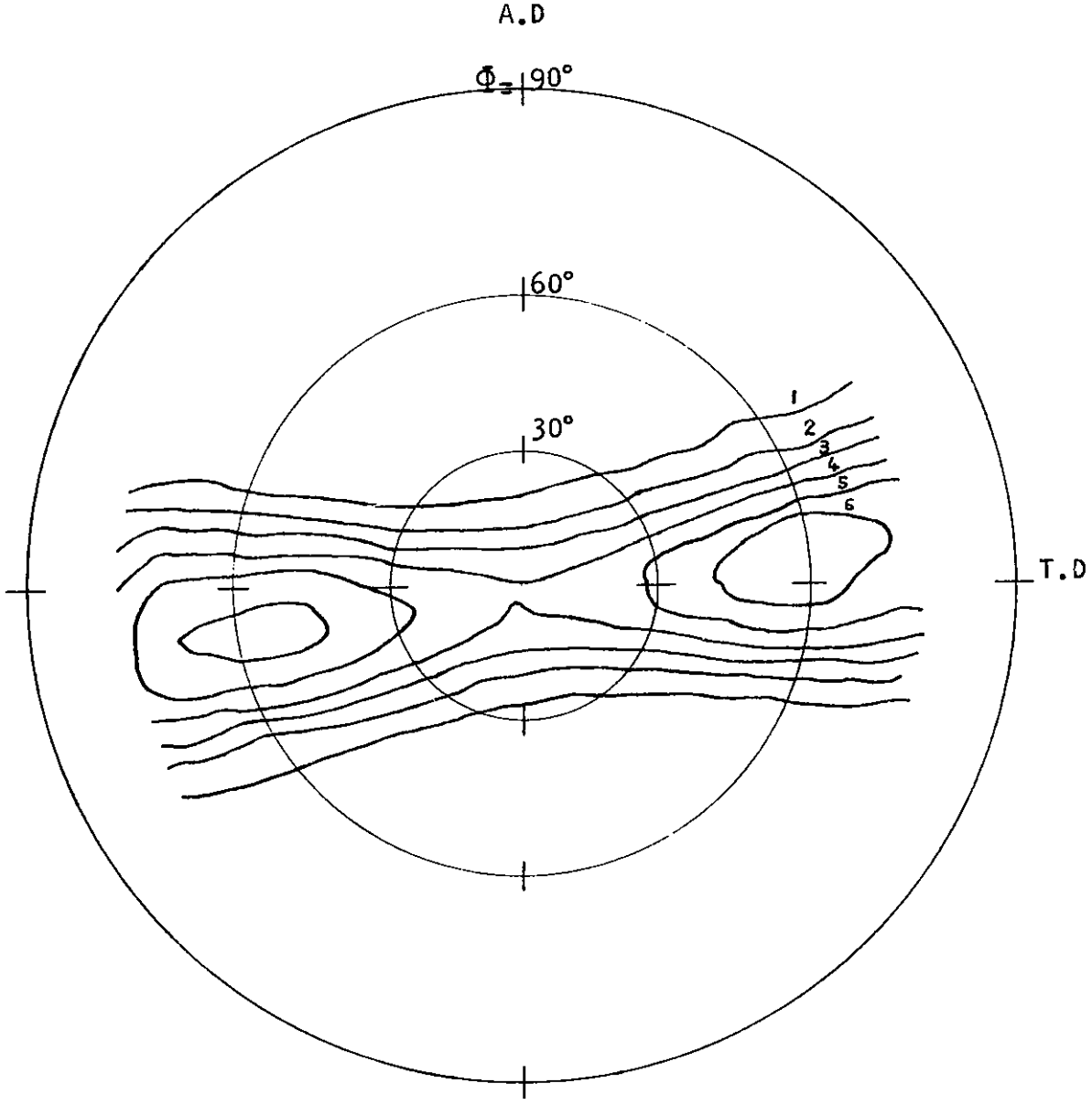

F I G U R E 26

BASAL POLE FIGURE FOR SAMPLE 25 VMR 3

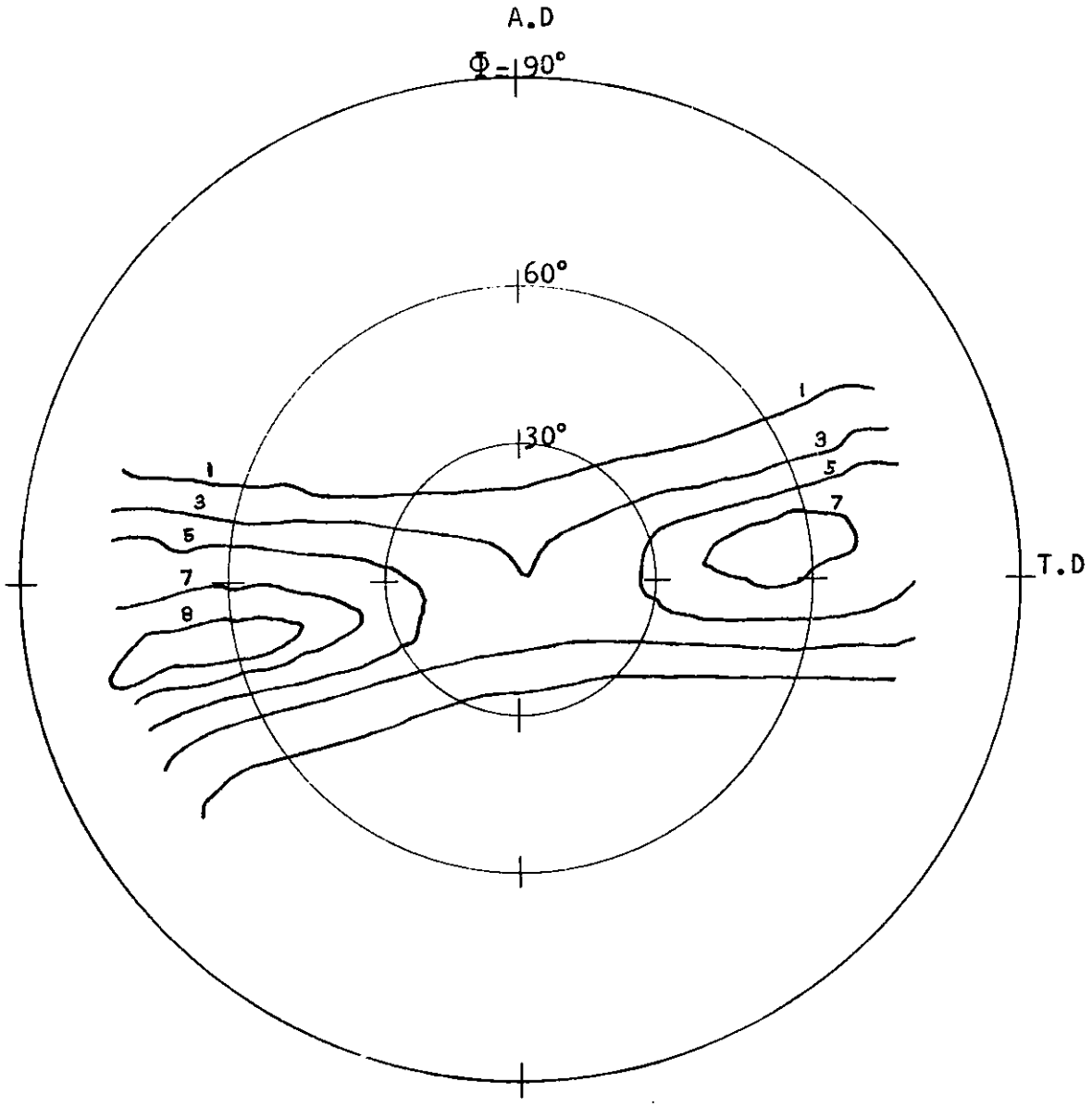

F I G U R E 27

BASAL POLE FIGURE FOR SAMPLE 25 VMR 6

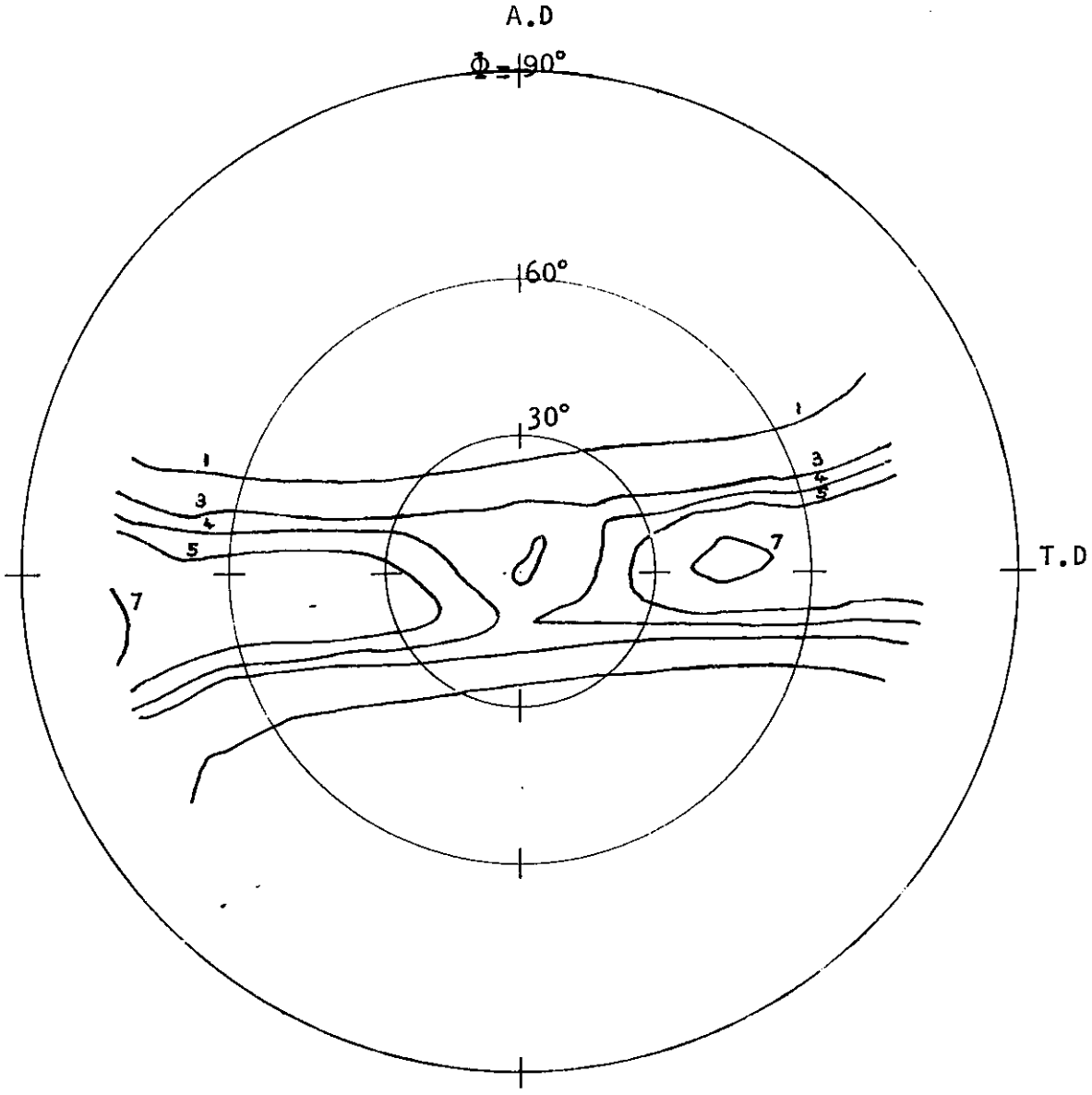

F I G U R E 28

BASAL POLE FIGURE FOR SAMPLE 25 VMR 8

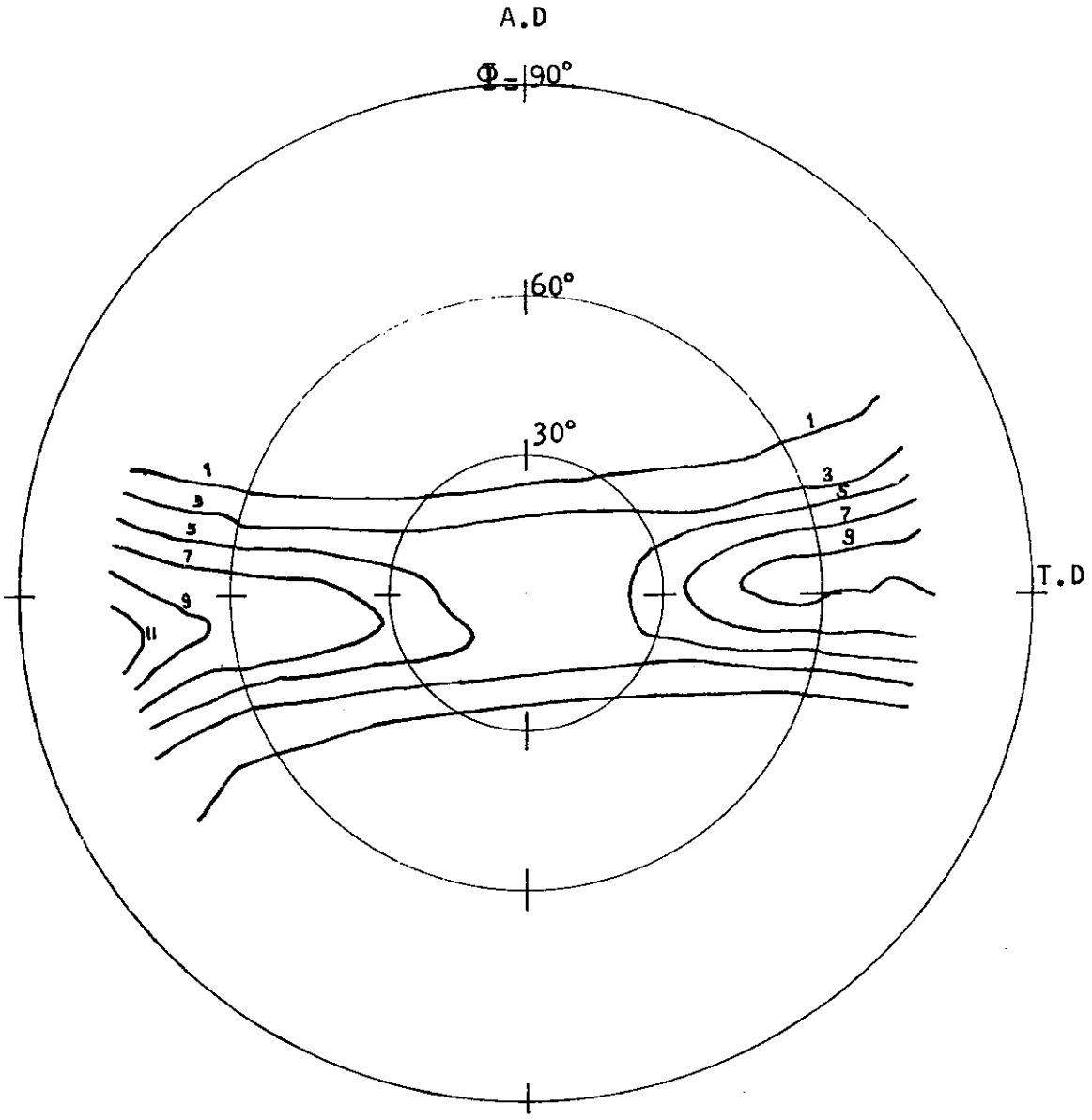

F I G U R E 29

TEXTURE PARAMETER f VERSUS DEFORMATION PARAMETER α

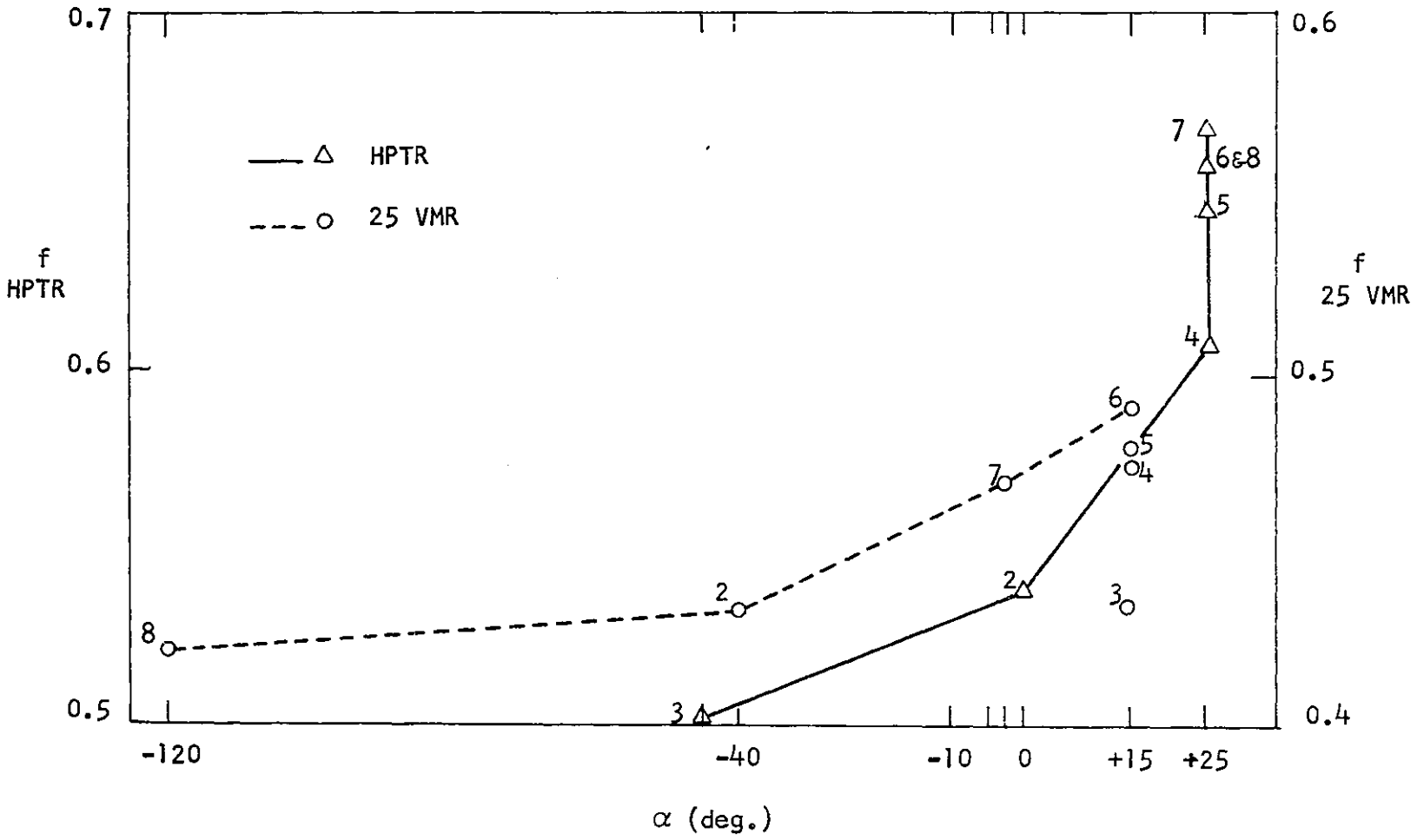

F I G U R E 30

TEXTURE PARAMETER f VERSUS DEFORMATION PARAMETER ε_e

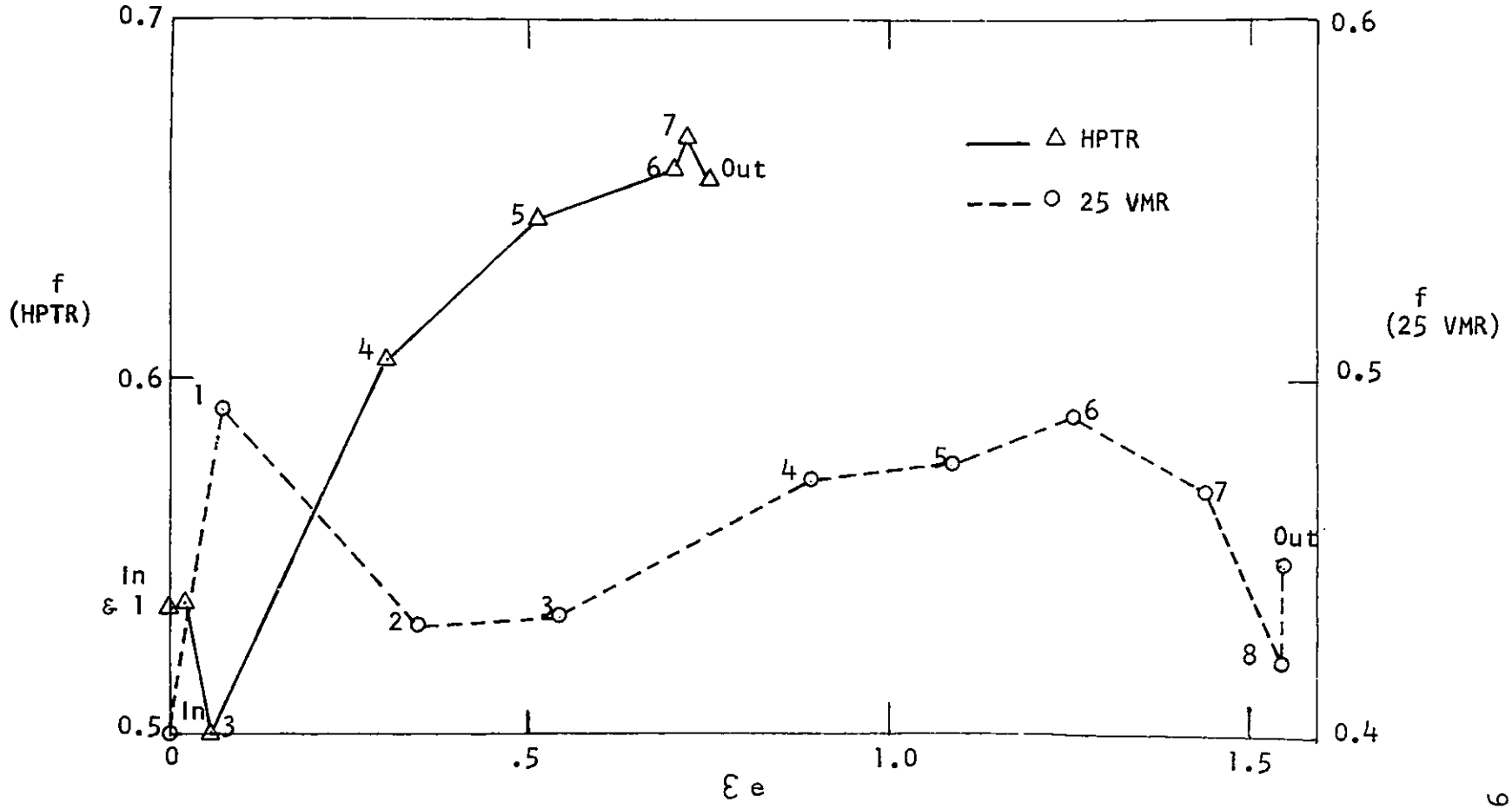

FIGURE 31

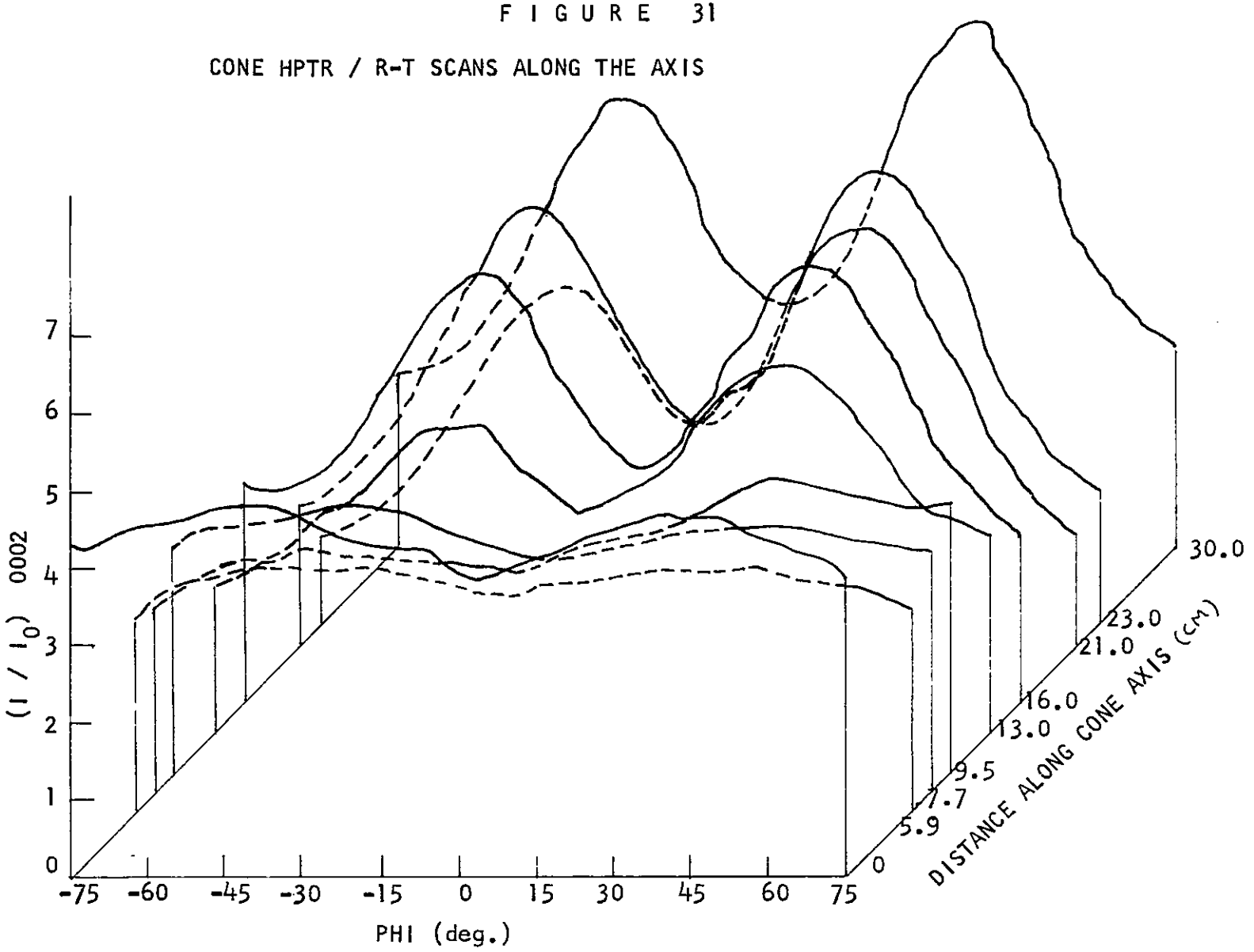
CONE HPTR / R-T SCANS ALONG THE AXIS
(I / I0) 0002
0
1
2
3
4
5
6
7
-75
-60
-45
-30
-15
0
15
30
45
60
75
PHI (deg.)
0
5.9
7.7
9.5
13.0
16.0
21.0
23.0
30.0
DISTANCE ALONG CONE AXIS (CM)

F I G U R E 32

CONE 25 VMR / R-T SCANS ALONG THE AXIS

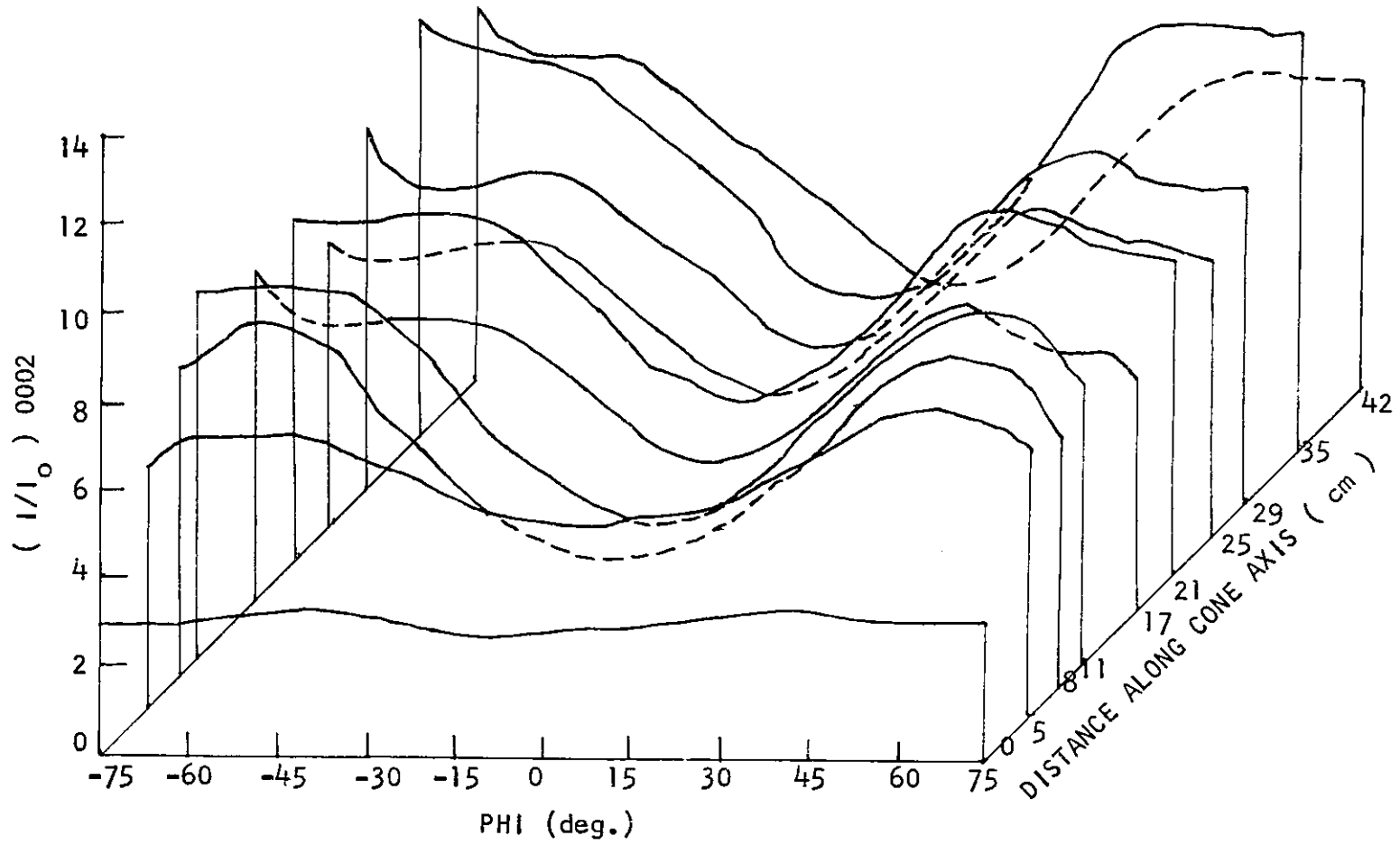

F I G U R E 33

TEXTURE PARAMETER S_1 / S_0 VERSUS DEFORMATION PARAMETER α

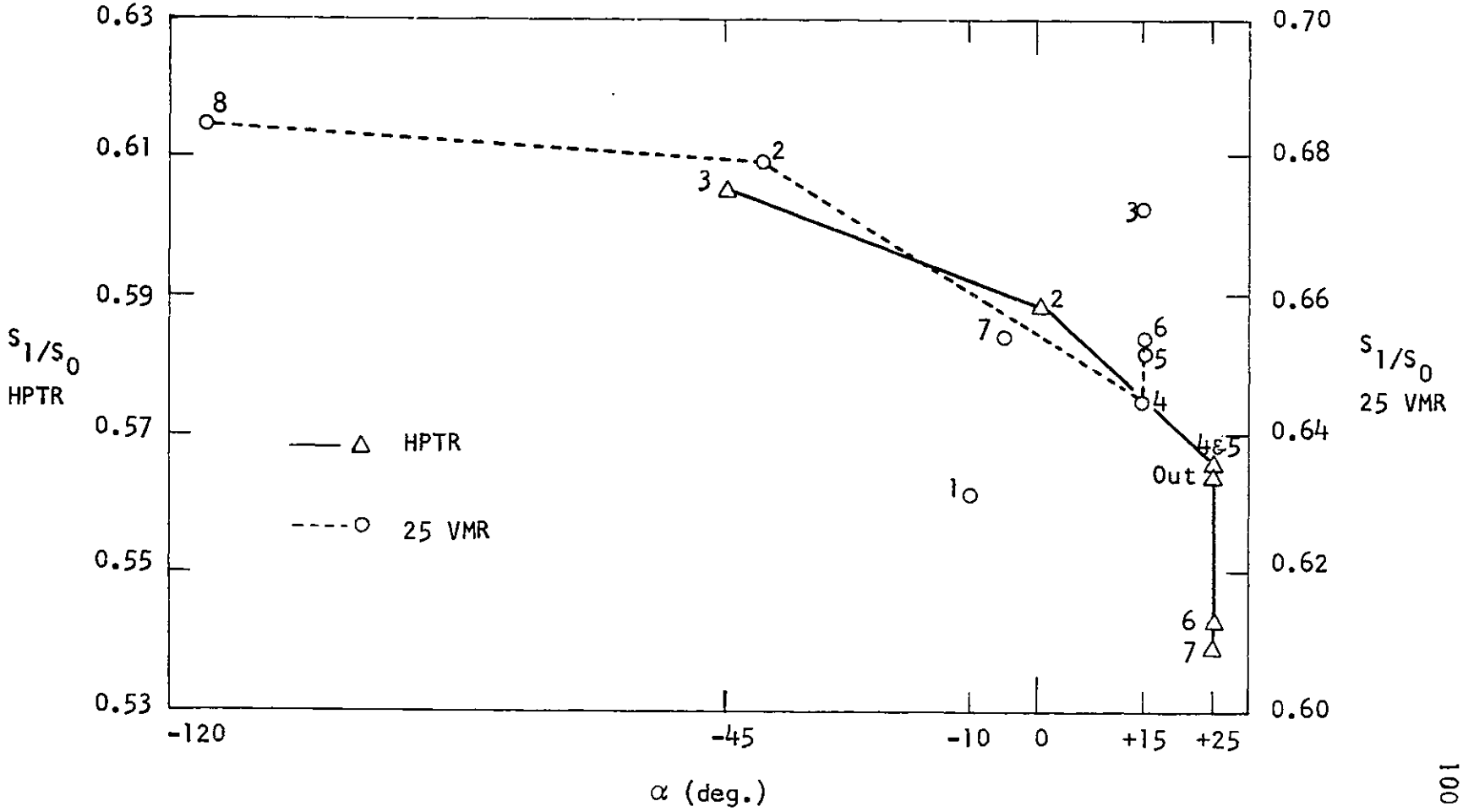

F I G U R E 34

TEXTURE PARAMETER S.D VERSUS DEFORMATION PARAMETER α

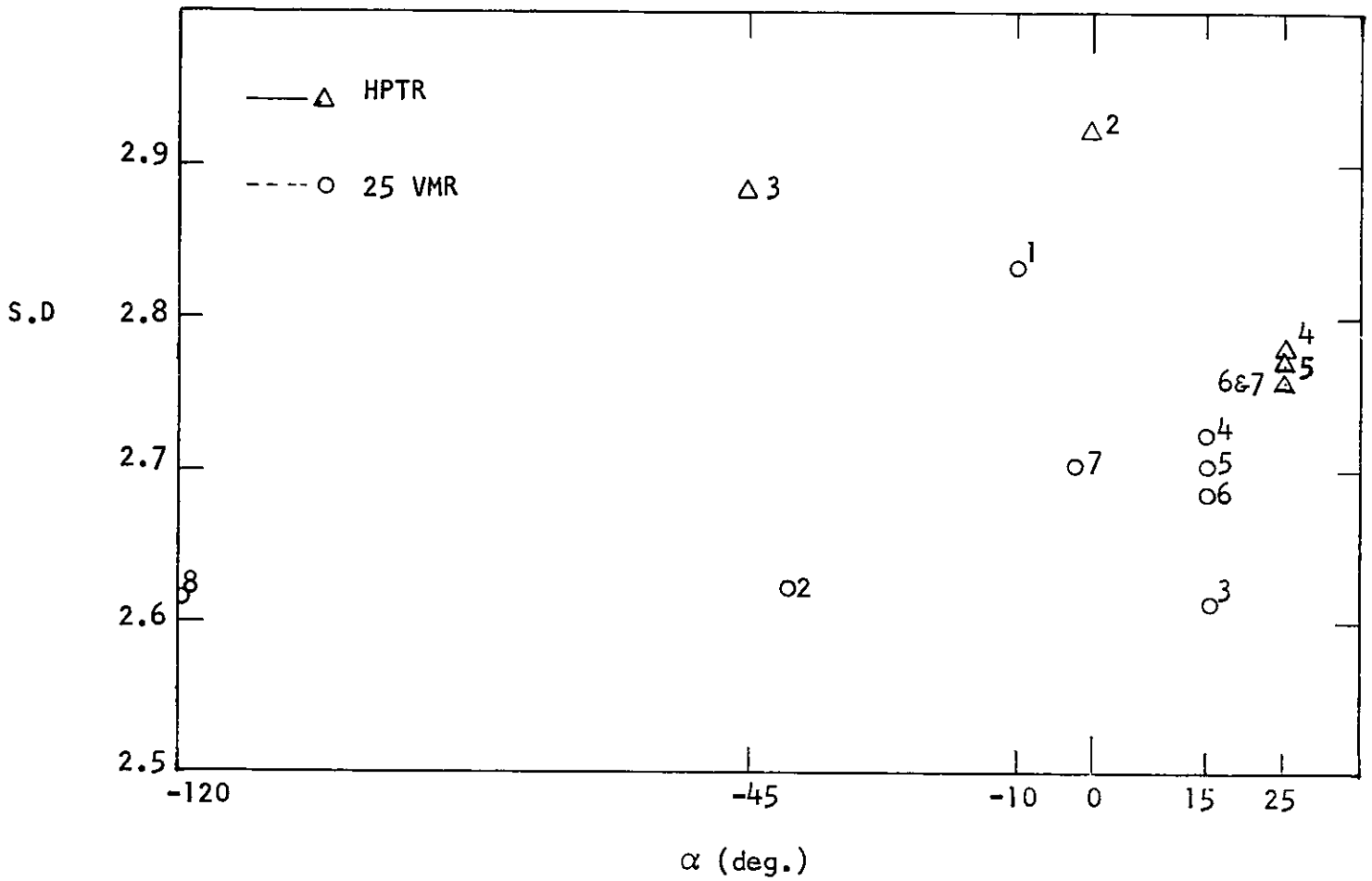

F I G U R E 35

TEXTURE PARAMETER F VERSUS DEFORMATION PARAMETER α

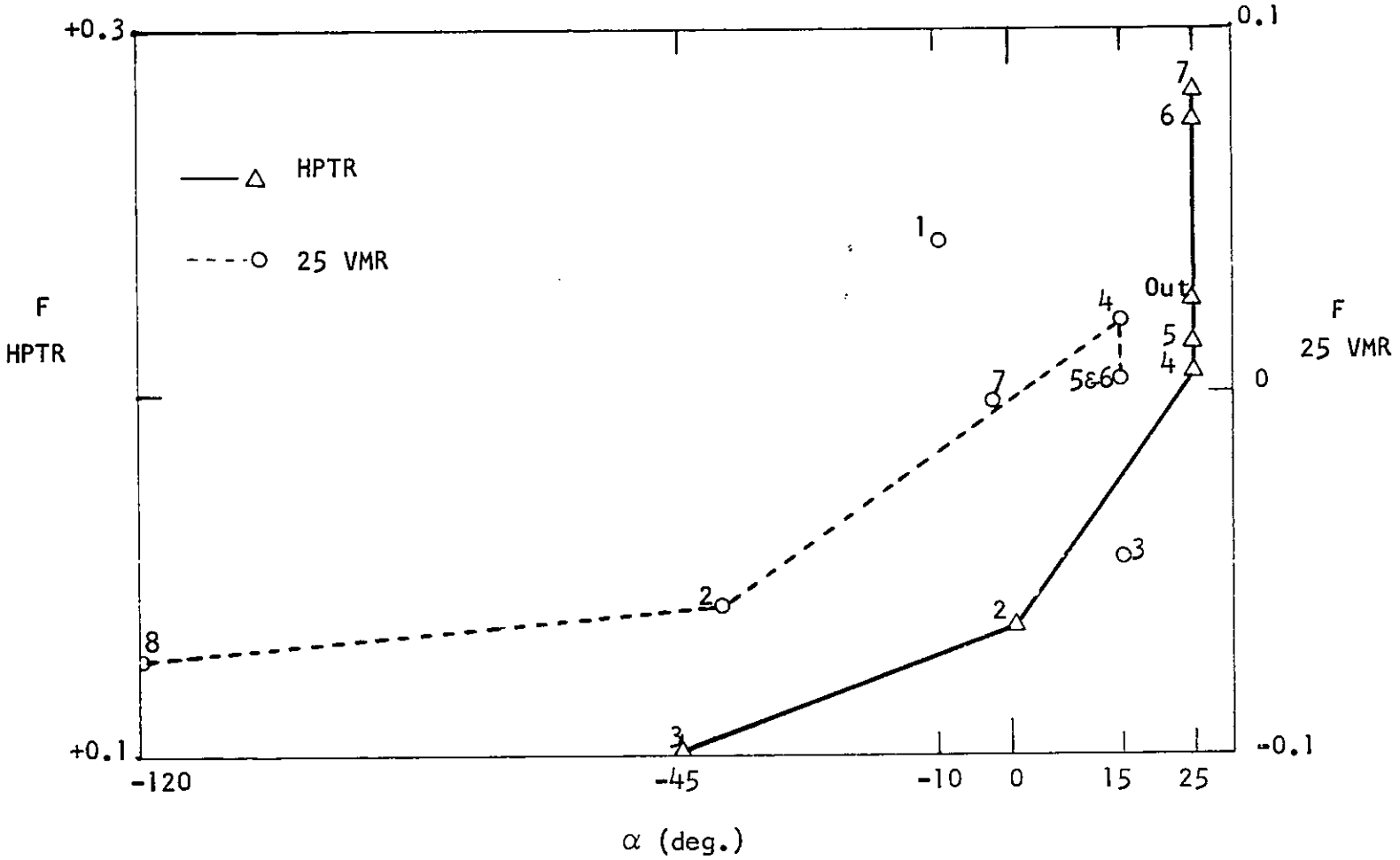

F I G U R E 36

TEXTURE PARAMETER S_1/S_0 VERSUS DEFORMATION PARAMETER ε_e

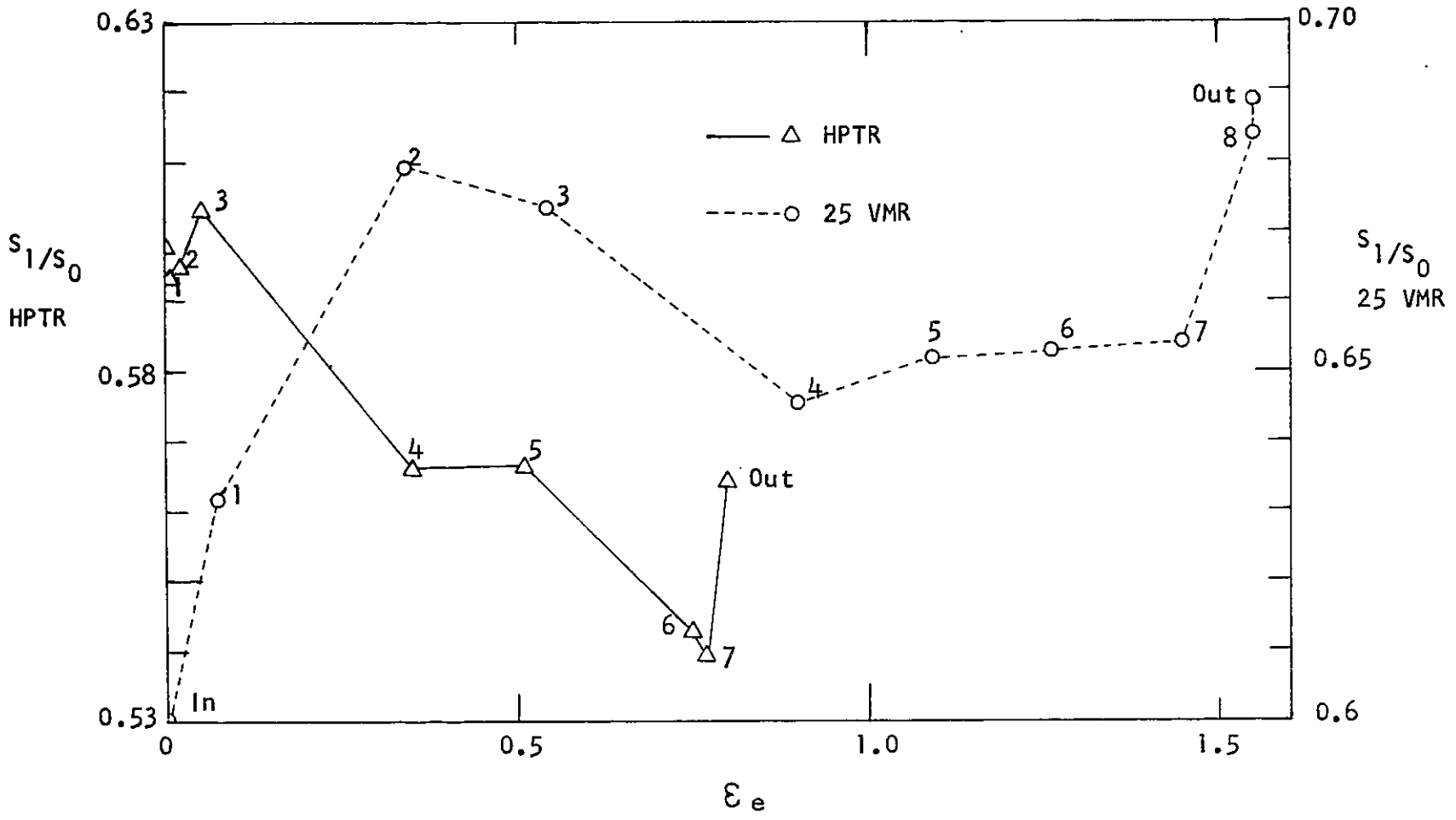

F I G U R E 37

TEXTURE PARAMETER S.D. VERSUS DEFORMATION PARAMETER ε_e

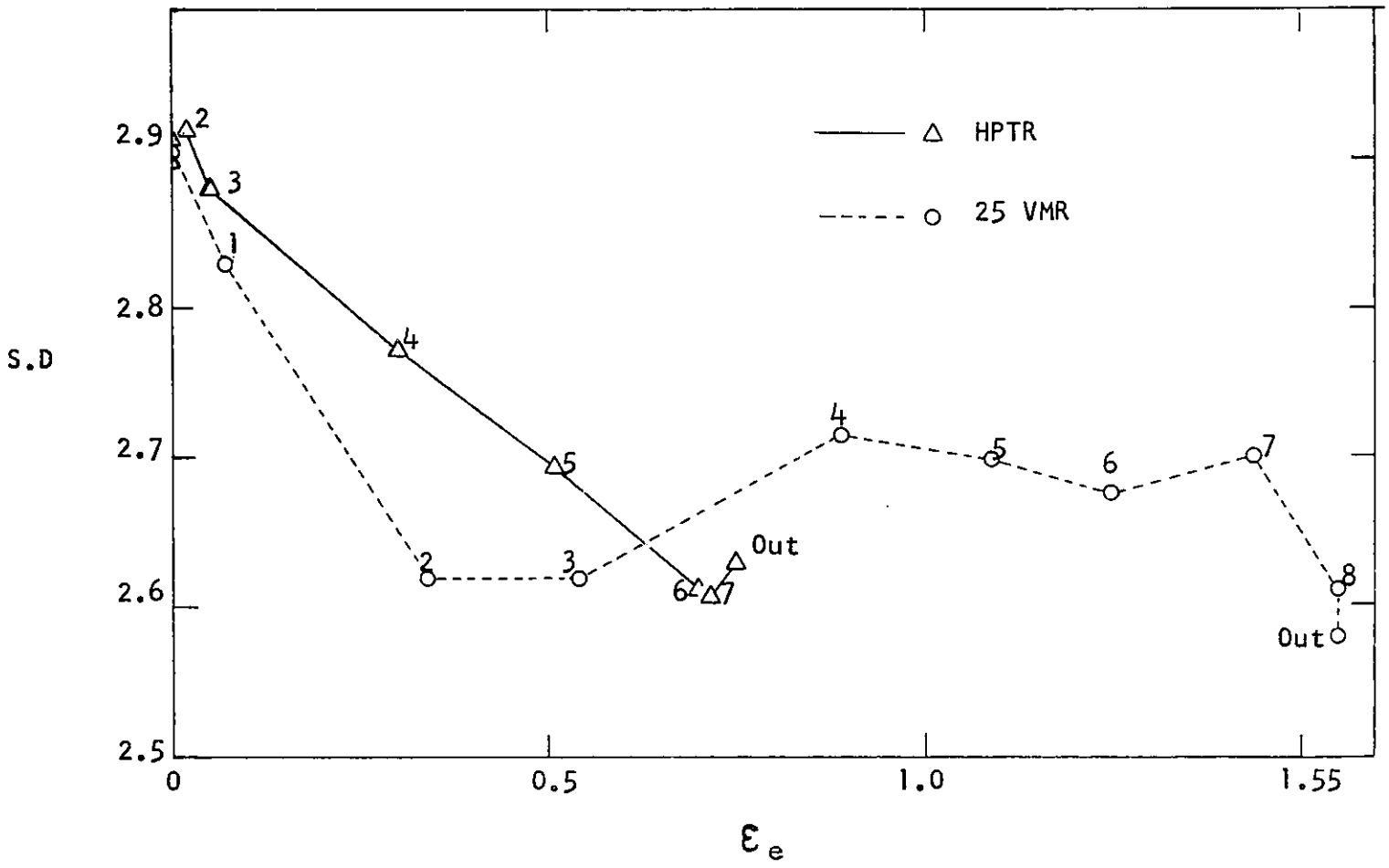

F I G U R E 38

TEXTURE PARAMETER F VERSUS DEFORMATION PARAMETER ε_e

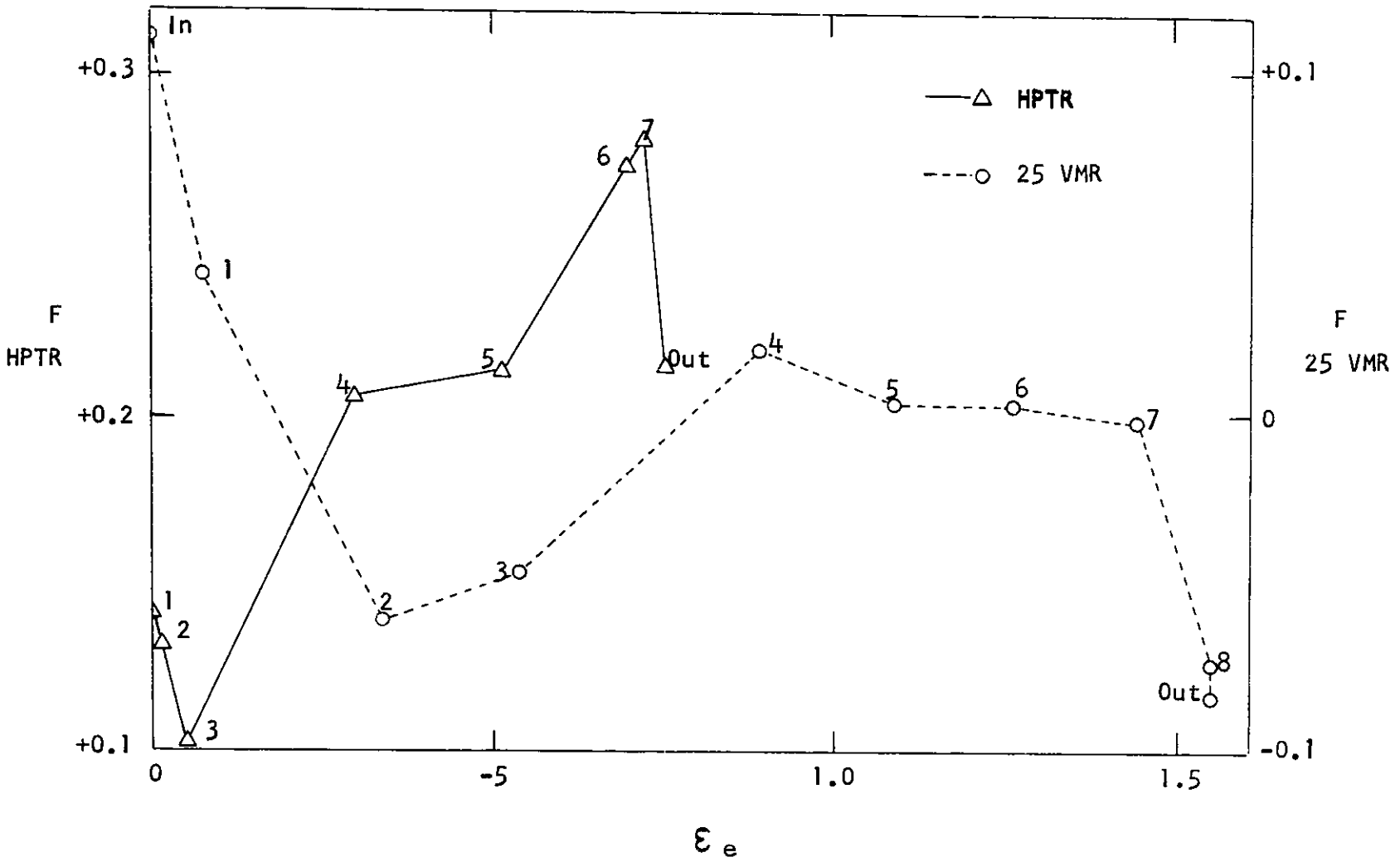

F I G U R E 39

CIRCUMFERENTIAL VARIATION FROM INVERSE POLE FIGURES

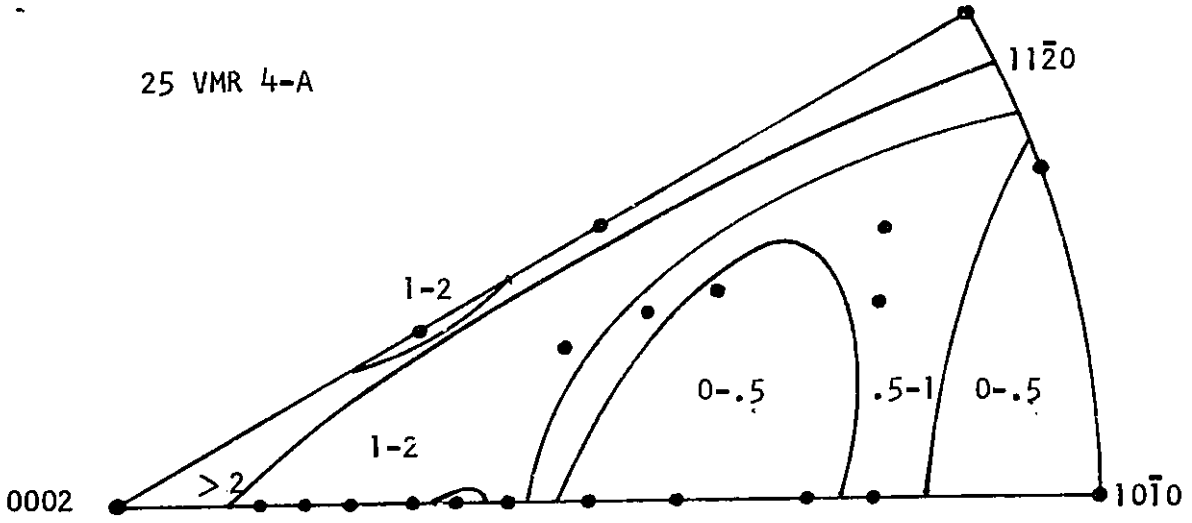

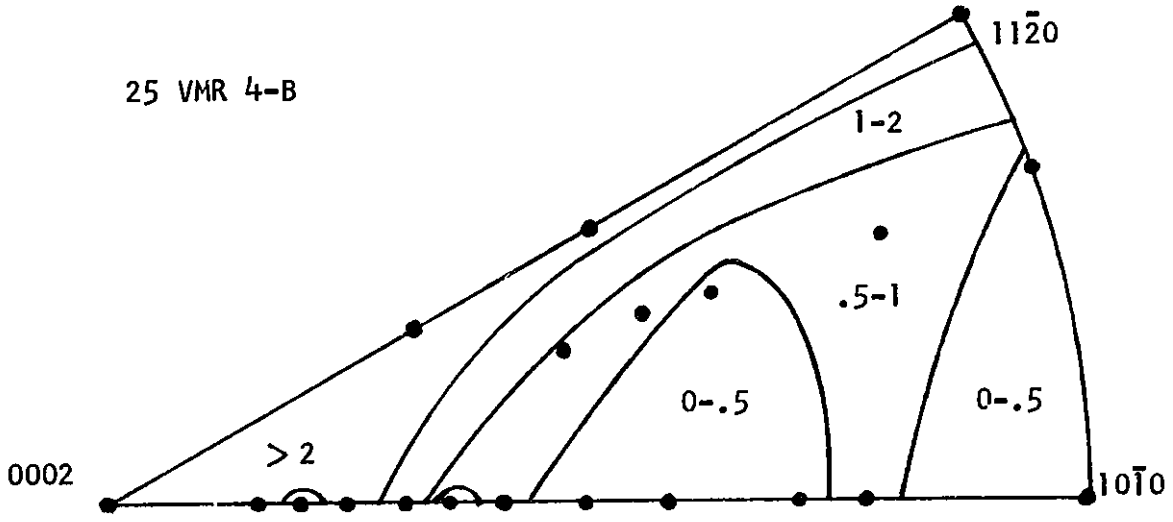

F I G U R E 40

CIRCUMFERENTIAL VARIATION FROM INVERSE POLE FIGURES

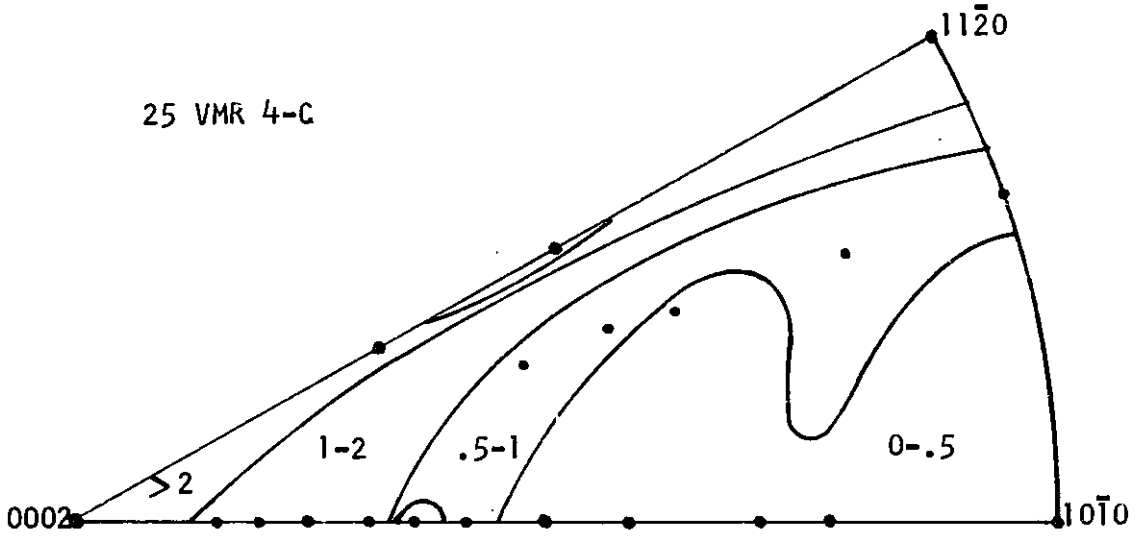

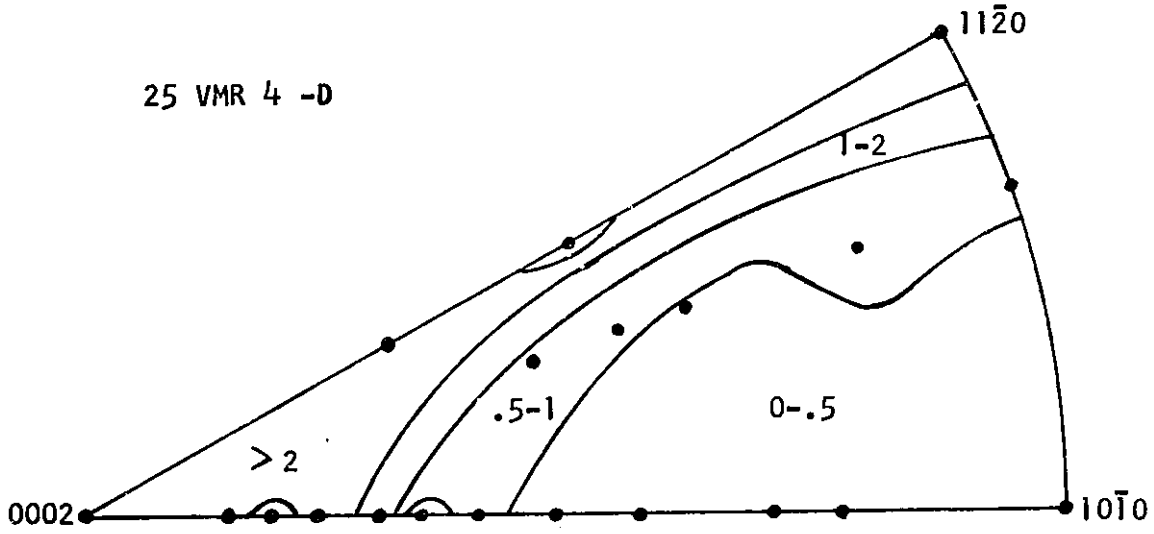

F I G U R E 41

HPTR MACHINE

CIRCUMFERENTIAL VARIATIONS FOR TEXTURE PARAMETER f

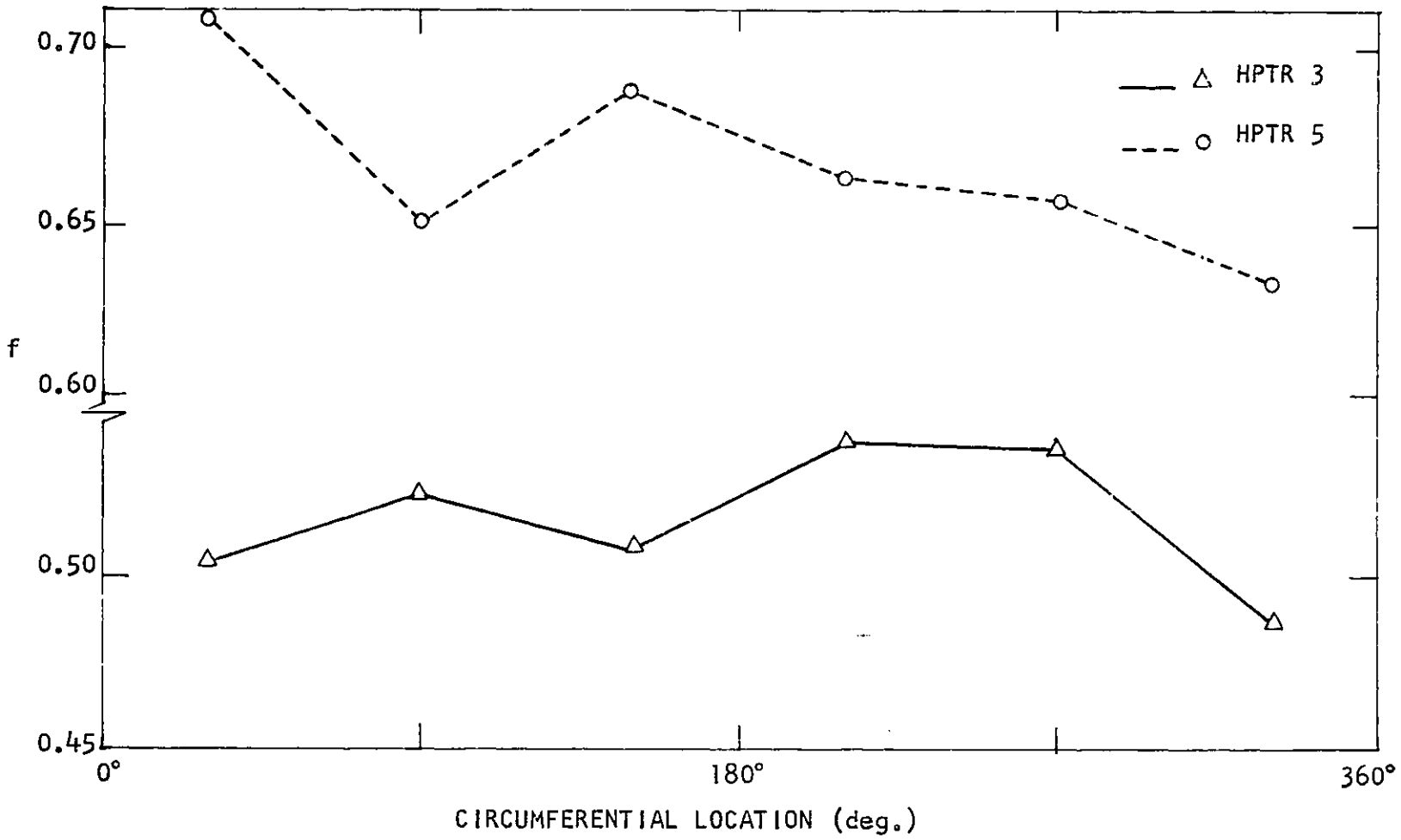

F I G U R E 42

25 VMR REDUCTION
CIRCUMFERENTIAL VARIATIONS FOR TEXTURE PARAMETER f

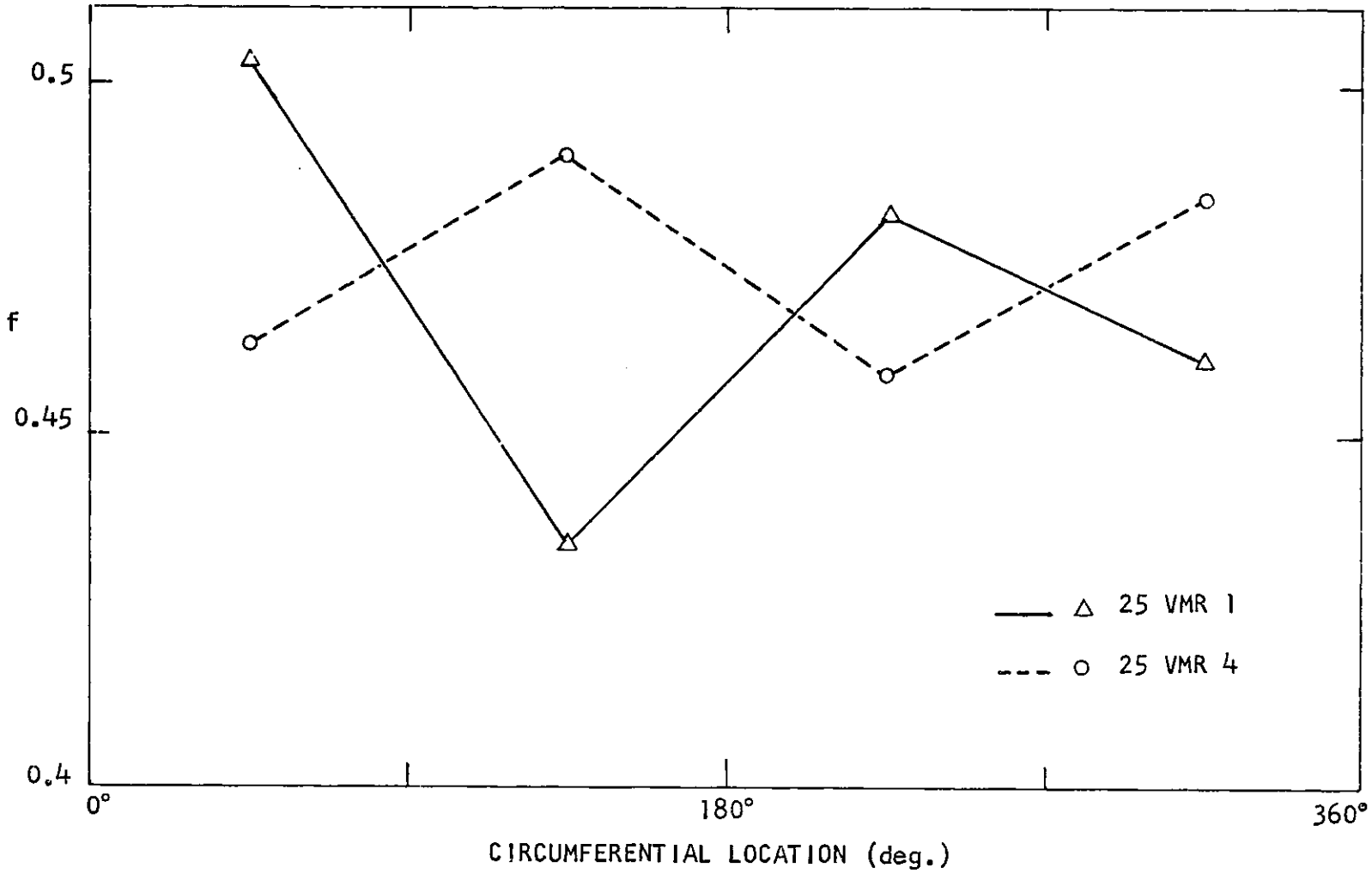

APPENDIX

Decker, Asp and Harker[25] designed the transmission technique for pole figure determination. The geometry of this technique, sketched in Fig.8 , does not allow to scan the center of the polar stereographic projection (Fig.9) because the specimen mount obstructs the X-rays for diffraction by planes almost parallel to the specimen surface. The method moreover requires correction for changes in X-ray absorption and scattering volume as the sample is rotated.

Schultz[26] designed the reflection technique.He demonstrated that this method eliminated the changes in absorption and scattering volume for flat sheet specimens. However corrections have to be made for geometric defocusing. As a sample is tilted, the diffracting line is effectively widened as a result of an apparent change in the Bragg angle.Less of this broader line is detected by the receiving slits resulting in a decrease of the measured intensity. Thus the reflection method does not resolve the pole figure for the high tilt angles ($\Psi > 75 - 80°$).

The specification ASTM E 81 "standard Method for Preparing Quantitative Pole Figures of Metal"requires that pole figures be determined by both transmission and reflection techniques.

However, it is current practice to use only reflection and plot only the central part of the pole figure.In this work, the correction for defocusing used are due to Knorr[16] and are summarized in Table Al.

TABLE A1

TABULATION OF EXPERIMENTALLY DETERMINED
GEOMETRIC DEFOCUSING VALUES

(deg.)	$I/I_{\Phi=0}$*
0	1.0
10	.9985
20	.9980
30	.9582
40	.9061
50	.8310
60	.7145
70	.4944
75	.3432
80	.1912

* Mean of 49 experimental runs